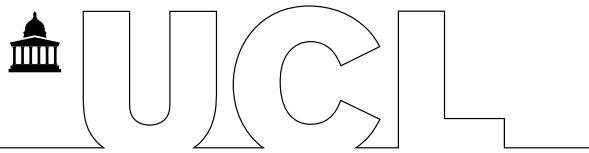

Electron-collisions with molecules of interstellar and plasma interest via the R-Matrix method

Stephen Harrison

A thesis submitted to University College London
for the degree of Doctor of Philosophy

Department of Physics and Astronomy
University College London

October 2012

I, Stephen Harrison, confirm that the work presented in this thesis is my own. Where previous work has been derived from other sources, I confirm that this has been referred to in the thesis. Any images taken from other sources have also been given due credit.

Acknowledgements

When I think back 12 years to when I sat in my physics class and told myself I wanted one day to have a PhD in the subject, I don't think I could ever have possibly imagined sitting here now typing this.

One person alone has made this entirely possible with their love and support, and for that I would like to thank my dad. This thesis is entirely dedicated to him and also to my mum, who will never be forgotten.

I would also like to thank my sister and brother-in-law for all their support, and I hope this inspires my wonderful nephew to go on and make them proud in whatever he decides to become. The world is yours Calum, anything is achievable if you want it.

For accepting me as a PhD student under the CASE studentship, I would like to thank both Dr. Dan Brown and Prof. Jonathan Tennyson. I hope that I have contributed in a wholly positive way to Quantemol as a company and I would like to say how grateful I am for being given the opportunity not only to study the subject I love, but also to learn many new and varied skills along the way. This simply wouldn't have been possible without the CASE studentship. Whilst talking of the company I would like to thank all the members of the team; Dr James Munro for teaching me the ropes and guiding me through the first 2 years of my PhD. Hemal Varambhia for his constant aid when first teaching me the software, and for his amazing help in writing this thesis. I believe the current team has the potential to make Quantemol flourish, and I would like to thank Anna Dzarasova, Adam Williams, Sergio Lopez and Brent Walker for their friendship over the last year. Finally from the company I would like to thank Will Brigg for his friendship and partnership as we solved many complex problems regarding the software and calculations, I hope I was able to guide him in his first year as I was guided by others.

Over the last 3 years I've been very lucky in being able to travel abroad to various

conferences. I've met some lovely people and would like to take this opportunity to thank both Mark Kushner and Nigel Mason, who guided me through these trips when I was still new to the entire experience. I would also like to thank UCL Physics and Astronomy for funding these trips.

I would like to thank Alexander Faure for his helpful guidance and partnership whilst working on the CN rotational code (chapter 4), and both Jimena Gorfinkiel and Zdenek Masin at the Open University for their advice in using some of the more advanced features of the R-Matrix codes. Also Bernard Keville at DCU for his patience and understanding as we tried something completely new in running the Oxygen atom (chapter 8).

Also a very special mention belongs to my fellow PhD students at UCL P&A, Charles Wood and Richard Spinney, who have been a constant source of friendship, laughter and companionship. Good times.

My final thank you is for Prof. Tennyson. He has guided me from my very first day to very last, always on hand with help and advise, no matter how complex or trivial. I hope that I have been a worthy student and the work we have done will mean something. To put it simply, my 10 year dream of getting this PhD simply wouldn't have ever been fulfilled without his guidance. I will always be grateful to him.

Abstract

Here the ab-initio R-Matrix method has been used to carry out electron-molecule collision calculations on the the molecules of interstellar interest C_3N, C_2H & CN, and molecules found in industrial plasma applications SiBr, $SiBr_2$ and NaI. These were carried out using the UK Molecular R-Matrix codes, along with the Quantemol expert system for running these codes. Calculations have also been carried out on electron collisions with atomic oxygen using these codes, with details included about the problems faced in running an atomic calculation with the molecular codes.

Calculations on each species include comparison of different models, including static-exchange and close-coupling models (with different size CAS tried), various basis sets, and for some species different initial orbitals. These different initial orbitals were either taken from the codes themselves (for SCF orbitals), or the quantum chemistry program MOLPRO (for natural orbitals), for the latter numerous state averaged orbitals were tried with different weightings in order to produce good target energies for carrying into the scattering calculation.

Results for all calculations include scattering observables such as eigenphase sums, elastic and excitation cross-sections, bound anionic states and resonance positions and widths.

Also a new theory has been developed for calculating rotational cross-sections which includes the spin angular momentum of the incoming scattering electron, this has been implemented into the already existing code ROTLIN, which can calculate rotational cross-sections using the scattering data from an R-Matrix calculation.

Contents

List of Figures

List of Tables

Chapter 1

Electron-Molecule Scattering and its Applications

1.1 Overview

The electron, first identified in 1897 by J. J. Thompson, plays a fundamental role in all the chemistry that occurs in the universe around us. Not only when bound to a parent atom or molecule, but also when existing as a free subatomic particle. One such type environment in which free electrons can be found are plasmas, these can be described as a state of matter in which a certain proportion of the particles are ionized. In other words this means a plasma is a 'soup' of positive and negatively charged particles (in this case, positively charged atoms and molecules, and the negatively charged free electrons). Plasmas can occur both naturally and artificially. To understand the nature of the plasma it is crucial to learn how the various particles can interact with each other. However free electrons can also exist in other environments too, and their interactions are not limited to collisions between negatively & positively charged particles. Indeed electron collisions with neutral molecules drive a number of significant processes, both natural and artificial, from the etching of silicon chips (Kimura et al., 2001), where the the 'soup' of ions and radicals can strip material, to causing natural phenomena such as the Northern and Southern lights, the aurora, where the interaction of electrons and molecules releases the energy we see (Meier, 1991). Electron molecule collisions also play key roles in the chemistry of planetary atmospheres (Broadfoot et al., 1979, 1981), an example being that of Saturn's moon Titan (Vuitton et al., 2009).

1.2 Low-Energy Processes

At low energies, defined in this case as all incident electron energies below a molecule's ionisation threshold, the following processes are especially important:

1. *Elastic scattering*

$$AB + e^- \rightarrow AB + e^-. \tag{1.1}$$

2. *Inelastic scattering*

   - Rotational excitation:

$$AB(j) + e^- \rightarrow AB(j') + e^-. \tag{1.2}$$

   - Vibrational excitation:

$$AB(\nu) + e^- \rightarrow AB(\nu') + e^-. \tag{1.3}$$

   - Electronic excitation:

$$AB + e^- \rightarrow AB^* + e^-. \tag{1.4}$$

3. *Fragmentation*

   - Dissociative Electron Attachment (DEA):

$$AB + e^- \rightarrow A^- + B. \tag{1.5}$$

   - Dissociative recombination:

$$AB^+ + e^- \rightarrow A + B. \tag{1.6}$$

   - Electron-impact dissociation

$$AB + e^- \rightarrow A + B + e^-. \tag{1.7}$$

At intermediate and higher energies electron-impact ionisation takes place:

$$AB + e^- \rightarrow AB^+ + 2e^-. \tag{1.8}$$

1.3 Industrial Plasmas

Let us consider in further detail the nature of an artificial plasma, these feature predominantly in the semiconductor industry, as they can be used in a variety of different ways. Plasma reactors can be used to either strip or deposit material onto surfaces, whether this be etching particular shapes onto silicon wafers by stripping surface layers, cleaning the inside of the reactor chamber by stripping away unwanted material from the walls, or depositing layers of material onto wafers to build 'MEMS' (microelectromechanical systems). Precise deposition of material is also crucial for the production of efficient solar cells. As the world becomes more and more driven by electronic items and computers, the semiconductor industry grows and grows, placing more and more emphasis on using the most efficient and cost-effective tools and processes. In order to do this it is crucial to understand in detail the precise interactions between species that occur within the plasma chamber. In order to create the charged species within the plasma (which drive these processes) neutral atoms and molecules must be stripped of electrons by applying current. As this happens one may consider how many collisions can occur between these free electrons and the remaining neutral atoms and molecules, these can drive further ionisation and are the fundamental processes which occur in the plasma discharge. Because of this it is important to know the precise way in which electrons can interact with neutral species, both in terms of collision energetics and reaction rate data. This is a key requirement for the progression of industrial plasma technology (Chistophorou and Olthoff, 2004). However there is still relatively little known about such processes, this is predominantly due to the lack of experimental data for the wealth of interactions that can exist in various industrial plasmas. One reason for this is simply that some species cannot be re-created in a controlled lab setup for electron-scattering experiments, where the species may not be stable enough to exist in any circumstance other than the plasma itself. This places the onus onto theoretical calculations for the relevant data.

1.4 The Importance of Electron-Molecule Collisions in the Interstellar Medium

In environments such as planetary nebulae, free electrons can interact with the atoms and molecules of the gas clouds that exist here. Electron-molecule collisions are important in the interstellar medium as the excitation rates caused by electron-molecule interactions

dominate over excitations due to neutral-neutral collisions. This becomes important when the electron-neutral ratio is over $\sim 10^{-5}$. In this thesis I concentrate on electron collisions with neutral, carbon-based molecules in the interstellar medium, as a precursor to forming the molecular anions observed.

The first anion detected in space was C_6H^- by McCarthy et al. (2006). Since then C_4H^- (Gupta et al., 2007), C_8H^- (Brunken et al., 2007), C_3N^- (Thaddeus et al., 2008) and C_5N^- (Cernicharo et al., 2008) have also all been detected. CN^-, C_3N^- or C_4H^-, and C_5N^- have also recently been identified in the atmosphere of Titan (Vuitton et al., 2009). CN^- has also been detected in the interstellar medium (ISM) (Agundez et al., 2010). These anions are all linear multiply-bonded carbon chains with closed shell. The prevailing opinion is that these anions are formed by radiative attachment of an electron to the neutral molecule with the same chemical formula (Millar et al., 2007). These neutral precursors are all linear multiply-bonded carbon chains with significant dipole moments which are known to exist in the interstellar medium. The corresponding anions are closed shell molecules whose extra electron is bound by several eV.

Herbst and co-workers (Petrie and Herbst, 1997; Terzieva and Herbst, 2000; Herbst and Osamura, 2008) developed and applied a model for calculating radiative association rates for these C_nH^- and $C_{n+1}N^-$ (n even) species. This model is based on the formation of low-lying resonances in electron collisions and fairly simple phase-space arguments. Studies suggest that although this model gives anion formation rates of approximately the right magnitude, the rates it provides cannot actually reproduce the observations Harada and Herbst (2008).

Although there have been a number of electronic structure studies of these anions (see for example Woon (1995), Natterer and Koch (1995), Botschwina and Oswald (2008), Fortenberry et al. (2010)), there appears to have been no previous study of their continuum states. We have therefore performed a series of studies of electron collisions with both C_nH and $C_{n+1}N$ (n even) targets. Initially this work focussed on electron collisions with C_4H and C_3N as the first member of each series for which the associated anion had been observed in the interstellar medium. However we found it difficult to establish definitive properties for the ground state of C_4H, a problem that is well-documented (Fortenberry et al., 2010). Here we report electron collision calculations which focus on CN, C_2H and C_3N as we consider the results of these calculations to be more reliable.

It is also worth noting the necessity for theoretical electron-collision studies on these

species. All of the neutral precursors are open-shell, having a single unpaired electron in their outermost orbital. These radicals are highly reactive and thus have a very limited lifespan in lab environments if being created for experiments. This makes obtaining experimental electron-collision data with these species extremely difficult.

1.5 Aims of this Thesis

1. To create accurate models of the neutral target species CN, C_3N, C_2H, NaI, O, SIBr & $SiBr_2$, with attention paid to accurately determining ground state energies and dipole moments, and vertical excitation energies. This shall be carried out using Hartree-Fock and configuration interaction methods with a variety of basis sets in order to meet experimental values (if they exist).

2. Using the *ab initio* R-matrix method to carry out both static-exchange and close-coupling scattering calculations on the neutral species above. From these will be obtained the scattering R-, K- and T-matrices and scattering observables (e.g. eigenphase sums and resonance data) and cross-sections (e.g. elastic, inelastic, ionisation).

3. Using the scattering T-matrices for CN, calculate the spin-coupled rotational cross-sections using the newly written program ROTLIN_S.

4. Consider the role of electron-induced chemistry in both astrophysical (Lovell et al., 2004) and industrial (Kimura et al., 2001) plasmas, considering the implications of the found results in existing models.

There are also other, non-result orientated goals for this thesis:

- To explain a new method for calculating spin-coupled rotational cross-sections, followed by an explanation of its computational implementation. This includes test cases for the code and example results for CN.

- To provide an explanation for using the UK molecular R-matrix codes in order to carry out electron-atom scattering. This includes a step-by-step methodology with potential problems identified and explained.

1.6 Layout of the Thesis

Chapter 2 outlines the basic principles of electron molecule scattering theory, including discussion of the various quantum chemistry methods which can be used to approximate the wavefunction of the target. Other theoretical pre-requisites are also explained here.

Chapter 3 discusses the R-matrix method for calculating electron-scattering data. Here the method is divided into two sections to explain how the method is applied to both the inner region (where the scattering target is contained) and the asymptotic outer region. It is then shown how scattering quantities (e.g. T-matrices) are obtained and from these the scattering observables can be determined. Then an introduction to the UK molecular R-matrix code package is given, discussing the history, structure and usage of the codes in order to carry out a full calculation. The work in this thesis also led to two new contributions being made to the R-matrix suite of codes, these are explained here.

In order to make the suite of codes easier to use for the non-expert, the Quantemol-N software was created. This was done in order to simplify and streamline using the codes, as to manually run the codes through a full calculation is very difficult for someone inexperienced. This can lead to small mistakes being made in the calculation input which propagate through to give erroneous final data. In the final part of this chapter this streamlining of the codes is explained and the usage of Quantemol-N in this thesis is outlined.

Chapter 4 presents the newly-developed theory for calculating spin-rotational cross-sections. Starting with an introduction to the need for this data and the previous work in the field, the starting point for this new theory is then explained by describing the existing theory. This is then developed to include the spin-coupling before the infinite order sudden approximation is applied to simplify the calculation. Finally a description of the computational implementation of this theory is given, along with test results for CN.

Chapters 5–10 present the results of the electron-scattering investigations undertaken over the duration of this research. All work was carried out using the R-matrix method and experimental comparisons have been given where available.

Chapter 5 is the results of the investigation into e-CN scattering, where a number of scattering models and bond lengths have been analysed. Spin-coupled rotational cross-sections have also been calculated for the first few rotational levels.

Chapters 6 & 7 present the results for the e-C_3N and e-C_2H calculations respectively, using a variety of scattering models. In these chapters emphasis is placed on investigating low-lying resonances and bound states as potential routes for radiative attachment to the neutral targets for anion formation.

Chapter 8 describes the theoretical calculation of the ^3P–^3P excitation cross-section of atomic oxygen. This chapter is the first know 'true' usage of the UK molecular R-matrix codes when applied to e-atom scattering. It contains the full methodology for using the codes for an atom, including potential problems and pitfalls associated with this unique usage of the codes.

Chapters 9 & 10 present electron-scattering investigations into species of industrial plasma interest, NaI, SiBr & $SiBr_2$. Here full sets of results and cross-section data are presented for each for the close-coupling scattering model (NaI) and both the static-exchange and close-coupling scattering models (SiBr & $SiBr_2$). All calculations in these two chapters were carried out solely using Quantemol-N.

The thesis is concluded with a brief summary of the findings of each chapter and their potential implications in future plasma modelling (both astrophysical and industrial). Where applicable criticisms of the work and suggestions for future investigations have been given.

Chapter 2

Background Theory

2.1 Electron-Molecule Scattering Theory

When considering the low-energy scattering interaction between and atom and an electron there are three possible outcomes:

1. *elastic scattering*

$$e^- + A \rightarrow e^- + A, \tag{2.1}$$

2. *inelastic scattering*

$$e^- + A \rightarrow e^- + A^*, \tag{2.2}$$

3. *electron-impact ionisation*

$$e^- + A \rightarrow 2e^- + A^+. \tag{2.3}$$

However electron-molecule scattering events have many more outgoing channels as the molecule can undergo nuclear excitation (both rotational and vibrational) at very low energies. Also fragmentation channels can open leading to dissociation. Some examples of electron-molecule scattering outcomes are (in approximate order of increasing scattering electron impact energy):

1. *elastic scattering*

$$e^- + AB \rightarrow e^- + AB, \tag{2.4}$$

2. *rotational excitation*

$$e^- + AB(j'') \rightarrow e^- + AB(j'), \tag{2.5}$$

where j is the rotational state of the target.

3. *vibrational excitation*

$$e^- + AB(v'' = 0) \rightarrow e^- + AB(v'), \tag{2.6}$$

where v is the vibrational state of the target

4. *electronic excitation*

$$e^- + AB \rightarrow e^- + AB^*, \tag{2.7}$$

5. *dissociation*

$$e^- + AB \rightarrow e^- + A + B, \tag{2.8}$$

6. *dissociative electron attachment*

$$e^- + AB \rightarrow A^- + B. \tag{2.9}$$

All of these events can occur at low scattering energies, thus low energy electron scattering can be a complex process with many subtle effects and possible outcomes.

As for all multiple-body interactions described using quantum mechanics, the scattering interaction can be described using the Schrödinger equation. However it is well established that for even the simplest three-body system no analytical solution can be calculated, and thus numerical methods must be implemented.

Various models are routinely used for the numerical treatment of low energy electron-molecule scattering. Some are basic and allow for rough but solid approximations, whilst others are more detailed and computationally intensive, but allow for excellent results to be obtained. In this work we have used the following models:

1. *Static exchange* (SE): In this model the target wave function is not allowed to relax (or polarize) in response to the incoming electron. However exchange effects between the target electrons and the projectile electron are included. In this approximation only a single wavefunction is used to describe the target, and this is usually a Hartee-Fock wavefunction (see section 2.3.1 for more information on HF). Because the target is 'fixed' in place and the electrons cannot move from their initial orbitals, the SE method cannot treat electronic impact excitation. Consequently it cannot be used to model Feshbach resonances as these are associated with this process. Shape resonances can be found using SE but their energy is usually too high as the polarization effects missing from this method usually act to

lower the resonance position (see section 3.3.2 for more information on resonances). Polarization effects can be included to create the *static exchange plus polarization* (SEP) method. However this model was not used in this work.

2. *Close-coupling* (CC): Within the CC method the target wavefunction includes several target states rather than a single state. This means the target is no longer 'fixed' as in SE and excitations of the target electrons can be included by ensuring the target wavefunction expansion contains several electronic states. This method is more computationally intensive than SE or SEP but in principle allows for a complete treatment of the low-energy scattering problem, including electronic excitations and detecting Feshbach resonances. It also introduces some complications that arise from having more than a single Hartree-Fock target state. For instance all states included in the target wavefunction expansion must be described using the same orbital set, of which there is no best choice. A common limit on the number of target states used in the expansion is to retain all those up to the ionization energy of the target, this is required as theoretically there is an infinite number of target states which could be included, but this method cannot have an infinite number of states. This limits the use of the CC method to describe scattering events below the ionization threshold of the target molecule. The expansion of the target wavefunction is given in terms of a complete set of unperturbed eigenstates of the isolated molecule ψ_i (Lane, 1980*a*):

$$\Psi_\varepsilon = \hat{A} \sum_i F_i(\mathbf{r}_{N+1})\psi_i, \tag{2.10}$$

where $\hat{A}$ is the antisymmetrisation operator and $\mathbf{r}_{N+1}$ is the position vector of the scattering electron. The summation in equation (2.10) could also theoretically include the continuum states of the target molecule. $F_i(\mathbf{r}_{N+1})$ is the one-electron scattering function, which satisfies this set of coupled equations:

$$\left[\nabla^2_{N+1} + k_n^2\right] F_i(\mathbf{r}_{N+1}) = \sum_j [V_{ij} + W_{ij}] F_j(\mathbf{r}_{N+1}), \tag{2.11}$$

where k_n is the linear momentum of the channel and ∇^2_{N+1} is the Laplacian operator for the scattering electron. The $F_i(\mathbf{r}_{N+1})$ corresponding to a target state i will depend on the initial target state specified by the asymptotic boundary conditions

$$\lim_{r\to\infty} \Psi_\varepsilon \sim \Psi_{inc} + \Psi_{scat}, \tag{2.12}$$

with an incident wavefunction described by an initial target state ψ_0 and wave vector $\mathbf{k}_0$

$$\Psi_{inc} = e^{i\langle \mathbf{k}_0, \mathbf{r} \rangle} \psi_0, \tag{2.13}$$

and a scattering wavefunction described by

$$\Psi_{scat} = \frac{1}{r} \sum_j e^{i\mathbf{k}_j \cdot \mathbf{r}} f_{j0}(\mathbf{k}_j, \mathbf{k}_0) \psi_j. \tag{2.14}$$

$f_{j0}(\mathbf{k}_j, \mathbf{k}_0)$ is the scattering amplitude for a transition $0 \rightarrow j$. V_{ij} is the electron-molecule scattering potential and W_{ij} is the exchange matrix. Using the R-matrix method in the outer region, the exchange is considered negligible so the antisymmetrisation operator $\hat{A}$ is omitted and (from chapter 3) $W_{ij} = 0$.

Equation (2.11) can be reduced to a set of coupled second order ordinary differential equations by expanding $F_i(\mathbf{r}_{N+1})$ using spherical harmonics $Y_l^m(\theta, \phi)$.

3. *Born dipole approximation for high energies*: When the dipole moment of a scattering target is large its long range dipole potential becomes significant and the Born approximation can be applied (e.g. Chu and Dalgarno (1974*a*)).

   This approximation calculates the total cross-section of the scattering event in which the number of partial waves required to converge to an answer is very large (this can occur when there is a long range dipole potential).

   In this work a Born correction is applied to the total cross-sections calculated, this acts to correct for all partial waves l above the threshold l_0, where the partial waves below this limit are treated using another scattering theory which is more appropriate for modelling the short-range interactions (our pre-Born corrected cross-sections). This correction is obtained by calculating both a total Born cross-section for all partial waves and a another containing only the waves $l \leq l_0$, the difference between the two being the Born correction for waves above l_0 (Norcross and Padial, 1982):

$$\delta\sigma(E) = \sigma_B(E) - \sigma_{B,l \leq l_0}(E), \tag{2.15}$$

   for an energy E, this is then added to the data from the other scattering theory (in this work the Born correction was applied to the cross-sections we obtained by using the CC method).

We applied the Born approximation and correction to the total cross-sections of SiBr & $SiBr_2$ in chapter 10, to both the total and the electronic excitation cross-sections of CN (chapter 5), C_3N (chapter 6) & C_2H (chapter 7), and finally to both the total cross-sections and the scaled BE excitation cross-sections for NaI (chapter 9), in all of these calculations a value of 4 for l_0 was used. These corrections were calculated using the computer program BORNCROSS (Baluja et al., 2001), which is regularly used as part of molecular R-matrix calculations.

2.2 Born-Oppenheimer Approximation

The Born-Oppenheimer approximation is the scheme in which the motions of electrons and nuclei in the same molecule can be separated. This approximation is valid as the electron is so much lighter than a nucleon (and so moves much faster), thus the electrons are seen to instantaneously 'relax' to any movement of the nuclei. Mathematically one can separate the electronic and nuclear parts of the molecular wavefunction, enabling the electronic part to be considered separately at each position of the nuclei. By starting with the non-relativistic Hamiltonian for a molecule of N_n nuclei and N_e electrons (in atomic units):

$$\hat{H}_t = -\sum_{A=1} \frac{1}{2M_A}\nabla_A^2 - \sum_{i=1} \frac{1}{2}\nabla_i^2 - \sum_{A,i} \frac{Z_A}{|\mathbf{r}_i - \mathbf{R}_A|} + \sum_{A>B} \frac{Z_A Z_B}{|\mathbf{R}_A - \mathbf{R}_B|} + \sum_{i>j} \frac{1}{|\mathbf{r}_i - \mathbf{r}_j|}. \quad (2.16)$$

Because the electrons move so much faster than the nuclei, it is assumed that they move in the Coulomb field of the nuclei. Within this approximation the first term (nuclear kinetic energy) in (2.16) may be removed and the nuclear repulsion term is simply a constant which does not effect the eigenkets associated with this equation, as constant operators only effect the resulting eigenvalue as opposed to changing the eigenket itself. After implementing these changes to (2.16) we are left with the electronic Hamiltonian $\hat{H}_e$ describing the motion of N_e electrons in the Coulomb field of N_n nuclei:

$$\hat{H}_e = -\sum_{i=1} \frac{1}{2}\nabla_i^2 - \sum_{A,i} \frac{Z_A}{|\mathbf{r}_i - \mathbf{R}_A|} + \sum_{A>B} \frac{Z_A Z_B}{|\mathbf{R}_A - \mathbf{R}_B|} + \sum_{i>j} \frac{1}{|\mathbf{r}_i - \mathbf{r}_j|}. \quad (2.17)$$

So from the standard Schrödinger equation used to obtain the energy of the system:

$$\hat{H}\psi = E\psi. \quad (2.18)$$

The Schrödinger equation for the electronic motion is then

$$\hat{H}_e \psi_e(\{\mathbf{r}_i\}_{i=1}^{N_e}; \{\mathbf{R}_A\}_{A=1}^{N_n}) = E_e(\{\mathbf{R}_A\}_{A=1}^{N_n}) \psi_e(\{\mathbf{r}_i\}_{i=1}^{N_e}; \{\mathbf{R}_A\}_{A=1}^{N_n}). \quad (2.19)$$

The solutions of which depend explicitly on $\{\mathbf{r}_i\}_{i=1}^{N_e}$ and parametrically on $\{\mathbf{R}_A\}_{A=1}^{N_n}$, the nuclear co-ordinates. So for each set of nuclear coordinates there will be a set of solutions and energy eigenvalues $E_e(\{\mathbf{R}_A\}_{A=1}^{N_n})$. This equation is initially solved excluding the nuclear repulsion term to give the electronic energy eigenvalue $\varepsilon_e(\{\mathbf{R}_A\}_{A=1}^{N_n})$, this is then modified by adding the nuclear repulsion to it to obtain the Hamiltonian eigenvalue E_e,

$$E_e(\{\mathbf{R}_A\}_{A=1}^{N_n}) = \varepsilon_e(\{\mathbf{R}_A\}_{A=1}^{N_n}) + \sum_{A>B} \frac{Z_A Z_B}{|\mathbf{R}_A - \mathbf{R}_B|}. \tag{2.20}$$

We now have a complete description of the electronic part of the molecular system.

In order to do the same for the nuclear motion we make the same assumptions as before: As the electrons relax 'instantly' to any nuclear movement, the nuclei see the electrons smeared out into an average. Thus the electronic co-ordinates of equation (2.16) can be replaced by their averaged values, averaged over the electronic wavefunctions. Thus the nuclear motion Hamiltonian, which averages the electronic motion, is defined as:

$$\begin{aligned}
\hat{H}_n &= -\sum_{A=1} \frac{1}{2M_A}\nabla_A^2 + \left\langle -\sum_{i=1} \frac{1}{2}\nabla_i^2 - \sum_{A,i} \frac{Z_A}{|\mathbf{r}_i - \mathbf{R}_A|} + \sum_{i>j} \frac{1}{|\mathbf{r}_i - \mathbf{r}_j|} \right\rangle \\
&\quad + \sum_{A>B} \frac{Z_A Z_B}{|\mathbf{R}_A - \mathbf{R}_B|} \qquad (2.21) \\
&= -\sum_{A=1} \frac{1}{2M_A}\nabla_A^2 + \varepsilon_e(\{\mathbf{R}_A\}_{A=1}^{N_n}) + \sum_{A>B} \frac{Z_A Z_B}{|\mathbf{R}_A - \mathbf{R}_B|} \qquad (2.22) \\
&= -\sum_{A=1} \frac{1}{2M_A}\nabla_A^2 + E_e(\{\mathbf{R}_A\}_{A=1}^{N_n}), \qquad (2.23)
\end{aligned}$$

where $E_e(\{\mathbf{R}_A\}_{A=1}^{N_n})$ is the molecule's potential energy surface (PES) and provides a potential which determines the nuclear motion. This means in the BO approximation the PES can only be found once the electronic problem has been solved. The nuclear Schrödinger equation

$$\hat{H}_n \Phi_n(\{\mathbf{R}_A\}_{A=1}^{N_n}) = \varepsilon_n \Phi_n(\{\mathbf{R}_A\}_{A=1}^{N_n}). \tag{2.24}$$

has solutions which describe the movement of the nuclei along the PES, thus giving information on the vibration, rotation and translation of a molecule, where ε_n is the Born-Oppenheimer approximation to the total energy, including the electron, vibrational, rotational and translation energies. The total wavefunction solution of equation (2.16) is then

$$\Phi(\{\mathbf{r}_i\}_{i=1}^{N_e}; \{\mathbf{R}_A\}_{A=1}^{N_n}) = \psi_e(\{\mathbf{r}_i\}_{i=1}^{N_e}; \{\mathbf{R}_A\}_{A=1}^{N_n}) \Phi_n(\{\mathbf{R}_A\}_{A=1}^{N_n}). \tag{2.25}$$

2.3 Molecular Orbitals

2.3.1 Hartree-Fock Approximation

The Hartree-Fock method is an approximation used for determining the ground state wavefunction of a quantum system.

One can equate Hartree-Fock theory to single (Slater) determinant theory (Szabo and Ostlund, 1996). By applying the variational principle a set of spin-orbitals χ_a can be formed such that the single determinant formed from these:

$$|\Psi_0\rangle = |\chi_1\chi_2\cdots\chi_a\chi_b\cdots\chi_{N_e}\rangle, \tag{2.26}$$

is an approximation of the ground state of an N_e-electron system described by an electronic Hamiltonian, determining both the ground state wavefunction and energy. From the variational principle, the best spin-orbital set is that which minimises the electronic energy functional

$$E_0(\Psi_0) = \langle\Psi_0|\hat{H}_{elec}|\Psi_0\rangle = \sum_a \langle a|\hat{h}|a\rangle + \frac{1}{2}\sum_{ab}\langle aa|bb\rangle - \langle ab|ba\rangle, \tag{2.27}$$

where

$$\langle ij|kl\rangle = \int d\tau_1 d\tau_2 \chi_i^*(\mathbf{x}_1)\chi_j(\mathbf{x}_1) r_{12}^{-1} \chi_k^*(\mathbf{x}_2)\chi_l(\mathbf{x}_2), \tag{2.28}$$

and the one-particle Hamiltonian is

$$\hat{h}(1) = -\frac{1}{2}\nabla_1^2 - \sum_A \frac{Z_A}{r_{1A}}, \tag{2.29}$$

with the constraint that the spin-orbitals be orthogonal:

$$\langle\chi_i|\chi_j\rangle = \delta_{ij}. \tag{2.30}$$

The spin-orbitals are then varied until E_0 is minimised. The equation for obtaining the best possible spin-orbitals set is the Hartree-Fock eigenvalue equation:

$$\left[\hat{h}(1) + \sum_{b\neq a}\mathcal{J}_b(1) - \sum_{b\neq a}\mathcal{K}_b(1)\right]\chi_a(1) = \varepsilon_a\chi_a(1) \tag{2.31}$$

and where the exchange and Coulomb operator are defined using

$$\mathcal{K}_b(1)\chi_a(1) = \left[\int d\tau_2 \chi_b(2)^* \frac{1}{r_{12}}\chi_a(2)\right]\chi_b(1), \tag{2.32}$$

$$\mathcal{J}_b(1)\chi_a(1) = \left[\int d\tau_2 \chi_b(2)^* \frac{1}{r_{12}}\chi_b(2)\right]\chi_a(1). \tag{2.33}$$

respectively. From the restricted summation, the operator in the square brackets is different for every spin-orbital χ_a. However, if one lets $b = a$ it is clear, from equations (2.32) and (2.33), that $[\mathcal{J}_b(1) - \mathcal{K}_b(1)]\chi_a(1) = 0$ and therefore it is quite possible to add this term to equation (2.31) with no major effect on the spin-orbitals. Now, we define a Fock operator $\hat{f}$

$$\hat{f}(1) = \hat{h}(1) + \sum_b \mathcal{J}_b(1) - \mathcal{K}_b(1). \tag{2.34}$$

The Hartree-Fock equation is simplified to

$$\hat{f}|\chi_a\rangle = \varepsilon_a|\chi_a\rangle. \tag{2.35}$$

This method is normally computed using a self-consistent algorithm, iteratively cycling through the variational optimization of spin-orbitals until the value of the ground state energy has converged to a suitably defined accuracy.

To do this the Hartree-Fock method makes some simplification to the complete problem:

1. Born-Oppenheimer approximation is assumed, thus only the coordinates of the electrons are included in the wavefunction.

2. Relativistic effects are neglected and the momentum operator used is entirely non-relativistic.

3. The variational solution is assumed to be a linear combination of basis functions, normally orthogonal, this finite basis is assumed to approximately be complete.

4. Each energy eigenfunction can be described by a single Slater determinant (which is the antisymmetrical product of the one electron orbitals in the system).

5. A mean field approximation is implied, whereby all the individual effects of each electron upon a single electron is replaced by an average field effect.

6. One consequence from this assumption is that electron correlation is taken into account for same-spin pairs of electrons, however it is omitted for pairs of different spins.

A full derivation of the Hartree-Fock (HF) equations is presented in Szabo and Ostlund (1996).

2.3.2 Basis Sets

Spin-orbitals describing the electrons contain both a spatial and spin component:

$$\chi_i(\mathbf{x}) = \begin{cases} \psi_i(\mathbf{r})|\alpha\rangle, \\ \psi_i(\mathbf{r})|\beta\rangle. \end{cases} \tag{2.36}$$

By eliminating spin, the calculation of the molecular orbitals is equivalent to solving the

$$\hat{f}(\mathbf{r}_i)\psi_i(\mathbf{r}_i) = \varepsilon_i\psi_i(\mathbf{r}_i) \tag{2.37}$$

eigenvalue equation (Szabo and Ostlund, 1996). By introducing a known spatial basis set (Roothan, 1951) the equations (2.37) may be transformed to a set of algebraic equations which may be solved by techniques of linear algebra.

In solving for the spatial part of the spin-orbitals one expands the molecular orbitals as a linear combination of known (atomic) ones:

$$\psi_i = \sum_{j=1} C_{ij}\phi_j. \tag{2.38}$$

These atomic orbitals, $\{\phi_i\}_{i=1}^{B}$, are traditionally described using one of two ways:

1. Slater-type orbitals (STOs) (Slater, 1960)

$$\phi^s_{nlm} = \sqrt{\frac{(2\zeta)^{2n+1}}{(2n)!}} r_\alpha^{n-1} e^{-\zeta r_\alpha} Y_l^m(\theta_\alpha, \phi_\alpha), \tag{2.39}$$

   with ζ a constant.

2. Gaussian-type orbitals (GTOs) (Boys, 1950)

$$\phi^g_{nlm} = N r_\alpha^{n-1} e^{-\zeta r_\alpha^2} Y_l^m(\theta_\alpha, \phi_\alpha), \tag{2.40}$$

   where r_α is the distance of the electron from a nuclear centre α, ζ is again a constant and N is a normalisation constant.

Slater-type orbitals are capable of describing the best possible representation of the molecular orbitals ψ_i with the least number of terms required in the expansion (2.38). However Gaussian-type orbitals have the advantage that two-electron integrals can be evaluated very fast and very accurately due to the way in which Gaussian functions can combine to form another Gaussian, this means the computation of the spin-orbitals is

much more efficient with this method. One can combine the advantages of both types of orbital to form contracted Gaussian functions. These have the form

$$\phi_i^{cg}(r_\alpha) = \sum_{p=1}^{L} d_{pi} g_p(\alpha_{pi}, r_p), \tag{2.41}$$

where α_{pi} and d_{pi} are the contraction exponents and coefficients and L is the length of the contraction. Integrals involving these reduce to sums of integrals involving the primitive Gaussians g_p, where these are described by (2.40). Although there may be many primitive integrals to be evaluated for each basis function, the basis function integrals will be rapidly calculated provided the method of computing primitive integrals is very fast (Szabo and Ostlund, 1996).

The calculations in this work have commonly used both the Dunning 'Double Zeta Polarised' (DZP) basis set (Dunning, 1970), or the 'correlation consistent polarized valence' (cc-pVnZ) basis sets of Dunning (1989). A library of contracted GTO basis sets may be found in the EMSL online database (Schuchardt et al., 2007).

2.3.3 Configuration Interaction Methods

Whilst the Hartree-Fock method is extremely quick to carry out using modern quantum chemistry computer programs, it will only ever give an approximation to the true ground state of a system. Furthermore this method does not include the short range correlation between electrons, a consequence of assuming the mean field approximation. Another problem with using the HF method is that the calculated dipole moment of the ground state is often far removed from the accepted value, this can have a negative influence when performing electron-scattering calculations of polar molecules, such as in this work.

The configuration interaction (CI) method is one of many 'post-HF' methods to exist, so called as they use the molecular orbitals initially created using the HF method and implement them in the resulting calculation. The underlying principle of the CI method is to obtain a diagonalised representation of the N_e-electron Hamiltonian operator in the basis of N_e-electron functions or Slater determinants. As opposed to the HF method, in which a single Slater determinant is used to represent the ground state wavefunction of a system, the CI method creates a wavefunction of the system using a linear combination of Slater determinants. This means that as well as the ground state, excited states are also described if the relevant electron configurations Slater determinant, these are commonly known as *configuration state functions*, or CSFs.

Theoretically the CI method can yield an exact solution to the N_e-electron problem but due to the long CPU time and the large hardware requirements needed by this method, one can only handle a finite set of N_e-electron trial functions so the method only provides upper bounds on the exact eigenenergies.

In order to account for the electron correlation, the CI method uses a linear combination of CSFs

$$|\Phi_0\rangle = |\Psi_0\rangle + \sum_{ar} c_a^r |\Psi_a^r\rangle + \frac{1}{2!} \sum_{a<b,r<s} c_{ab}^{rs} |\Psi_{ab}^{rs}\rangle + \cdots , \tag{2.42}$$

where a,b are spin-orbitals occupied and r,s are virtual spin-orbitals in the reference determinant, $|\Psi_0\rangle$. This is normally the HF Slater determinant describing the ground state (lowest energy set of spin-orbitals). The higher terms in this expansion can be characterised by how they compare to this first term. Firstly we have the single excitations, $|\Psi_a^r\rangle$, configurations where a single electron has been promoted into one of the virtual orbitals of the reference determinant (thus all these single excitation terms differ from the reference by one spin-orbital). Similarly the next set of terms, $|\Psi_{ab}^{rs}\rangle$, are known as double excitations, whereby two spin-orbitals in the reference determinant are swapped with virtual orbitals.

Furthermore this expansion can continue up to the nth excitation described by n-tuply excited determinants. This allows a limit to be placed of the number of determinants in the expansion, called the CI-space. The coefficients c_a^r and c_{ab}^{rs} in (2.42) are determined by the variational principle, and the summations for the excited determinants ensure that each excitation is only included once in the expansion.

If no limit is placed on the CI-space, a full CI (FCI) wavefunction can be created, which provides exact Energy solutions to the N_e-electron Hamiltonian eigenvalue problem for the given basis set. However the CI method is computationally intensive and the size of the Hamiltonian matrix increases as more CSFs are included, hence the FCI method is only possible for small systems. Restrictions on the CI-space can however be made in order to carry out calculations on larger systems. Within this work two variations of CI were employed.

2.3.4 Complete Active Space-CI

The CASCI method restricts the full CI expansion by defining which orbitals in the reference determinant are core (always doubly occupied), active (vary in occupancy), and

virtual (always remain unoccupied). The active orbitals of the reference determinant are open for excitations subject only to the limit that all the core spin-orbitals must remain doubly occupied. This limits the CI-space of the calculation. This method is easy to balance with an extra scattering electron, with the resultant energies favouring neither a better ground state nor excitations.

2.3.5 Multi Reference-CI

As opposed to the CI method, in which only one reference determinant was used, the HF ground state Slater determinant, in the MRCI method more than one reference state is used. All excitations (within the CI-space limit imposed) from all reference determinants are then included in the CI expansion. The MRCI method helps to balance the correlation between the ground and excited states, thus improving the excitation energies. It also helps to give a better correlation for the ground state, which is important if it has more than one dominant determinant.

2.3.6 Natural Orbitals

It is normally the convention to use HF spin-orbitals in the CI method to produce the ground state reference determinant, and doing so will result in the CI expansion becoming slowly convergent. However other spin-orbitals may instead be used which may result in the CI expansion converging more quickly. Löwdin (1955) introduced natural orbitals (NOs) as one possibility.

To understand how these are related to HF orbitals we take the first-order reduced density matrix of an N_e-electron system

$$\rho(\mathbf{x}_1, \mathbf{x}_1') = N \int \prod_{i=2}^{N_e} d\tau_i \Phi(\mathbf{x}_1, \mathbf{x}_2, \ldots, \mathbf{x}_{N_e}) \Phi^*(\mathbf{x}_1', \mathbf{x}_2, \ldots, \mathbf{x}_{N_e}), \tag{2.43}$$

which can be expressed in the basis of orthonormal Hartree-Fock spin-orbitals,χ_i, as an expansion:

$$\rho(\mathbf{x}_1, \mathbf{x}_1') = \sum_{i,j} \chi_i(\mathbf{x}_1) \gamma_{ij} \chi_j(\mathbf{x}_1')^*. \tag{2.44}$$

It can be shown (Szabo and Ostlund, 1996) that if Φ is the Hartree-Fock ground state wavefunction Ψ_0,

$$\gamma(\mathbf{x}_1, \mathbf{x}_1') = \sum_{i} \chi_i(\mathbf{x}_1) \chi_i(\mathbf{x}_1')^*, \tag{2.45}$$

γ is Hermitian so it is possible to define an orthonormal basis $\{u_i\}$, which can be related by a unitary transformation to the HF spin-orbitals, such that γ is diagonalised. The elements u_i are the natural spin-orbitals. The new matrix is then expressed as

$$\gamma_{diag} = \sum_i \lambda_i u_i(\mathbf{x}_1) u_i(\mathbf{x}_1')^*, \tag{2.46}$$

where λ_i is the occupation number of u_i. Because of the way in which the equation is defined (with the occupation number as part of the summation), NOs which have a large occupation number will contribute much more to the eigen-energy solution than NOs with only a very small occupation number. Therefore the NOs with low occupations can be removed from the calculation without affecting the results in a significant way.

In this work the MRCI method employed produced NOs for use in scattering calculations, the details of these can be found in (see chapters 5, 6 & 7).

2.3.7 Multi-Configuration Self-Consistent Field Orbitals

It is finally worth noting another type of orbital which may be used in the CI method, the MCSCF variant. Consider a multideterminantal wavefunction which has been restricted to only contain a small number of configurations. In the MCSCF method the orbitals are varied in order to minimize the energy of the configurations they are used to construct. The MCSCF wavefunction is a reduced CI expansion

$$|\Psi_{MCSCF}\rangle = \sum_I c_I |\Psi_I\rangle, \tag{2.47}$$

where both the orbitals contained in $|\Psi_I\rangle$ and the c_I coefficients are optimized. If a single determinant is retained in the expansion, the MCSCF and HF methods become identical (Szabo and Ostlund, 1996). It is finally worth noting that the equations which require solving in order to carry out this method are much more complex than those used to carry out the HF method. The MCSCF method has not been used to produce final results in this thesis, however this method provided the initial orbitals used as input for the MRCI method outlined above.

2.4 Co-ordinate Systems for Theoretical Scattering Calculations

2.4.1 The Fixed Nuclei Approximation

Consider a molecule which follows the Born-Oppenheimer approximation and all its nuclei are fixed in position, thus solving the system's Hamiltonian reduces down to finding the energy eigenvalues and partnering eigenvectors for the electronic Hamiltonian only. When considering a scattering interaction with an incoming electron, one can define a co-ordinate system which simplifies the collision between static target molecule and an electron. Lane (1980*a*) outlined this method.

2.4.2 Definition

A BODY co-ordinate frame is defined so that the principal axis of the molecule lies along the z-axis (where the principal axis of the molecule is the vector direction of its dipole moment. In this work, where the majority of the molecules were linear, this means the z-axis lay along the molecule's length.

A LAB co-ordinate frame can be defined such that the z-axis lies along the momentum vector of the incoming scattering electron. In both co-ordinate frames the origin lies at the center of mass of the target molecule.

If we now consider the system as a whole, with *N* nuclei and *N+1* electrons in total, and define $\{\mathbf{r}_i\}_{i=1}^{N_e}$ and $\{\mathbf{R}_A\}_{i=1}^{N_n}$ to be the vectors describing the positions of the *molecular* electrons and nuclei respectively, and also let $\mathbf{r}_{N+1}$ be the position of the scattering electron in the BODY frame. We can then express the total electron-molecule system's Hamiltonian as

$$\hat{H}_{N+1,elec} = -\frac{1}{2}\nabla^2_{N+1} + \hat{H}_{N,elec} + \hat{V}_{e-mol}, \tag{2.48}$$

where ∇^2_{N+1} is the electron kinetic energy operator and the other terms are defined as follows:

$\hat{H}_{N,elec}$ is the electronic target Hamiltonian

$$\hat{H}_{N,elec} = -\sum_{j=1}^{N_e}\frac{1}{2}\nabla^2_j - \sum_{i}^{N_e}\sum_{A=1}^{N_n}\frac{Z_A}{|\mathbf{r'}_i - \mathbf{R}_A|} + \sum_{i=1}^{N_e}\sum_{j>i}^{N_e}\frac{1}{|\mathbf{r'}_i - \mathbf{r'}_j|}, \tag{2.49}$$

and $\hat{V}_{e-mol}$ is the operator of the electron-molecule interaction potential

$$\hat{V}_{e-mol} = -\sum_{A=1}^{N_n}\frac{Z_A}{|\mathbf{r'}_{N+1} - \mathbf{R}_A|} + \sum_{j=1}^{N_e}\frac{1}{|\mathbf{r'}_{N+1} - \mathbf{r'}_j|}. \tag{2.50}$$

2.4.3 Limitations

These equations, which define the fixed-nuclei (FN) approximation, only hold in conjunction with the BO approximation, in that the collision must happen in a much shorter period of time than the time it would take for the nuclei to move e.g. molecular rotation or vibration. This means the target molecule appears to be fixed in space in respect to the incident electron.

However if the collision time is long, for instance if the incident electron scatters at an energy close to a narrow resonance, the FN approximation will not be applicable. This is also the case if the scattering system has strong long-range interactions e.g. if the target molecule is strongly polar. This leads to the scattering electron being under the influence of the target field for a longer period (thus the collision lifetime is larger).

2.4.4 Frame Transformation

In order to obtain scattering variables such as cross-sections, the FN approximation can be used in conjunction with other methods. The R-matrix scattering method makes use of one such method, frame transformation (Fano, 1970; Chang and Fano, 1972). When using this method, the BODY frame can only be applied in the region close to the nuclei, within some boundary radius. This radius is chosen specifically so that at this boundary the nuclear Hamiltonian is not relevant and the dominant interactions are electron correlation and exchange. However out beyond this boundary region these can also be ignored. Instead, at the boundary a frame transformation takes places changing into the LAB co-ordinate system and asymptotic solutions for the problem are found for the outer region.

2.5 Adiabatic Nuclei Approximation

There are certain conditions in which the boundary of the frame-transformation may be extended to infinity.

- The scattering electron energy is far from the threshold energy.
- No resonances are present.
- There are no significant long range interaction in the system.

If these conditions are met then the extension of the boundary allows the entire problem to be solved within this region. This frame transformation is implemented at the end of a calculation where it is applied to the computed scattering quantities, matrices, and observables.

Chapter 3

Ab-initio R-matrix Theory

3.1 Introduction

The development of the R-Matrix theory began with the work of Wigner (1946) and Wigner and Eisenbud (1947). Initially this was to study nuclear reactions in which a compound state is formed. 30 years later this method was extended for electron-atom scattering in a number of papers (Burke et al., 1971; Robb, 1972; Burke, 1973). Followed shortly after by its application to electron-molecule scattering systems (Schneider, 1975; Schneider and Hay, 1976).

Over the last 30 years the UK R-matrix package has been developed between a number of institutes. This package now exists as the open-source UK Molecular R-Matrix codes (Carr et al., 2012), in both diatomic (Burke et al., 1977) and polyatomic (Morgan et al., 1997) variants, where the former makes use of Slater-type orbitals (STOs), and the latter uses Gaussian-type orbitals (GTOs). These codes have been used to investigate a number of electron scattering problems. Some examples include the SiO close-coupling (CC) studies of Varambhia et al. (2009), the PH_3 static-exchange-plus-polarisation (SEP) study of (Munjal and Baluja, 2007), and the BeH^+ cation (Chakrabati and Tennyson, 2012). Water dimer R-Matrix calculations have also been carried out (Bouchiha et al., 2008; Caprasecca et al., 2009). Much larger systems of the DNA/RNA purine bases (Dora et al., 2012), intermediate-energy scattering on C_2^- using pseudo states (MRMPS) (Halmová et al., 2008) and positron scattering on water (Zhang et al., 2009). Finally there have been recent calculations on positron scattering with C_2H_2 also using MRMPS (Zhang et al., 2011). A comprehensive review article has recently been published (Tennyson, 2010).

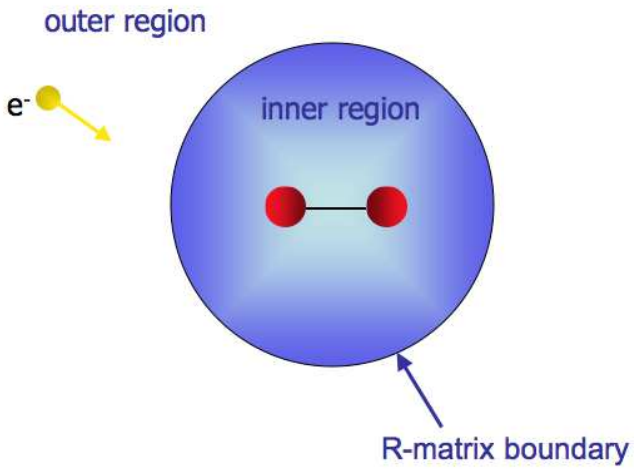

Figure 3.1: Partition of configuration space in fixed-nuclei R-matrix theory

The basis of R-matrix theory is the division of co-ordinate space into inner and outer regions, separated by a boundary of radius a. Fig 3.1 displays this division, where the origin of the co-ordinate system lies at the centre-of-mass of the target. Within the inner region the short-range electron interactions, exchange and correlation, are the dominant effects between the N electrons of the target molecule and the incoming scattering electron. Due to this the $N + 1$-electron system is analogous to a bound state, and the configuration interaction method can be used to produce the $N + 1$ inner region eigenkets. Beyond the R-matrix boundary in the outer region all short-range interactions are assumed to be negligible in comparison to multipole potential created by the N-electron target, hence a single centre expansion of the scattering wavefunction is used in this region. Because of this the problem is reduced into a set of coupled differential equations. These are far easier to solve using mathematical methods.

3.2 The Inner Region Method

3.2.1 The Inner Region Hamiltonian and the Bloch Operator

Within the inner region the $N+1$-electron scattering problem is defined by the time-independent Schrödinger equation (TISE)

$$\hat{H}_{N+1}|\Psi\rangle = E|\Psi\rangle, \tag{3.1}$$

where $\hat{H}_{N+1}$ is the molecular Hamiltonian operator:

$$\hat{H}_{N+1} = \sum_{i=1}^{N+1}\left(-\frac{1}{2}\nabla_i^2 - \sum_A \frac{Z_A}{r_{iA}}\right) + \sum_{i>j=1}^{N+1}\frac{1}{r_{ij}} + \sum_{A>B}\frac{Z_A Z_B}{|\vec{r_A} - \vec{r_B}|}. \tag{3.2}$$

The solution of which is a complete set of basis eigenkets, $|\psi_k\rangle$:

$$|\Psi\rangle = \sum_k A_{Ek}|\psi_k\rangle. \tag{3.3}$$

However non-Hermitian surface terms will be present at the $r = a$ surface. See appendix A for more details of this. In order to keep the operator Hermitian it must be modified with the addition of the Bloch operator:

$$\hat{L}_{N+1} = \sum_{i=1}^{N+1}\delta(r_i - a)\left(\frac{d}{dr_i} - \frac{b}{r_i}\right). \tag{3.4}$$

Where the spherical boundary a is chosen so that the electron cloud of the target is completely contained within. The eigenbases $|\psi_k^\Delta\rangle$ are now defined so that the following holds:

$$\langle\psi_k^\Delta|\hat{H}_{N+1} + \hat{L}_{N+1}|\psi_{k'}^\Delta\rangle = E_k\delta_{kk'}, \tag{3.5}$$

where Δ represents the values of angular momenta corresponding to a particular irreducible representation of the molecule's point group.

3.2.2 The Creation and Definition of the R-Matrix

By introducing the Bloch operator and re-writing, Equation (3.1) can be defined as

$$(\hat{H}_{N+1} + \hat{L}_{N+1} - E\hat{1})|\Psi^\Delta\rangle = \hat{L}_{N+1}|\Psi^\Delta\rangle, \tag{3.6}$$

re-arranging this to give the formal solution

$$|\Psi^\Delta\rangle = (\hat{H}_{N+1} + \hat{L}_{N+1} - E\hat{1})^{-1}\hat{L}_{N+1}|\Psi^\Delta\rangle. \tag{3.7}$$

We can then use the eigenket completeness theorem:

$$\sum_k |\psi_k^\Delta\rangle\langle\psi_k^\Delta| = \hat{1}, \tag{3.8}$$

in order to expand equation (3.7):

$$\begin{aligned} |\Psi^\Delta\rangle &= \sum_{k,k'} |\psi_k^\Delta\rangle\langle\psi_k^\Delta|(\hat{H}_{N+1} + \hat{L}_{N+1} - E\hat{1})^{-1}|\psi_{k'}^\Delta\rangle\langle\psi_{k'}^\Delta|\hat{L}_{N+1}|\Psi^\Delta\rangle & (3.9)\\ &= \sum_{k,k'} \frac{|\psi_k^\Delta\rangle\langle\psi_{k'}^\Delta|\hat{L}_{N+1}|\Psi^\Delta\rangle}{E_k - E}\delta_{kk'} & (3.10)\\ &= \sum_k \frac{|\psi_k^\Delta\rangle\langle\psi_k^\Delta|\hat{L}_{N+1}|\Psi^\Delta\rangle}{E_k - E}. & (3.11) \end{aligned}$$

Comparing this to equation (3.3) we can see

$$A_{Ek} = \frac{\langle\psi_k^\Delta|\hat{L}_{N+1}|\Psi^\Delta\rangle}{E_k - E}. \tag{3.12}$$

3.2.3 Expansion of the Bloch Operator

The Bloch operator may be expanded by a complete basis set, thus we can express it in terms of the channel basis functions $|\psi_i^N Y_{l_i}^{m_i}\rangle$:

$$\frac{1}{2}\sum_{i=1}^{N+1}\sum_{j=1} |\psi_j^N Y_{l_j}^{m_j}\rangle\delta(r_i - a)\left(\frac{d}{dr_i} - \frac{b}{r_i}\right)\langle\psi_j^N Y_{l_j}^{m_j}|. \tag{3.13}$$

If we define the ‘ reduced radial function’

$$F_j(a) = \langle\psi_j^N Y_{l_j}^{m_j}|\Psi^\Delta\rangle, \tag{3.14}$$

and the energy-independent ‘surface amplitudes’,

$$w_{jk}^\Delta(a) = \langle\psi_j^N Y_{l_j}^{m_j}|\psi_k^\Delta\rangle, \tag{3.15}$$

and

$$w_{jk}^\Delta(a)^\dagger = \langle\psi_k^\Delta|\psi_j^N Y_{l_j}^{m_j}\rangle. \tag{3.16}$$

By substituting (3.13) into (3.12), and applying our new definitions, we can state

$$A_{Ek} = \frac{1}{2}\sum_{j=1} \frac{(w_{jk}^\Delta(a))^\dagger\left(F_j'(a) - ba^{-1}F_j(a)\right)}{E_k - E} \tag{3.17}$$

where the integrations are carried out across all $N+1$ electronic spin-space co-ordinates in the inner region, excluding the radial co-ordinate of the scattering electron.

Substituting this into equation (3.3), The total wavefunction Ψ^{Δ} can be expressed as

$$\Psi^{\Delta} = \frac{1}{2}\sum_{k,j}\frac{w_{jk}^{\Delta}(a)^{\dagger}\left(F_j'(a) - ba^{-1}F_j(a)\right)}{E_k - E}\psi_k^{\Delta}. \tag{3.18}$$

From this the R-matrix can be calculated, this is done by projecting (3.18) onto a channel $|\psi_i^N Y_{l_i}^{m_i}\rangle$ and evaluating the term on the R-matrix boundary, where $r = a$:

$$R_{ij}^{\Delta}(E) = \frac{1}{2a}\sum_{k}\frac{w_{ik}^{\Delta}(a)(w_{jk}^{\Delta}(a))^{\dagger}}{E_k - E}. \tag{3.19}$$

The R-matrix supplies the boundary condition for applying the Schrödinger equation to the outer region correctly. Within it is contained the surface value of the scattering wavefunction and the its derivative-matching surface boundary condition.

3.2.4 The Trial Inner Region Scattering Wavefunction

In the inner region the close-coupling trial wavefunction

$$\psi_k^{\Delta}(\mathbf{X}_{N+1}; R) = \hat{A}\sum_{i=1}\sum_{j=1}a_{ijk}^{\Delta}\Phi_i^{\Delta}(\mathbf{X}_N; \hat{\mathbf{r}}_{N+1}\sigma_{N+1})\eta_{ij}^0(\mathbf{x}_{N+1}) + \sum_{l=1}\chi_l^{\Delta}(\mathbf{X}_{N+1})b_{lk}^{\Delta}, \tag{3.20}$$

is used to represent $|\psi_k^{\Delta}\rangle$ where $\mathbf{X}_{N+1} = \{\mathbf{x}_i\}_{i=1}^{N+1}$ and $\mathbf{x}_i = \mathbf{r}_i\sigma_i$ is the spin-space coordinate of the i^{th} electron. Φ_i^{Δ} is the wave function of the ith target state, and it along with the continuum orbitals η_{ij}^0 (which represent the scattering electron) and square integrable functions χ_i^{Δ} depend parametrically on the geometry R. $\hat{A}$ is the antisymmetrisation operation which is applied to ensure that the wavefunction is antisymmetric with respect to interchange of any two electrons.

Φ_i^{Δ} are formed from fixed-nuclei electronic target states spin-coupled to the angular and spin functions of the scattering electron (see above). In the polyatomic suite these channel functions and the quadratically integrable functions χ_i^{Δ} are constructed from GTOs (Gaussian-type orbitals) centred on the nuclei. The target electronic wavefunctions can be created using either the Hartree-Fock or configuration-interaction method previously discussed.

The first summation runs over the electronic target states. It represents a situation where one electron exists in the continuum states, with the remaining N electrons remaining in the target state, and is known as a 'target+continuum' configuration.

Continuum basis functions, of the form $f_{il_i}(\mathbf{r}) = \frac{1}{r}u_{il}(r)Y_{l_i}^{m_i}(\theta, \phi)$, and target molecular virtual orbitals are combined to produce the continuum orbitals. The radial part of

the wavefunction, u_{il}, is numerically generated as a solution of a second order ordinary differential equation:

$$\left[\frac{d^2}{dr^2} - \frac{l(l+1)}{r^2} + 2V_0(r) + k_i^2\right] u_{il}(r) = 0, \tag{3.21}$$

where u_{il} is based on the expansion of GTOs (Faure et al., 2002*a*).

Finally, to construct the continuum orbitals, $\eta^0_{il_i}(\mathbf{r}_{N+1})$, the continuum basis functions $\{f_{il}\}$ are firstly orthogonalised to the target orbitals using the Schmidt orthogonalisation procedure. Then, to remove linear dependence problems between the functions a Löwdin orthogonalisation is used (Tennyson, 2010). This problems can arise as two independent basis sets are being used to describe both the target and the continuum. As basis sets increase in size they will increasingly cover the same (function) space and therefore become linearly dependent.

These continuum orbitals are used to create the R-Matrix boundary amplitudes, w, described previously in equation (3.15):

$$w^{\Delta}_{ik}(a) = \sum_{j=1} \eta^0_{ij}(a) a^{\Delta}_{ijk}. \tag{3.22}$$

The second term of equation (3.20) sums over χ^{Δ}_i configurations in which all the electrons are contained only within the target molecular orbitals. In order to include correlation effects, such as excitations to higher states not included in the first terms summation, the L^2 functions are introduced. This is to ensure that important parts of the configuration space are not excluded.

Diagonalisation of $\hat{H}_{N+1} + \hat{L}_{N+1}$ using the $|\psi^{\Delta}_k\rangle$ inner region basis (as found in equation (3.5)) provides the a^{Δ}_{ijk} and b^{Δ}_{lk} co-efficients. The evaluation of the matrix elements in equation (3.5) can be carried out using adapted quantum chemistry methods. This adaptation allow for the integrals to be carried out over a finite range and also allow the inclusion and treatment of the continuum orbitals as well as the standard Gaussian or Slater type orbitals.

3.3 The Outer Region Method

3.3.1 Outer Region Eigenfunctions

In the external region the outer region wavefunction is expressed as an expansion, using the channel functions $\psi_i^N Y_{l_i}^{m_i}$ as the basis:

$$\Psi^{\Delta}(\mathbf{X}_{N+1}) = \sum_{i=1} \psi_i^N Y_{l_i}^{m_i} \frac{F_i^{\Delta}(r_{N+1})}{r_{N+1}}. \tag{3.23}$$

These are eigenfunctions of the Hamiltonian and describe the solutions where there is no interaction between the incident electron and the target molecule. This is because an interaction radius is chosen, beyond which all short-range exchange and correlation effects between the scattering electron and the electrons of the target molecule vanish.

The wavefunctions ψ_i^N are created by the coupling of a molecular target state Φ_i^N to the scattering electron spin σ_{N+1}. Due to the interaction boundary discussed above there is no need for the inclusion of an antisymmetrisation operator, as the scattering electron is in its own independent region. Also because this region is completely separate from the target the L^2 and χ_i^{Δ} functions seen in equation (3.20) also vanish. It is therefore possible to use single-centre reduced radial wavefunctions, $F_i^{\Delta}(r_{N+1})$, to represent this electron.

A set of second order coupled ordinary differential equations can be created from these. This is done by substitution of $\Psi^{\Delta}(\mathbf{X}_{N+1})$ into the TISE (equation (3.1)) followed by a projection of both sides onto the channel basis (appendix B). These equations

$$F_{\lambda}^{\Delta\prime\prime} - \frac{l_\lambda(l_\lambda+1)}{r_{N+1}^2} F_{\lambda}^{\Delta} + 2(E-E_\lambda)F_{\lambda}^{\Delta} = 2\sum_{\lambda'} V_{\lambda\lambda'} F_{\lambda'}^{\Delta}, \tag{3.24}$$

are satisfied by the reduced radial wavefunctions $F_i^{\Delta}(r_{N+1})$.

This set of equations are solved for the range $[a, a_p]$, where $r = a$ represents the boundary between internal and external regions, and $r = a_p$ defines the boundary between the external and the asymptotic regions of the calculation space. The differential equations are also restricted by boundary conditions at the interface between internal and external regions ($r = a$):

$$F_i^{\Delta}(a) = \sum_j R_{ij}^{\Delta} \left(a F_j'(a) - b F_j(a) \right), \tag{3.25}$$

and the R-matrix equation (3.19), as discussed in Burke et al. (2007).

Propagation of the R-matrix

There are standard method for solving these equations at each interval of a (e.g. Burke and Seaton (1971)). These methods solve the equations at the $r = a$ region interface, and propagate outwards by dividing the external region (where $a \leq \ r \leq \ a_p$) into a set of p sub-regions. The $F_i^{\Delta}(r_{N+1})$ can be expanded within each sub-region, using a basis of Legendre polynomials (Baluja et al., 1982). By applying this method to propagate through each subsequent sub-region the R-matrix can be determined at the external/asymptotic region boundary, $r = a_p$. Now that the R-matrix is known at each of the sub-region boundaries, the reduced radial wavefunction can be obtained across each region.

The Asymptotic Region

Careful selection of the size of a_p ensures that it is large enough for the solution to equation (3.24) to be represented by the asymptotic boundary conditions. For open channels:

$$F_{ij}^{\Delta} \sim \frac{1}{\sqrt{k_i}} \left[\sin\left(k_i r - \frac{l_i \pi}{2}\right) \delta_{ij} + \cos\left(k_i r - \frac{l_i \pi}{2}\right) K_{ij}^{\Delta} \right], \tag{3.26}$$

where i,j are in-, out-channels respectively, and for closed channels:

$$F_{ij}^{\Delta} \sim e^{-|k_i| r}. \tag{3.27}$$

The K-matrix can then be determined by matching to the open channel boundary condition, this matrix will have dimensions $n_o \times n_o$, where n_o is the number of open channels at each scattering energy within the range defined in the calculation.

Scattering Observables

The K-matrix can be used to provide a quantity known as the eigenphase sum, this can be used as a diagnostic tool for the scattering calculation, providing information on scattering resonances and channel-opening thresholds. In order to obtain this quantity a new matrix is first created from the diagonalisation of the K-matrix, $\mathrm{diag}(K_1^{\Delta}, K_2^{\Delta}, \ldots, K_{n_o}^{\Delta})$. The arctangent of the diagonal elements are then summed over all channels that have been retained in the outer region part of the calculation:

$$\eta^{\Delta}(E) = \sum_i \arctan K_i^{\Delta}. \tag{3.28}$$

This quantity is generally plotted against incident scattering energy and a number of recognisable features may be determined by examination of these plots. A number of examples are presented in this work.

The K-matrix can also be linked to the S- and T- matrices respectively using the following relations:

$$\mathbf{S}^{\Delta} = (1 + i\mathbf{K}^{\Delta})(1 - i\mathbf{K}^{\Delta})^{-1}, \tag{3.29}$$

$$\mathbf{T}^{\Delta} = \mathbf{S}^{\Delta} - \mathbf{1} = (2i\mathbf{K}^{\Delta})(1 - i\mathbf{K}^{\Delta})^{-1}. \tag{3.30}$$

These are used to determine a number of scattering observables from the calculation. E.g. The excitation cross-section for the electronic transition $i \rightarrow i'$ is defined as

$$\sigma(i \rightarrow i') = \frac{\pi}{k_i^2} \sum_{\Delta} \frac{2S+1}{2(2S_i+1)} \sum_{l_\lambda m_\lambda l_{\lambda'} m_{\lambda'}} |T^{\Delta}_{\lambda\lambda'}|^2. \tag{3.31}$$

And also the T-matrices are used in the spin-coupled rotational cross-section work presented in the the next chapter.

3.3.2 Resonances

Resonances describe the temporary trapping of an electron to form a quasibound or short-lived state. They can primarily be seen as a feature or enhancement of the cross-section at a certain energy. Resonance features have both a position E_r, and due to the Heisenberg uncertainty principle, a width Γ_r (where both of these features are measured in terms of the scattering electron energy).

A number of electron-molecule processes are driven by resonances, such as dissociative attachment (Domcke, 1991), and dissociative recombination (Florescu-Mitchell and Mitchell (2006), Larsson and Orel (2008)). It is also common in almost all scattering processes for resonances to lead to an enhancement of cross-sections, for example vibrational excitation due to electron impact (Domcke, 1991).

There are different types of resonances, each is characterised by a different theoretical treatment.

Shape resonances occur when the electron becomes trapped behind a barrier in the potential of the electron-molecule system. Usually this barrier is the centrifugal one caused by the angular momentum of scattering electron. Because of this *s*-wave scattering cannot create shape resonances. Another common way of understanding this process is that the electron occupies a low-lying unoccupied electron orbital in the target molecule, this is often the energetically lowest unoccupied molecular orbital (LUMO).

Shape resonances are typically short lived, and as such they have a broad width as a function of energy when they appear in scattering observables. If the bond length of the target molecule increases beyond equilibrium shape resonances can become bound states. This occurs as the energy position of the resonance will decrease with increasing bond length. Eventually this causes the position to become negative on the energy axis, with the width also decreasing to zero (Rabadán and Tennyson (1996), Rabadán and Tennyson (1997)).

Feshbach resonances (Feshbach, 1958, 1962) occur when there is simultaneous electronic excitation of the target molecule with the incoming electron also becoming trapped. Hence a normally occupied orbital is now a hole and two virtual orbitals become occupied. The electronically excited state is known as the parent state, and these types of resonances are normally classified as Feshbach or core-excited resonances, depending on whether the resonance position lies below or above this parent state. They are also generally narrower than shape resonances and thus have a longer life-time. At the end of this life-time a Feshbach resonance will decay to a lower-lying excited state, and a core-excited resonance will decay back to the parent state or the ground state. Feshbach resonances also provide a direct route to dissociative recombination (Larsson and Orel, 2008).

A simple way to differentiate between shape and Feshbach resonances in a scattering calculation is to perform it once using a single-state target and once using a multi-state target. Resonances that appear in both will be shape, and those only appearing in the multi-state calculation will be Feshbach (as target excitations are allowed).

Nuclear-excited Feshbach resonances can only occur in molecules, unlike the previously discussed types. These occur when the $N+1$ electron system has a weakly bound state, and appear at very low energies with a narrow width. With this type of resonance the excitation is caused by vibrational excitation or nuclear motion of the molecule, hence the treatment must go beyond the Born-Oppenheimer approximation to investigate these correctly. Resonances of this type can lead to complicated structures near thresholds, and investigations have been made into their effect upon vibrational (Morgan et al. (1990), Thummel et al. (1993)) and rotational (Pfingst et al. (1992), Thummel et al. (1992)) excitation processes.

Finally another type of resonance may be present in scattering calculation results, *Pseudo* resonances. These are spurious resonances which occur when an incomplete

theoretical model is used. In principle these occur when an open channel which lies within the energy range of the calculation is omitted. Technically the means of coupling to this channel must also be present in order to cause the pseudo resonances, hence static exchange calculations do not find them despite only using the ground state of the target. Generally this type of resonance is better avoided due to the unnecessary complication it adds to the calculation results. However sometimes their presence is utilised, for instance in R-matrix calculations at intermediate energies (Burke et al. (1987), Scholz (1991)).

Determining the precise values of resonance positions and widths is a key objective for many electron scattering calculations, and in the UK molecular R-matrix codes the module RESON (Tennyson and Noble, 1984*a*) is used to initially detect resonances from the eigenphase sums and then apply a fit to determine a position and width. Resonance detection used the fact that the eigenphase sum, (3.28)) shows a rapid jump by π radians. RESON then fits this using a Breit-Wigner formula (Breit and Wigner, 1936) to obtain the resonance parameters.

$$\eta^{\Delta}(E) = \eta^{\Delta}_{bg} + \eta^{\Delta}_{res} \tag{3.32}$$

$$= \eta^{\Delta}_{bg}(E) + \arctan \frac{\Gamma_r}{E_r - E}, \tag{3.33}$$

where $\eta_{bg}(E)$ is the background phase.

This method is however sometimes limited, the Breit-Wigner form cannot fit overlapping resonances, or those features lying near to a channel-threshold. This problem occurs because as the size of the energy range of the fit increases, there will be an increase in the variation of the background eigenphase sum, η^{Δ}_{bg}. The resulting assumptions then made about the background phase will mean uncertainties are introduced for this fit. In this work it was found that sometimes the fitting failed and as such a manual fit was taken by eye, examples of this can be found in the results for CN, C_3N, and C_2H.

3.3.3 T-matrix Transformations

All R-Matrix calculations in this thesis have been carried out on linear molecules (with the exception of the e^--O work). These molecular calculations have all been carried out in C_{2v}, the highest Abelian sub-group of the natural group $C_{\infty v}$.

However in order to calculate spin-coupled rotational cross-sections as described in the next chapter, T-matrices in the natural group, $C_{\infty v}$, are required. Hence we had to transform the fixed nuclei T-matrices output from the calculations from C_{2v} back to their $C_{\infty v}$ natural group.

Λ_0	m_{l_i}	Λ_s
	0	$^2\Sigma^+$
$^2A_1$	2	$^2\Delta$
	4	$^2\Gamma$
	1	$^2\Pi$
$^2B_1$	3	$^2\Phi$
	1	$^2\Pi$
$^2B_2$	3	$^2\Phi$
	0	$^2\Sigma^-$
$^2A_2$	2	$^2\Delta$
	4	$^2\Gamma$

Table 3.1: Rule for transforming a C_{2v} T-matrix of symmetry Λ_0 to a $C_{\infty v}$ one with symmetry Λ_s

Linear molecules have Hamiltonians which have $C_{\infty v}$ symmetry, so the group elements g commute with the Hamiltonian:

$$g\hat{H}\tilde{g} = \hat{H} \quad \forall g \in C_{\infty v}. \tag{3.34}$$

These group elements correspond to an infinitesimal rotation about the z axis, and commute with $\hat{H}$. Because of this the z-projection of the angular momentum $\Lambda_{t,s}$ is a constant of motion for both the N- and $N+1$-molecular Hamiltonian respectively (However $\Lambda_t = 0$ for Σ^+ ground state targets in this work). Transforming the T-matrix in the $C_{\infty v}$ representation from the existing C_{2v} one merely extracts those T-matrix elements with $m_{l_i} = \Lambda_s$. Table 3.1 gives the rules for creating the $C_{\infty v}$ symmetries from the C_{2v} ones.

3.4 The UK Molecular R-Matrix Codes: Structure and Outline

All work carried out in this thesis uses the polyatomic R-Matrix codes (Morgan et al., 1998*a*). This code package comprises of modules which are run in order to carry out a full electron-scattering calculation. The inner region part of the package is built upon the Sweden-Molecule quantum chemistry suite of Almlof and Taylor (1984), using these existing codes to generate the molecular orbitals of the target and also the transformed

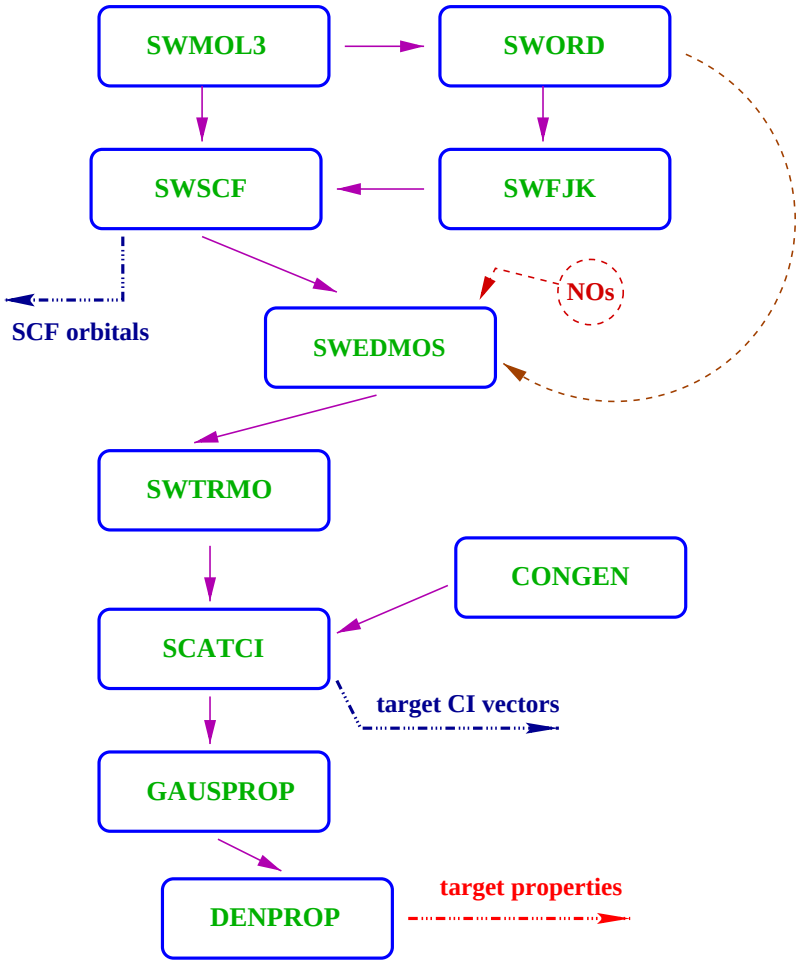

Figure 3.2: R-matrix inner region flow diagram for the target calculation

integrals. The number of outer region modules has increased over time as code users have introduced new functionality into the suite. Recently the code package has undergone an update and renewal to introduce uniform coding standards and practices across the suite, the codes now exist as a collaborative project between institutions under the name UKRMOL (Carr et al., 2012).

The structure and running order of the target, the inner region scattering, and the outer region scattering parts of the code are outlined in figures 3.2, 3.3 and 3.4 respectively.

3.4.1 Target and Inner Region Scattering

- **SWMOL3**: generates one and two-electron integrals from the given GTO basis set, in the code these are input in SUPERMOLECULE format as found via (Schuchardt et al., 2007);

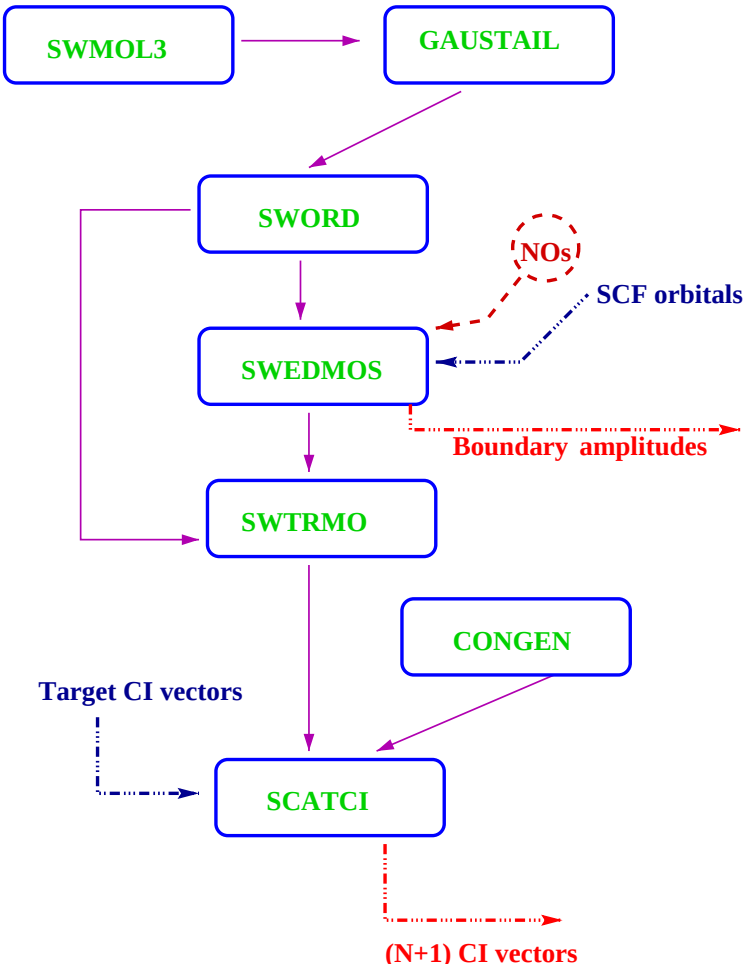

Figure 3.3: R-matrix inner region flow diagram for the calculation of the $(N+1)$ scattering eigenket $|\psi_k^{\Delta}\rangle$ (equation (3.20))

- **GAUSTAIL**: adusts the integrals over atomic orbitals for the finite dimension of the R-Matrix sphere by adding matrix elements of the Bloch operator to the Hamiltonian ones (Morgan et al., 1997);
- **SWORD**: orders the atomic integrals evaluated by SWMOL3;
- **SWFJK**: forms combinations of Coulomb and exchange integrals for building the Fock matrix;
- **SWSCF**: carries out the Hartree-Fock (see section 1.3.1) process to generate the target molecular orbitals from linear combinations of atomic ones. Here it employs the integrals obtained from the SWFJK code;
- **SWEDMOS**: constructs molecular orbitals and boundary amplitudes for the target wavefunction and also the continuum. It also applies the Schmidt orthogonali-

sation so that each continuum orbital is orthogonalised to all the target ones, and symmetric orthogonalisation to orthogonalise the continuum orbitals among themselves. A deletion threshold (with a generally accepted value of 10^{-7}) is employed for orbital deletion. Those continuum orbitals with overlap matrix eigenvalues less than this threshold are deleted. This is also the point in the codes at which external molecular orbitals can be introduced from, e.g. MOLPRO (for examples see sections 5.3, 6.3 & 7.3);

- **SWTRMO**: transforms the atomic orbitals to the four-index molecular orbital representation of the ordered integrals produced by SWMOL3;

- **CONGEN**: produces configuration state functions (CSFs) of the correct spin and symmetry coupling. In the case of a static-exchange calculation, only one (ground state) configuration is produced, however for configuration interaction (CI) calculations many tens of thousands of CSFs can be produced. It also generates prototype CSFs for the $(N+1)$-electron system. CONGEN also solves phase factor problems that arise from the use of CI expansions (Tennyson, 1997);

- **SCATCI**: performs a CI calculation of the target molecular and the $(N+1)$-complex wavefunctions (Tennyson, 1996) using the CSFs produced by CONGEN. Diagonalisation of the Hamiltonian takes place to obtain the CI expansion coefficients (eigenkets) and the corresponding eigenvalues. The output from this is the pole energies of the R-Matrix equation (3.19);

- **GAUSPROP**: generates the property integrals required by DENPROP;

- **DENPROP**: constructs the transition density matrix from the target eigenvectors obtained from the CI calculation. From this it then calculates the multipole transition moments $M_l^m(\lambda \rightarrow \lambda')$ required for solving the outer region coupled equations (3.24), the dipole spherical polarisability α_0, and where possible the diagonalised tensor components α_{xx}, α_{yy} and α_{zz}, which are computed using second-order perturbation theory and the property integrals. Only multipole moments up to and including $l = 2$ are computed, and together with the target Hamiltonian eigenenergies (figure 3.2), they are saved to a target properties file for later use in the outer region (figure 3.4);

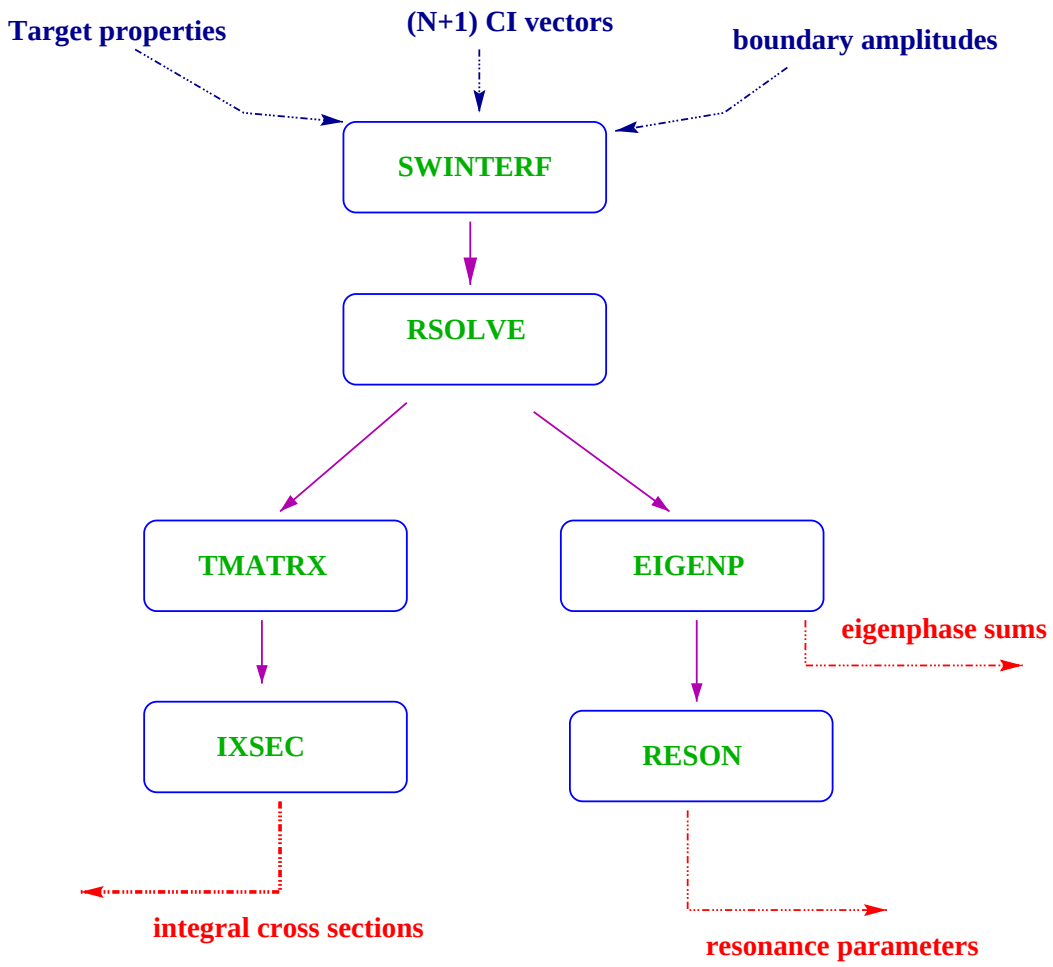

Figure 3.4: R-matrix outer region flow diagram

3.4.2 Outer Region

- **SWINTERF**: the interface between the internal and outer regions. It uses the boundary amplitudes from SWEDMOS, the $N+1$-system eigenvectors and their corresponding eigenvalues and the molecule's multipole moments (figure 3.4). The output contains data needed in order to rapidly construct the R-matrix initially at the interaction radius as a function of energy;

- **RSOLVE**: constructs the R-matrix at the interaction radius and uses RPROP (Morgan, 1984) to propagate this R-matrix to the asymptotic region for matching to the boundary condition there (equation (3.26)) by solving the coupled ordinary differential equations (3.24) in an outer region which is divided into sectors. It then constructs the fixed-nuclei K-matrices (Noble and Nesbet, 1984);

- **EIGENP**: calculates the multichannel eigenphase sum by diagonalising the K-

matrix and summing over channels (equation (3.28));

- **RESON**: detects resonances and performs a least squares fit of the eigenphase sums to a Breit-Wigner profile (Tennyson and Noble, 1984*a*) (See section 2.3.2);
- **TMATRX**: calculates the T-matrices from the K-matrices using equation (3.30);
- **IXSEC**: computes the integral cross sections from the T-matrices;
- **TMATSUB**: transforms the C_{2v} FN T-matrices to $C_{\infty v}$ as discussed in section 3.4.4;
- **ROTLIN**: using the ANR approximation it computes rotationally resolved integral cross sections from the $C_{\infty v}$ T-matrices. Also computing and including the Born correction for $|\Delta J| = 1$. It was adapted from the existing ROTIONS code (Rábadan and Tennyson, 1998*a*), which computes the same for cations, and invokes the Coulomb-Born approximation. This programme is the forerunner to **ROTLIN_S**, which has been created to calculate spin-coupled rotationally resolved integral cross-sections.

Other outer region modules exist for calculating other scattering observables, e.g. differential cross-sections, multi-channel quantum defects. However these modules were not used in this work. Details of other outer region modules can be found in Tennyson (2010).

3.5 Contributions to the R-matrix Package

3.5.1 ROTLIN_S

In order to calculate the spin-coupled rotationally resolved integral cross-sections outlined previously (section 1.6), it was necessary to adapt the existing outer region module ROTLIN (Faure et al., 2007) to incorporate spin coupling. The original code was based upon the work of Rabadán et al. (1998*b*) which detailed rotational cross-sections from body frame T-matrices. The adaptations made to this code have been outlined in the next chapter.

3.5.2 KMATADGENERAL

In the outer region, the module **RSOLVE** produces K-matrices and outputs them into files for storage and re-use. In order to save space and I/O processing time only the upper triangle of the matrix is stored (as the actual K-matrices are symmetric). However some subsequent outer region programmes require the K-matrices in square format, such as polyDCS, for calculating differential cross-sections (Sanna and Gianturco, 1998).

A number of 'KMATAD' modules had previously been written in order to return the triangular matrices to the full, square, format. Each version of the module had been specifically made for different symmetries, as and when it was required. Over time this led to many versions within the outer region suite.

After some investigation it was discovered the only difference in these versions was the number of input files looped through for conversion. E.g. for the C_{2v} symmetry the code looped through 4 triangular K-matrix input files, for the A1, B1, B2 and A2 K-matrices respectively.

In order to provide one version of the module to work for all symmetries, the loop over input files was simply adapted to run across the number of symmetries provided in the namelist. This then meant that a single version of the program could be used for all cases.

3.6 Quantemol-N

Due to the number of modules that must be run in order to carry out a full R-Matrix calculation, the process from start to finish can take long periods of time to set up. Each module has its own namelist input, the variables in this namelist can depend on the results of the previous parts of the calculation. This has historically led to some of the more complex CI calculations taking up the entire duration of a PhD.

Also when considering the variations possible in the calculations, such as different basis sets or complete active spaces, it is clear that in order to optimise a calculation to obtain the best results, it is better to test a number of models for the system.

In order to make the creation and running of the R-Matrix codes far easier, a java-based GUI wizard system has been created, Quantemol-N (Tennyson et al., 2007). This has enabled non-specialist users to be able to quickly setup and run electron-molecule scattering R-Matrix calculations of which they may not have any experience.

3.6.1 Manually Running the R-Matrix Codes

As hinted at above, when creating an R-Matrix calculation a number of variables must be chosen for the system:

- Geometry and symmetry of the system.
- Target and continuum basis sets.
- The R-Matrix radius.
- The type of molecular orbitals used.
- The electron distribution through these orbitals for both the target model and the inner region CI problem.
- The deletion threshold for the continuum orbitals.
- The scattering energy grid.
- The number of target states retained in the outer region calculation.
- The R-Matrix propagation distance.
- Further outer region module options (e.g. Resonance fitting parameters etc..).

3.6.2 The Quantemol-N Approach

By automating much of the selection of these options behind-the-scenes, Quantemol-N can be used to create R-Matrix calculations from only a select few input variables:

- Geometry co-ordinates of the system.
- Symmetry of the system (aided with graphics to ensure a suitable option is chosen).
- Electron configuration of the target (a default initial guess is provided which can be changed if required).
- Type of model to be used (Hartree-Fock static exchange or configuration-interaction close coupling).
- Basis set for the target molecule (a library of stock basis sets is included for non-experts).

- R-Matrix radius (aided by graphics to ensure whole system is enclosed by R-Matrix sphere), this then defines the continuum basis set to be used for representing the scattering electron (Faure et al., 2002*b*).
- For CI calculations: Number of states per symmetry calculated for the target and number of orbitals retained in the complete active space.
- Scattering energy grid (a default option is provided which can be changed if required).

By taking these few inputs, the software automatically produces the correct inputs and runs all the modules required to produce a full calculation, presenting the results afterwards as part of the GUI.

3.6.3 Use of Quantemol-N in this Work

All of the work presented started in some way with an initial R-Matrix calculation using Quantemol-N. In each case initial studies were taken using a range of different basis sets until a model was found which was deemed to represent the system well.

In the cases of NaI (chapter 9) and $SiBr_n$ (chapter 10) the final Quantemol-N results obtained were tested using multiple models until a convergence was found to consistent results (given the lack of literature with which to compare these species with).

However in the cases of CN, C_3N & C_2H, (chapters 5, 6 & 7) there were a number of factors which led to the decision to extend the model beyond the capabilities of Quantemol-N. In these cases the jobfiles produced automatically by the software were used as a starting point, with changes and extensions being made to them in order to make the calculation more advanced. For these species, when calculating the target, it was necessary to move away from the HF-SCF orbitals produced by the R-Matrix module SCF and into natural orbitals produced by the MRCI method from the MOLPRO software (Werner et al., 2008). This procedure is now used regularly in R-Matrix calculations but is currently beyond Quantemol-N.

Finally, whilst it is possible theoretically to calculate electron-atom scattering using the polyatomic R-Matrix codes (and thus Quantemol-N), we believe the Oxygen results presented in this work (chapter 8) to be the first attempt at it. This led to a number previously unconsidered problems which would not normally occur when carrying out standard electron-molecule scattering using the codes. These considerations are outlined

in chapter 8 along with their solutions. Because of these again extension beyond the Quantemol-N calculations was required in order to proceed. Here we simply took the jobfiles produced by the software and manually made changes to solve the problems faced, before running as a standard R-Matrix calculation.

Chapter 4

Electron-Impact Spin-Coupled Rotational Cross-Sections - A New Theory

This chapter has been substantially published as Harrison et al. (2012)

4.1 Introduction

Electron collisions provide a route to excitation in even weakly ionised plasmas. While most plasmas are not studied at rotational resolution, this is not true of the cold astronomical plasmas in the interstellar medium (ISM), that form both dense and diffuse molecular clouds. Electron molecule collisions are important in other astronomical environments including planetary nebulae, cometary tails and planetary aurora. Thus, for example, rotational emission spectra have been used to provide the most direct estimate available of the electron density in a shocked region of the ISM (Jimenez-Serra et al., 2006) and hence to study differences in the behaviour of ionised and neutral molecules (Roberts et al., 2010).

Given that none of the environments mentioned above are in local thermodynamic equilibrium (LTE), electron collision cross sections are required to model any observed emission due to electron impact excitation. The laboratory measurement of electron impact rotational excitation cross section is extremely challenging and very few such measurements are available. This has placed the onus on theory to provide the necessary data.

R-matrix calculations, combined with a Coulomb-Born treatment for high electron angular momenta, were originally developed for the treatment of electron collisions with

linear molecular ions (Rabadán et al., 1998*b*,*a*; Rabadán and Tennyson, 1998*b*; Lim et al., 1999; Faure and Tennyson, 2001). Comparison of calculations performed for several species showed that while for systems with dipoles larger than about 2 Debye, excitations with $\Delta J = 1$ are both completely dominant and well-treated by the Coulomb-Born formula of Chu and Dalgarno (1974*b*), transitions with $\Delta J \neq 1$ are important for less polar molecules and such systems require the detailed treatment of short-range interactions provided by the R-matrix methodology.

The work on linear was subsequently extended to non-linear ions (Faure and Tennyson, 2002*b*,*a*) and neutral molecules (Faure et al., 2004). Electron impact rotational excitation with a number of closed-shell linear molecules has been considered including HCN and HNC (Faure et al., 2007), SiO (Varambhia et al., 2009) and CS (Varambhia et al., 2010). For the HCN system, Faure et al. (2007) extended the theoretical treatment to allow for hyperfine effects. The data on electron impact rotational excitation of neutral and ionised molecules of astrophysical interest is gathered in the BASECOL database (Dubernet et al., n.d.).

The difficulty of measuring rotational excitation cross sections makes it hard to assess independently the reliability of the cross sections mentioned above. However evidence from experimental studies on cooling of HD^+ by electrons (Shafir et al., 2009) and electron collisions with water (Faure et al., 2004; Itikawa and Mason, 2005; Curik et al., 2006; Zhang et al., 2009), as well as comparison with detailed close-coupling calculations (Faure et al., 2006), all point towards the reliability of this procedure.

So far all the studies considered above have only treated closed systems. Open shell species introduce new sources of angular momentum in the collision system and therefore require a generalisation of the methodological developments described above. In this work we re-formulate the theory of electron impact rotational excitation for the case of a linear molecule with total electron spin angular momentum, S, greater than zero. In this we follow the work of Corey and McCourt (1983), who considered collisions between a $^{2S+1}\Sigma^+$ linear molecule and an atom in a ^1S state. As an electron has $s = 1/2$, it is necessary to consider an extra spin in our treatment.

Spin-coupling has been taken into account for a number of different physical situations. From probing Zeeman effect in magnetic fields (Radford and Broida, 1962), to studying the cosmic microwave background radiation (Roth et al., 1993; Leach, 2012). Spin-rotation coupling also plays an important role in ultra-cold physics (Guillon and

Stoecklin, 2007).

Currently we know of no other computation implementations for calculating spin-coupled rotational cross-sections driven by electron impact, however there has been recent work published on spin-inclusive rovibrational cross-sections for atom-molecule systems (Lopez-Duran et al., 2008). Similarities exist with this work in that the atom in question is treated as structureless, which is also the initial assumption for the projectile used here.

4.2 Method

The initial starting point of this theory is the work of Corey and McCourt (1983), whose work outlined the calculation of cross-sections for a collision between a $^{2S+1}\Sigma$ linear molecule and an atom in a ^1S state, using a Hund's case (b) coupling scheme. The general idea is that the electron spin is only weakly coupled to the molecular rotation and it plays a spectator role in the collision dynamics. In such a treatment, the dynamical problem is reduced to a spin-free problem where the energy splitting of the spin multiplets is neglected and the spin wave functions are decoupled from the rotational wave functions using a recoupling scheme. This "recoupling" approach is adapted at collisional energies much larger than the energy splittings, which are typically below 1 meV for doublet and triplet targets. In order to implement collisions with electrons, the spin of the projectile needs to be incorporated into the coupling scheme of the existing work.

4.2.1 Coupling in Case when the Projectile is Spinless

Using the general case of Corey and McCourt (1983), We adapt the angular momentum coupling scheme to include a spin-1/2 electron projectile. Using the definitions from Corey & McCourt (CM):

- $\mathbf{N}$ is the rotational angular momentum of molecule;
- $\mathbf{S}$ is the electron spin angular momentum of the molecule;
- $\mathbf{j} = \mathbf{N} + \mathbf{S}$ is the total angular momentum of the molecule;
- $\mathbf{l}$ is the orbital angular momentum of the projectile;
- $\mathbf{J} = \mathbf{l} + \mathbf{j}$ is total angular momentum of the compound system.

CM use a total-J basis represented by the coupling scheme, eq. (CM2.10):

$$\mathbf{N}+\mathbf{l}=\mathcal{J},\mathcal{J}+\mathbf{S}=\mathbf{J}. \tag{4.1}$$

This basis is defined through eq. (CM2.11)

$$|(Nl)\mathcal{J}S;JM\rangle=\sum_{m,m_S}(-1)^{-\mathcal{J}+S-M}[J]^{1/2}\begin{pmatrix}\mathcal{J} & S & J\\ \mathcal{M} & m_s & -M\end{pmatrix}|Nl\mathcal{J}\mathcal{M}\rangle\,|Sm_s\rangle\,, \tag{4.2}$$

where $|Nl\mathcal{J}\mathcal{M}\rangle$ is defined by eq. (CM2.12)

$$|Nl\mathcal{J}\mathcal{M}\rangle=\sum_{m_N,m_l}(-1)^{-N+l-\mathcal{M}}[\mathcal{J}]^{1/2}\begin{pmatrix}N & l & \mathcal{J}\\ m_N & m_l & -\mathcal{M}\end{pmatrix}|Nm_N\rangle\,|lm_l\rangle\,, \tag{4.3}$$

where the $[x]$ is used to represent a factor of $(2x+1)$.

Thus if one has T-matrices in the $|Nm_N\rangle\,|lm_l\rangle$ basis, they can be converted to the $|Nl\mathcal{J}\mathcal{M}\rangle$ basis using the above, subject to the condition $\mathcal{J}=\mathbf{N}+\mathbf{l}$.

4.2.2 Case when the Projectile has Spin=1/2

The above case of coupling can be adapted by redefining some variables and adding a new one to define the projectile electron spin. In this new coupling scheme the spin momenta and non-spin momenta are calculated in parallel before being combined in the final coupling stage.

- $\mathbf{N}$ is rotational angular momentum of molecule.
- $\mathbf{S}_m$ is electron spin angular momentum of the molecule.
- $\mathbf{s}$ is spin of projectile electron, $\mathbf{s}=1/2$.
- $\mathbf{S}$ is total spin angular momentum of the system, $\mathbf{S}=\mathbf{S}_m+\mathbf{s}$.
- $\mathbf{j}$ defined as previously, $\mathbf{j}=\mathbf{N}+\mathbf{S}_m$.
- $\mathbf{l}$ is angular momentum of the projectile.

In this case we still use eq. 4.1:

$$\mathbf{N}+\mathbf{l}=\mathcal{J},\mathcal{J}+\mathbf{S}=\mathbf{J}. \tag{4.4}$$

but with a generalised definition of $\mathbf{S}$:

$$\mathbf{S}=\mathbf{S}_m+\mathbf{s}=S_m\pm 1/2. \tag{4.5}$$

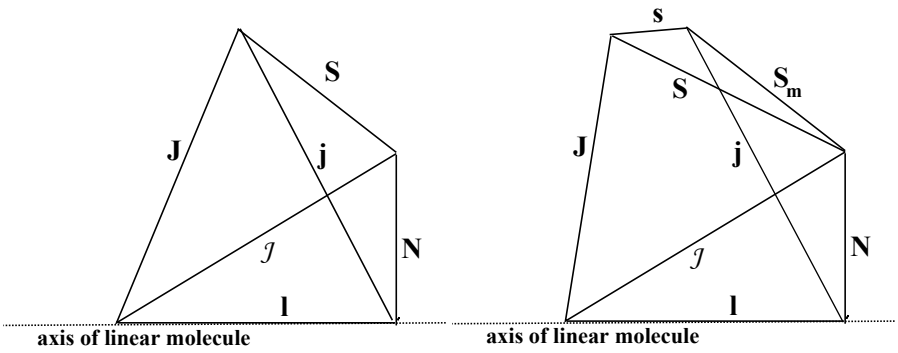

Figure 4.1: Comparison of the old (Corey and McCourt (1983), left) and new (right) coupling schemes.

Both schemes are shown in fig. 4.1, note the difference in definition of molecular spin, **j** and **J** between the original (left) and the new (right) schemes. Figure 4.1 also provides the triangulation limits on the summations in eqs. 4.6 to 4.8 below.

Within our chosen coupling scheme, the spin and other angular momenta are coupled separately and then joined. Therefore the electron scattering T-matrices can be transformed by using eq. 4.3, before including the extra weighted summation over S arising from the need to consider projectile spin. Adapting eq. (CM2.27):

$$T^{JS}_{N'j'l',Njl} = \sum_{\mathcal{J}} (-1)^{j'-l'-j+l} [\mathcal{J}][j',j]^{1/2} \left\{ \begin{array}{ccc} S & N & j \\ l & J & \mathcal{J} \end{array} \right\} \left\{ \begin{array}{ccc} S & N' & j' \\ l' & J & \mathcal{J} \end{array} \right\} T^{\mathcal{J}S}_{N'l',Nl}, \tag{4.6}$$

where the superscript S notation shows that the total electron spin is treated as a constant of motion for a given T-matrix.

4.2.3 Rotational Cross-Sections

Once the T-matrices have been transformed to the necessary basis, the scattering observables can be calculated using the following equations. Eq. (CM2.28) gives the scattering amplitude from state $NSjm$ to state $N'Sj'm'$:

$$
\begin{aligned}
& f(N'Sj'm'\leftarrow NSjm|\hat{R}) \\
= & \left(\frac{\pi}{kk'}\right)^{1/2} \sum_{Jll'm_{l'}} i^{l-l'+1}[l]^{1/2}[J] \begin{pmatrix} j & J & l \\ m & -m & 0 \end{pmatrix} \begin{pmatrix} j' & J & l' \\ m' & -m & m_{l'} \end{pmatrix} T^{JS}_{N'j'l',Njl} Y_{l'm_{l'}}(\hat{R}) \\
= & \left(\frac{\pi}{kk'}\right)^{1/2} \sum_{Jll'm_{l'}} \sum_{\mathcal{J}} i^{l-l'-1}(-1)^{j'-l'-j+l}[\mathcal{J}J][jj'l]^{1/2} \begin{Bmatrix} S & N & j \\ l & J & \mathcal{J} \end{Bmatrix} \begin{Bmatrix} S & N' & j \\ l' & J & \mathcal{J} \end{Bmatrix} \\
\times & \begin{pmatrix} j & J & l \\ m & -m & 0 \end{pmatrix} \begin{pmatrix} j' & J & l' \\ m' & -m & m_{l'} \end{pmatrix} T^{\mathcal{J}S}_{N'l',Nl} Y_{l'm_{l'}}(\hat{R}). \qquad (4.7)
\end{aligned}
$$

Finally, the integral cross-section for a given S is given by eq. (CM2.30):

$$
\begin{aligned}
\sigma^S(N'j'\leftarrow Nj) &= \frac{\pi}{(2j+1)k^2} \sum_{Jll'} [J] |T^{JS}_{N'j'l'\leftarrow Njl}|^2 \\
&= \frac{\pi}{k^2} \sum_{\mathcal{J}\mathcal{J}'} \sum_{Jll'} [J\mathcal{J}'\mathcal{J}j'] \begin{Bmatrix} S & N & j \\ l & J & \mathcal{J} \end{Bmatrix} \begin{Bmatrix} S & N' & j' \\ l' & J & \mathcal{J} \end{Bmatrix} \\
&\quad \times \begin{Bmatrix} S & N & j \\ l & J & \mathcal{J}' \end{Bmatrix} \begin{Bmatrix} S & N' & j' \\ l' & J & \mathcal{J}' \end{Bmatrix} T^{\mathcal{J}\mathcal{S}}_{N'l',Nl} T^{\mathcal{J}'S*}_{N'l',Nl}. \qquad (4.8)
\end{aligned}
$$

However a weighted summation over S is required to obtain the observable cross-section

$$
\sigma(N'j'\leftarrow Nj) = \sum_{S=|S_m-s|}^{S_m+s} \frac{(2S+1)}{n} \sigma^S(N'j'\leftarrow Nj), \qquad (4.9)
$$

with

$$
n = \sum_{S=|S_m-s|}^{S_m+s} (2S+1). \qquad (4.10)
$$

This summation is not required in the original theory of Corey and McCourt (1983), as there is only a single value of S in their scheme.

4.3 The Infinite Order Sudden Approximation

Spin-coupled cross-sections may also be obtained through manipulation of the pure rotational cross-sections using the Infinite Order Sudden approximation (IOS). This approximation is very similar to the Adiabatic Nuclei Rotation (ANR) approximation in the electron-molecule literature (Lane, 1980*b*). This latter was employed in all previous R-matrix studies, combined with the Born or Coulomb-Born theory (see references in section 4.1). The ANR and IOS approximations consist of assuming that the target rotational states are degenerate, which is valid when the rotational spacings are negligible

with respect to the collisional energy. Within such a treatment, the sum of cross-sections over a final state is independent of the initial state. The IOS or ANR approximation was shown to be valid down to threshold in the case of the electron-H_3^+ system (Faure et al., 2006), owing to the strong Coulomb field which ensures that the time scale for electron motion is always rapid compared to nuclear motion. In the case of a neutral target, the IOS approach is expected to fail at threshold, and a kinematic correction is usually employed (see below). Corey and McCourt (1983) have shown that within the IOS approximation, the spin-coupled or fine structure cross sections can be directly obtained from the "fundamental" pure rotational cross sections, i.e. those out of the lowest $N = 0$ level. In practice, this is the method used below to calculate our data.

Rabadán et al. (1998*b*) describe how to calculate rotational cross-sections using T-matrices produced by the R-matrix method (Tennyson, 2010), employing the ANR approximation to allow the body-frame T-matrices to be transformed to the laboratory frame:

$$T^{\mathcal{J}S}_{N'l',Nl} \approx \sum_{\Lambda=-l}^{l} A^{\mathcal{J}\Lambda}_{N',l'} T^{\Lambda S}_{l',l} A^{\mathcal{J}\Lambda}_{N,l}, \tag{4.11}$$

where Λ is the projection of l over the nuclear axis and where

$$A^{\mathcal{J}\Lambda}_{N,l} = \sqrt{\frac{2N+1}{2\mathcal{J}+1}} C(Nl\mathcal{J}; 0\Lambda - \Lambda), \tag{4.12}$$

where $C(.)$ is a Clebsch Gordan coefficient. From these, the integrated rotational cross-sections are then calculated using:

$$\sigma^{RM}(N' \leftarrow N) = \frac{\pi}{(2N+1)k_i^2} \sum_{\mathcal{J}=0}^{\infty} \sum_{l=|\mathcal{J}-N|}^{\mathcal{J}+N} \sum_{l'=|\mathcal{J}-N'|}^{\mathcal{J}+N'} (2\mathcal{J}+1) \, |T^{\mathcal{J}S}_{N'l',Nl}|^2, \tag{4.13}$$

where k_i is the initial momentum of the electron. In practice, the partial-wave expansion is truncated to some finite maximum value of l. This formulation has been implemented in the Fortran program ROTLIN, written by Faure et al. (2007). We have used the ROTLIN program to produce the pure rotational cross-sections for this work, subsequently calculating the spin-coupled data using the IOS approximation outlined in Corey and McCourt (1983).

Within the IOS approximation, the spin-coupled, degeneracy-averaged integrated cross-sections are given by eq. (CM4.11):

$$\begin{aligned} \sigma^S(N'Sj' \leftarrow NSj) &= \sum_{\lambda=0}^{N+N'} [N'Nj'] \begin{pmatrix} N' & N & \lambda \\ 0 & 0 & 0 \end{pmatrix}^2 \begin{Bmatrix} \lambda & j & j' \\ S_m & N' & N \end{Bmatrix}^2 \\ &\quad \times \sigma^S(\lambda \leftarrow 0), \end{aligned} \tag{4.14}$$

where $\sigma(\lambda \leftarrow 0)$ is defined explicitly by

$$\sigma^S(\lambda \leftarrow 0) \equiv \frac{\pi}{k_i^2} \sum_{l'l} \frac{[l'l]}{[\lambda]} \begin{pmatrix} l' & l & \lambda \\ 0 & 0 & 0 \end{pmatrix}^2 |T_\lambda^{lS}|^2. \tag{4.15}$$

This is equivalent to the pure rotational cross-section out of the lowest $N = 0$ level, for a given S

$$\sigma^S(\lambda \leftarrow 0) \equiv \sigma^S(N' \leftarrow 0). \tag{4.16}$$

The total cross section is then obtained using Eq. (4.9).

Using this method we have generalised on the code ROTLIN to the create ROTLIN_S which implements this IOS approximation method to add the spin-coupling to the pure rotational cross-sections. This is done by specifying the required values of j and j' as user input, where they can take the values

$$|N - S_m| \leq j \leq N + S_m, \tag{4.17}$$

and

$$|N' - S_m| \leq j' \leq N' + S_m, \tag{4.18}$$

in integer steps of j, j'.

The original ROTLIN code also implemented a Born correction for $\Delta N = 1$ transitions, this is especially important when the dipole moment of the molecule is large (say $\gtrsim 1$ D) and the Born cross-section becomes dominant (Faure et al., 2004). In this case, the standard procedure is to use the dipolar Born approximation to obtain the cross-section for the high partial waves not included in the body-frame T-matrices (Norcross and Padial, 1982). The resulting $\Delta N = 1$ spin-rotation cross-sections produced also incorporate the Born correction correctly.

Finally, as mentioned above, the expected unphysical behaviour of the IOS cross-sections near rotational thresholds was corrected using a simple kinematic ratio (Chang and Temkin, 1969; Rabadán et al., 1998*b*) which forces the excitation cross-sections to zero at the rotational threshold:

$$\sigma^{final}(N'j' \leftarrow Nj) = \frac{k_f}{k_i} \sigma(N'j' \leftarrow Nj), \tag{4.19}$$

where k_f is the final momentum of the electron, which is equal to zero at threshold. The exact threshold law is however not known. We note that threshold as well as closed-

channel effects can only be included rigorously in full close-coupling calculations (Faure et al., 2006).

4.4 Testing the IOS Approximation

Corey and McCourt (1983) showed that a consequence of the IOS approximation is that cross sections for any transition $N' \leftarrow N$ can be deduced from the fundamental rotational cross sections $\sigma(\lambda \leftarrow 0)$. Namely eq. (CM5.8),

$$\sigma(N' \leftarrow N) = \sum_{\lambda=0}^{N+N'} [N'] \begin{pmatrix} N' & N & \lambda \\ 0 & 0 & 0 \end{pmatrix}^2 \sigma(\lambda \leftarrow 0), \tag{4.20}$$

where $\sigma(\lambda \leftarrow 0)$ are the pure rotational cross-sections out of the $N = 0$ level. This property can thus be tested in the present context. Indeed, in the above treatment the IOS approximation was combined with both a Born and a threshold correction and the rotational spacings were thus taken into account in the final cross sections. Also the above sum over lambda is limited by the maximum of N and N' but is truncated in practice. Hence the above IOS property, eq. (4.20), should not be fulfilled. However, if in practice the departure from eq. (4.20) is small, as expected at high collision energy, the above IOS treatment for spin-coupled cross sections should be reliable.

Recently Harrison and Tennyson (2012) published electron-collision data on the molecular radical CN using the R-matrix method. The T-matrices produced during these calculations are used here to calculate spin-rotational cross-sections from 0.1 to 4 eV. We use this example to test whether the IOS approximation holds, and also to produce some initial spin-rotational cross-sections for CN (see next section). Figure 4.4 presents comparisons of the directly calculated $\sigma(N' \leftarrow N)$ pure rotational cross-sections, which include the Born and threshold corrections, with those calculated using the IOS eq. (4.20) above for a number of transitions.

Clearly there is excellent correlation between the two calculations for all transitions. The slight discrepancies at low energy (lower than $\sim 25\%$) can be explained because *i)* the target rotational levels are not treated as degenerate in the Born regime and *ii)* the rotational thresholds are included in the full calculation through the kinematic ratio, eq. (4.19). However there is in general an excellent correlation between the two calculations, demonstrating that eq. (4.20) and by extension eq. (4.14) is reliable. We therefore conclude that the IOS approximation is applicable in the energy regime investigated and

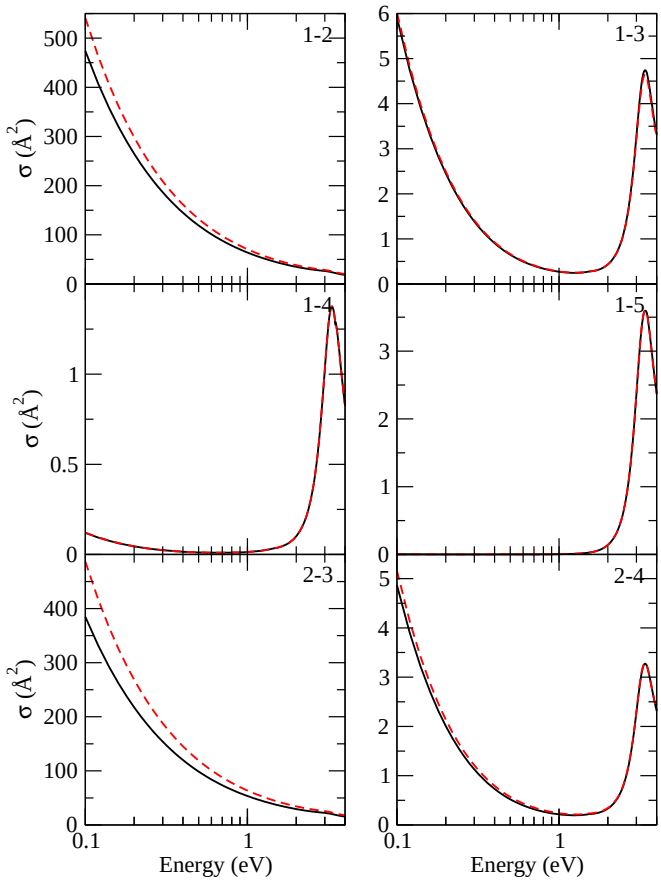

Figure 4.2: Electron-impact rotational excitation of CN ($N \rightarrow N'$) calculated using the full theory (solid) and the IOS approximation, Eq. 4.20 (dashed).

can be used to simplifying the full spin-coupling theory. We note that at lower energy, it is possible to improve the IOS approach by scaling the IOS spin-recoupled cross sections by the pure rotational cross sections, as done by Faure et al. (2007) for the hyperfine rate coefficients of HCN. Full details about this scaling procedure, which becomes necessary for collision energies below 0.1 eV owing to the failure of the IOS assumption, will be discussed elsewhere.

4.5 Conclusions

Here is presented a new theory of calculating spin-coupled rotational cross-sections for electron collisions with neutral linear molecules in a $^{2S+1}\Sigma^+$ ground state. This is based on the initial work of Corey and McCourt (1983), who outlined the details of a ^1S atom colliding with a linear molecule in a $^{2S+1}\Sigma^+$ ground state. This work has already provided the equations required for calculating the state to state differential, and integrated

cross-sections from the collision T-matrices of the appropriate basis. By introducing projectile spin to represent the colliding electron, and coupling this to the target molecule spin, we have presented an altered coupling scheme which can still be used in the existing theoretical framework.

However, by applying the IOS approximation, we are able to greatly simplify the theory to obtain the spin-coupled cross-sections by simple manipulation of the pure rotational data. The viability of using this approximation has been tested using existing input T-matrices from electron-CN scattering calculations (Harrison and Tennyson, 2012), and found to be applicable in this scheme. The use of IOS approximation has also enabled a successful integration into the existing ROTLIN Fortran program, which calculates pure rotational cross-section using the T-matrix output from an electron-molecule scattering calculation using the R-matrix method (Tennyson, 2010). This has led to the development of the new ROTLIN_S program, which enables the spin-coupled cross-sections to be calculated with the addition of new user input which will be implemented as a module within the UK Molecular R-matrix code (section 3.4).

4.6 Example Results

A full set of example results for the CN spin-rotation cross-sections, and conclusions to these results, can be found in section 5.7.

Chapter 5

CN

This chapter has been substantially published as Harrison and Tennyson (2012).

5.1 Introduction

The CN radical (fig 5.1) is a well known and a well studied molecule, particularly through its spectra. A review of previous work on this can be found in the introduction of (Liu et al., 2001). CN is found in numerous environments, ranging from the sun's atmosphere Porfireva (1975), the interstellar medium Krelowski et al. (2011) to terrestrial plasmas and within flames Halpern et al. (1996). It was also one of the first molecules used to study the cosmic microwave background Thaddeus (1972); Kaiser and Wright (1990), and is still studied today Leach (2012).

Information on electron scattering is important as such collisions may cause electronic excitations. This produces the electronic emission spectra crucial in identifying the molecule in a range of environments. Modelling these spectra requires knowledge of appropriate electronic excitation mechanisms. Here we consider the interactions between the target radical and the scattering electron and, in particular, the first two excitations of molecular CN, the $X^2\Sigma^+$-$A^2\Pi$ and $X^2\Sigma^+$-$B^2\Sigma^+$ transitions. These give rise to the 'CN red' and 'CN violet' spectral bands.

The anionic form, CN^-, is also the smallest molecular anion to be have been observed in space (Agundez et al., 2010). This detection used observations of the $J = 2 - 1$ and $J = 3 - 2$ rotational transitions in the envelope of carbon star IRC +10216; these transitions were recently measured experimentally in the laboratory by Gottlieb et al. (2007). Here CN^- was found in high abundance. 0.25%, relative to neutral CN, in

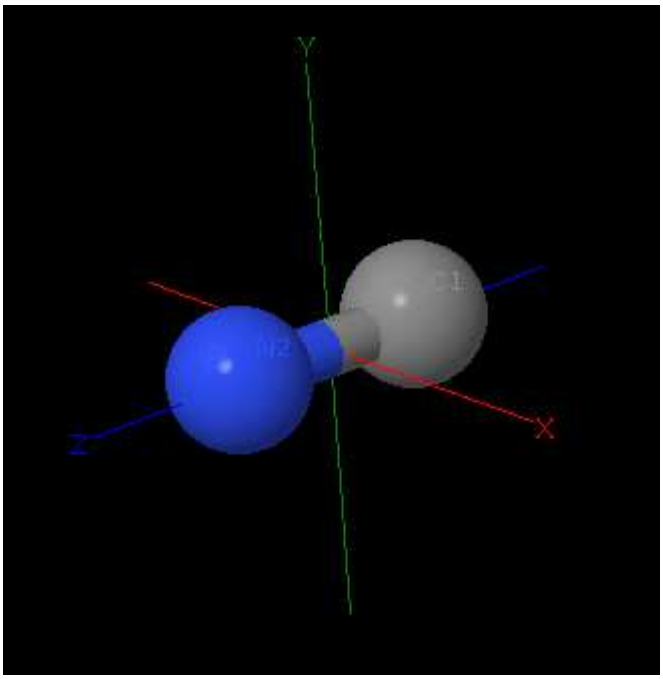

Figure 5.1: The molecule CN (taken from Quantemol-N)

comparison to the extremely small abundance of C_2H^- relative to its neutral in the same region. The reason for the relative sparseness of C_2H^- in comparison to other observed small linear carbon chains is discussed in chapter 7. As the rate of formation of the anion due to radiative electron attachment is very slow for the smallest carbon chains, such as CN^-, here we investigate the possibility that the formation rate is enhanced by very weakly bound anion states. This mechanism has been proposed for the linear, carbon-chain anions recently detected in space (Herbst and Osamura, 2008).

Surprisingly, given its importance, there is very little previous work on electron collisions with CN. Experimental electron collision studies are common for stable diatomics (Brunger and Buckman, 2002) but difficult for radicals and we are unaware of any for CN. Many theoretical methods are not constrained by the need for a stable target structure, including the one we present below. However the only calculated e^--CN collision cross sections are due to Joshipura and Patel (1994), who considered total cross sections at high energies (100 – 1000 eV). Our work therefore represents the first study of low-energy electron collision behaviour with the CN radical.

5.2 Method

The scattering calculations reported here were performed using the UK molecular R-matrix codes Morgan et al. (1998*b*). In order to simplify the calculation, the Quantemol-N interface (section 3.6) has been used for models 1–4 (see the Target Calculations section for details on these models). Non-Quantemol calculations used molecular orbitals different from the standard Hartree-Fock (HF) orbitals which the R-Matrix codes produce. To produce these non-standard orbitals the quantum chemistry software MOLPRO of Werner et al. (2008) has been used to calculate and output natural orbitals (NOs), via the multi-reference configuration interaction (MRCI) method.

Scattering calculations were performed at two levels: static exchange (SE), and close coupling (CC). The presence of low-lying excited target states meant that the widely used one-state static exchange plus polarisation model was deemed inappropriate for this study, as this method is prone to give pseudo-resonances at energies above the first electronically excited target state. Calculations were carried out with an R-Matrix radius of 15 a_0, this was to ensure all of the more diffuse augmented basis set used are entirely enclosed within the R-matrix sphere.

All calculations were initially performed at the CN equilibrium geometry 1.1718 Å, and ignored effects due to nuclear vibrational motion.

We note that although CN is linear, neither the polyatomic R-matrix codes nor MOLPRO use $C_{\infty v}$ symmetry. All calculations were therefore performed using C_{2v} symmetry but identifying the results in $C_{\infty v}$ proved to be straightforward and these symmetry labels are largely used below.

5.3 Target Calculations

A variety of models were tested at r_e when calculating results for the neutral CN target, a selection of these are shown in table 5.2. Models 1 – 4 were carried out using the R-Matrix expert system Quantemol-N. These comprised of HF and Complete Active Space Configuration-Interaction (CAS-CI) calculations. Two basis sets, cc-pVTZ and aug-cc-pVTZ, were also used for each method. For the CAS-CI calculations an orbital space of 7,2,2 (for symmetries a_1, b_1, b_2) has been used. Mapping to 7 σ and 2 π orbitals in $C_{\infty v}$. Eight electrons were frozen in the 1 – 4σ orbitals with five active electrons distributed amongst the 5 – 7σ and 1 – 2π. Model 5 used this CAS-CI model but the

Table 5.1: Results of the aug-cc-pVTZ R-matrix target tests run using various weighted NOs produced by Molpro, and their comparison to the standalone Molpro quantum chemistry calculation and experimental data.

Weighting ($^2\Sigma^+$:$^2\Pi$)	X $^2\Sigma^+$ (H)	μ (D)	A $^2\Pi$ (eV)
1:0	-92.384	1.42	1.71
5:1	-92.381	1.61	1.52
5:2	-92.380	1.74	1.45
1:1	-92.370	1.93	1.34
Molpro	-92.586	1.28	1.32
Thompson and Dalby (1968)		1.45	
Huber and Herzberg (1997)			1.15

molecular orbitals used in the calculation were the NOs produced by MOLPRO. For this model the scattering calculations were performed using the R-Matrix codes manually, to allow for use of these orbitals. The NOs were state averaged from 3 separate MRCI calculations, one for each of the $^2A_1$, $^2B_1$ and $^2B_2$, ($^2\Sigma^+$ and $^2\Pi$) states, using the MOLPRO 'MATROP' facility. The weighting chosen for each state in the average was (using the above order of states) 5:1:1. This weighting was chosen as the pure $^2\Sigma^+$ (1:0:0) MRCI orbitals gave a vertical excitation energy which is too high but reproduced the experimental dipole moment excellently, and the equally state averaged (1:1:1) orbitals made the dipole moment too high by 0.5 Debye, although this model reproduced the vertical excitation energy found in the literature excellently. Because of this it was deemed that a weighting be used which approximated both parameters to a good degree without sacrificing the quality of one to improve the other. Having excitation energies too high would cause a shift in the threshold of the subsequent excitation cross-sections produced. Also when the Born correction is applied to these excitation cross-sections, the correction's magnitude depends fundamentally on the square of the dipole moment. Hence approximating both of these molecular properties to a good degree is important to obtain a target which will lead to accurate scattering observables being produced in the finished calculation. Table 5.1 shows the full details of Molpro NO study.

There have been a number of previous *ab initio* studies on CN; Table 5.2 compares our models with the best of these. As we only use a very limited correlation space, the other studies give lower absolute energies even for calculations which use the same target basis. Our dipole moment for our final model gives agreement within 10% against the calculation of Kalcher (2002) and the experimental values of Thompson and Dalby (1968)

Table 5.2: Selected calculated target properties of CN. All results are for the equilibrium geometry of CN. The calculated absolute energies of the X $^2\Sigma^+$ ground state are given in Hartree while the vertical excitation energy to the low-lying electronic states is given in eV. μ is the ground state dipole moment, given in Debye. See text for details of models.

Model	Basis	Orbitals	Method	X $^2\Sigma^+$	μ	A $^2\Pi$	B $^2\Sigma^+$
1	cc-pVTZ	SCF	HF	-92.217	2.260		
2	cc-pVTZ	SCF	CAS-CI	-92.290	1.167	1.538	3.910
3	aug-cc-pVTZ	SCF	HF	-92.218	2.307		
4	aug-cc-pVTZ	SCF	CAS-CI	-92.221	2.230	2.142	7.023
5	aug-cc-pVTZ	NOs	CAS-CI	-92.381	1.612	1.515	3.491
Thogersen and Olsen (2004)	cc-pVDZ		FCI	-92.493			
Berente et al. (2002)	DZP	ROHF	CCSD	-92.508			
Sordo (2001)	CBS limit		CCSDT	-92.606			
Ajitha and Hirao (2001)	ANO		RCCSD			1.106	
Shi et al. (2011)	AV5Z		MRCI+Q+CV+RE			1.141	3.194
Kalcher (2002)	cc-pVQZ		CAS-ACPF		1.44	1.141	
Polak and Fiser (2002)	aug-cc-pVQZ		CASSCF-MRCI		-1.44		
Thompson and Dalby (1968)			Experiment		1.45		
Huber and Herzberg (1997)			Experiment			1.151	3.197

and Polak and Fiser (2002). Absolute values of the dipole moment have been given, and in all cases the direction points towards the Nitrogen atom. Our predictions for the vertical energy of excitation for the low-lying state are systematically too high for all models based on Hartree-Fock orbitals. Use of NOs greatly improves this situation; with these orbitals our excitation energies are 0.6 eV and 3.5 eV closer to the experimental values than model 4, which used Hartree-Fock orbitals but the same basis set. The best theoretical results, from the recent paper of Shi et al. (2011), benefit from having the Davidson correction applied as well as including relativistic effects and core-valence correlation into the calculations. Note that the experimental excitation energies, taken from Huber and Herzberg (1997), are corrected to change from adiabatic to vertical excitation energies. This raises the original adiabatic values by some 0.06 eV (A) and 0.001 eV (B) giving vertical excitation energies given in the table.

5.4 Scattering Calculations

Our scattering calculations provide a number of scattering observables, including total elastic and excitation cross-sections, eigenphase sums and resonance data, and detection of anionic bound states. Three classes of model were tested: SE based on a single target

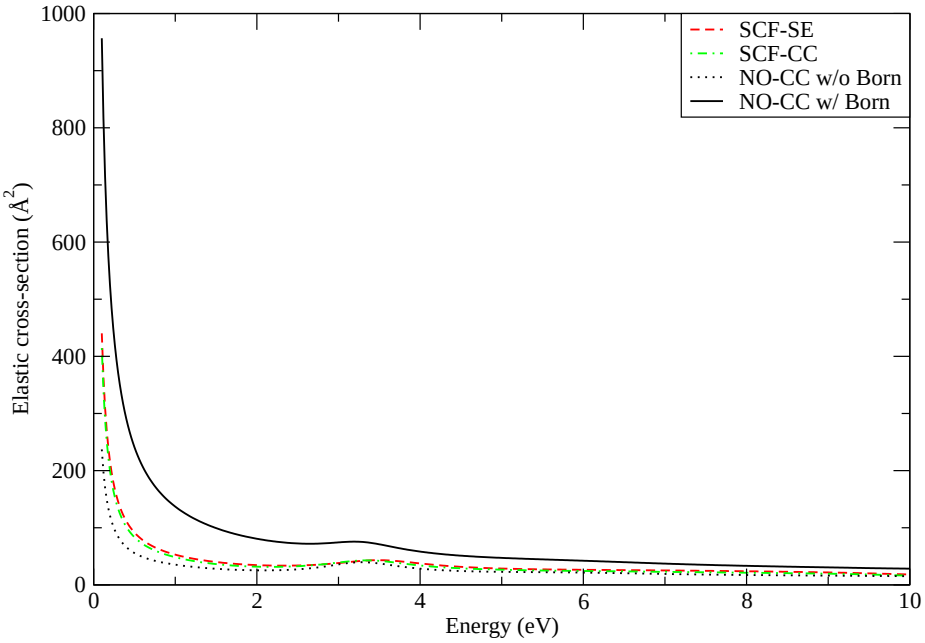

Figure 5.2: Elastic Cross-Section for electron CN collisions

state and using Hartree-Fock orbitals (the SCF-SE method), and two CC models where 48 state calculations (with the target composing of doublet and quartet states and 6 states per symmetry) were performed in the inner region. Of the two CC models, one used Hartree-Fock orbitals (SCF-CC), and the other used the MRCI natural orbitals produced in MOLPRO (NO-CC).

Outer region calculations were performed retaining those target states which lie below 10 eV for the CC calculations, the Quantemol-N default setting. This means 16 and only 4 states were kept for models 2 and 4 respectively, and 15 for model 5. The results reported below are insensitive to increasing these numbers.

5.4.1 Cross-sections

Figure 5.4 presents the total elastic cross-section of CN for electron scattering energies up to 10 eV, for all 3 models with the aug-cc-pVTZ basis set, SCF-SE, SCF-CC and NO-CC. For the final NO-CC model, a Born correction was applied due to the dipolar nature of the molecule, which acts to increase the cross-section at all energies.

Electron impact electronic excitation cross sections are given by the many-state CC calculations. Figure 5.5 shows the cross-sections representing the excitation from the $^2\Sigma^+$ ground state of the neutral to the first two excited states, A $^2\Pi$ and B $^2\Sigma^+$. Here the Born correction is applied to both excitations as they are both dipole allowed transitions;

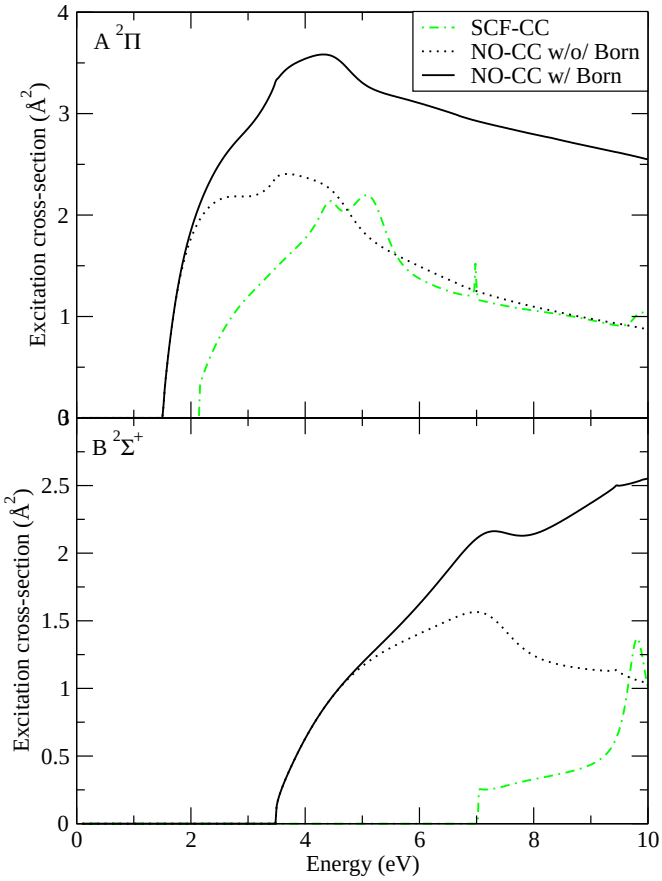

Figure 5.3: Electron impact electronic excitation cross sections for CN final state: A $^2\Pi$, B $^2\Sigma^+$

for clarity we only give corrected results for our calculation based on the use of NOs. The Born correction is small near threshold but becomes significant at higher collision energies, presumably as higher partial waves become important. Both excitation cross sections show resonance features. The biggest difference between models is caused by the shift in excitation threshold. Since the NO-based calculation gives excitation energies which agree more closely with experiment than the SCF-based calculations, these must be regarded as our best estimate for the electronic excitation cross section.

5.4.2 Bound anionic states

Bound state energies were calculated by searching at negative scattering energies using the outer region program BOUND (Sarpal et al., 1991). For these calculations only the low-lying X $^2\Sigma^+$ and A $^2\Pi$ were retained in the outer region of the CC calculations, since experience has shown that strongly closed states can cause such outer region calculations to be numerically unstable. These were propagated to a distance of 30.1 a_0. Table 5.3 summarizes the results of these studies. All models found only a single bound state.

Table 5.3: CN^- bound states with energies given in eV. All calculations are for the equilibrium geometry of CN

Model	Basis	Orbitals	Method	$^1\Sigma^+$ Binding energy
This work/1	cc-pVTZ	SCF	SE	2.594
2	cc-pVTZ	SCF	CC	3.485
3	aug-cc-pVTZ	SCF	SE	2.571
4	aug-cc-pVTZ	SCF	CC	3.820
5	aug-cc-pVTZ	NOs	CC	3.407
Thogersen and Olsen (2004)	cc-pVDZ		FCI	3.527
Midda and Das (2004)	aug-cc-pVTZ		HF/DF B3LYP	4.04
Polak and Fiser (2002)	aug-cc-pVQZ		CASSCF-MRCI	3.58
			w/Davidson	3.75
Ortiz (1998)	6-311++G(d,p)	UHF	2MBPT	3.83
Berkowitz et al. (1969)			experiment	3.82±0.02
Klein et al. (1983)			experiment	3.821±0.004
Bradforth et al. (1993)			experiment	3.86±0.003

The SE calculations give a vertical binding energy of about 2.6 eV whereas for the CC calculations this binding energy is increased to between 3.4-3.8 eV. This figure is in good agreement with the full configuration interaction electronic structure calculations of Thogersen and Olsen (2004).

The use of density functional theory (Midda and Das, 2004) gives an energy of 4.04 eV, 0.6 eV higher than our value despite using the same basis set. The NO-CC binding energy of our final model is some 0.4 eV less than both the calculated SCF-CC and the measured values; however the measured binding energies quoted are adiabatic and will therefore be larger than our calculated vertical ones. The work of Polak and Fiser (2002) agrees within 5% of our best value despite their use of a larger basis set, however once the Davidson correction had been applied the result moved away from our results towards the experimental values. Finally the best theoretical results come from the second order many body perturbation theory of Ortiz (1998), who matches the experimental values excellently.

5.4.3 Resonances

Resonances were characterised using a Breit-Wigner fit to the eigenphase sums as implemented in the automated detection and fitting program RESON (Tennyson and Noble,

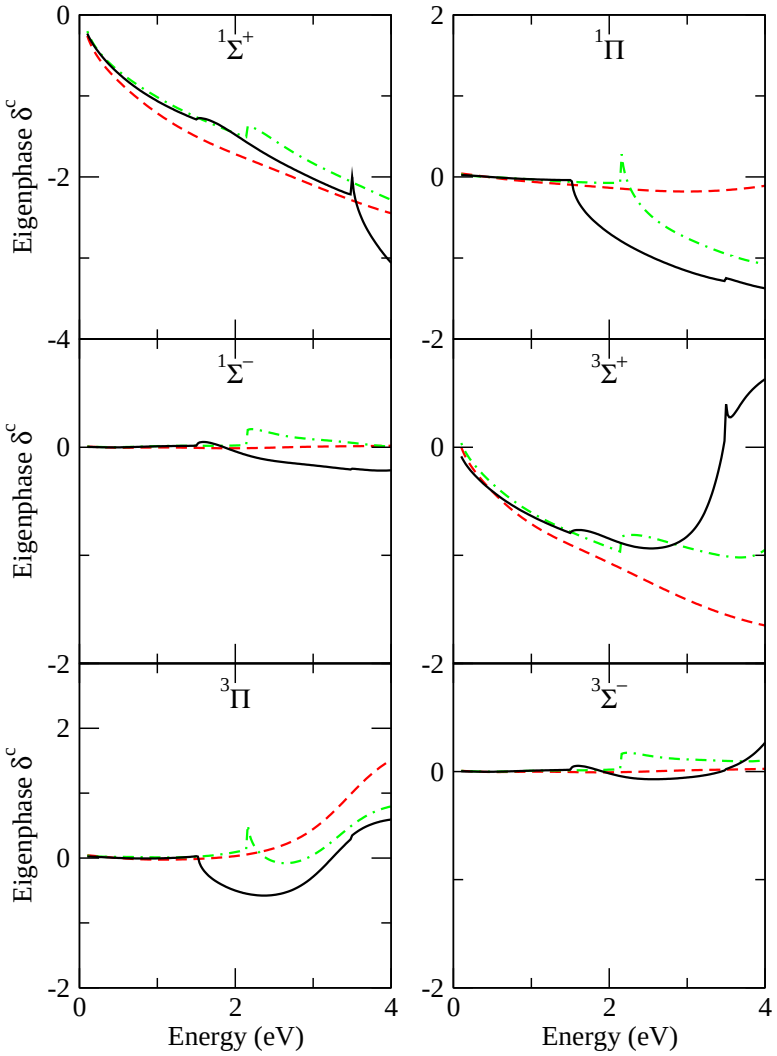

Figure 5.4: Electron – CN eigenphase sums for different symmetries for the SCF-SE(dash), SCF-CC(dash-dot) and NO-CC(solid) models.

1984*b*). Eigenphase sums, which were obtained from diagonalising the K-matrix for each symmetry at each energy, are displayed in figure 5.6. Only low-lying resonances were considered since higher resonances are unlikely to be important in any radiative association process.

A resonance manifests itself as a rapid increase by π radians in the eigenphase sum. This can best be seen in the $^3\Pi$ sum of the figure, where all 3 models undergo this change (although these resonance features extend above the 4 eV range of this figure). Note we do not see the full shift of π as the widths of these resonances are large, spanning between 1 - 1.5 eV. The fitting of the Breit-Wigner form to a resonance can however be disrupted by the presence of threshold features in the eigenphase sum within the energy range of the fit. Threshold features are discontinuities in the derivative of the eigenphase

sum caused by the opening of new scattering channels. This can clearly be seen in both the $^1\Sigma^+$ and $^3\Sigma^+$ eigenphase sums of the NO-CC model, where the B $^2\Sigma^+$ excitation threshold of the target appears at 3.491 eV. The Breit-Wigner form explicitly does not allow for a partial resonance fit, thus when this occurs there is an uncertainty in the fitted data.

Table 5.4 summarizes the resonances detected for CN^-. The SE calculations both detect a single shape resonance of $^3\Pi$ symmetry at about 3.4 eV. At the SE level this is a very broad resonance with a width of about 1.5 eV. In the CC calculations this resonance position is systematically lowered, although for the cc-pVTZ basis set the width narrows and for the aug-cc-pVTZ basis it broadens. This is possibly because RESON had trouble finding this resonance in certain models (where thresholds were present), only a manual increase in the sensitivity of the programme allowed it to be fitted. Hence the widths do not appear consistent across similar models; the quoted values should probably be regarded as uncertain by up to 50%. The CC calculations based on the use of SCF orbitals introduce Feshbach resonances of $^3\Sigma^+$ and $^3\Sigma^-$ symmetry, with the use of an augmented basis set acting to raise the energy at which it appears by about 1 eV and 0.7 eV respectively. We note that none of these resonances lie below the A $^2\Pi$ first excited state of CN.

The quantum chemistry calculations on CN^- by Musial (2005), using the same aug-cc-pVTZ basis set as our final model, calculated excited states of the anion. These excited states would manifest in our scattering calculations as the sum in energies of an anionic bound state and a resonance (of the same symmetry). However the results in Musial (2005) are purely for singlet excited states, for which we find no resonances. This leads us to conclude that the excited states of CN^- detected by Musial (2005) are all false artefacts. The reasoning behind which can be found in the work of Stibbe and Tennyson (1999).

Interestingly we note that both HCN and HNC were found to support a single shape resonance of $^2\Pi$ symmetry at a position of between 2.5 – 3.3 eV and a width of between 1.3 – 1.6 eV depending on the model used (Varambhia. and Tennyson, 2007).

5.5 Results as a Function of Bond Length

As a further development to our calculations we ran the same model (aug-cc-pVTZ basis set, NO-CC scattering model) at different bond lengths, spanning 0.5 Å and centred

Table 5.4: CN^- low lying resonance positions (and widths) in eV

Model	1	2	3	4	5
$^3\Sigma^+$		3.450 (0.761)		4.486 (0.462)	4.526 (1.186)
$^3\Pi$	3.359 (1.513)	2.978 (1.053)	3.424 (1.403)	3.340 (1.583)	3.208 (1.084)
$^3\Sigma^-$		4.613 (1.209)		5.319 (0.906)	4.881 (1.084)

Table 5.5: X $^2\Sigma^+$ target energies, A $^2\Pi$ & B $^2\Sigma^+$ excitation energies, and $^1\Sigma^+$ bound state energies for different bond lengths, All values are in eV.

Bond length (Å)	X $^2\Sigma^+$	A $^2\Pi$	B $^2\Sigma^+$	$^1\Sigma^+$ Binding energy
0.9718	-92.252	3.092	3.212	3.178
1.0718	-92.354	2.206	3.341	3.326
1.1718 (equilibrium)	-92.381	1.515	3.491	3.407
1.2718	-92.371	1.014	3.651	3.414
1.3718	-92.338	0.589	3.622	3.411

on the equilibrium geometry of 1.1718 Å. Table 5.5 presents the results of the target calculation as a function of bond length and also the binding energy of the anionic bound state detected in the scattering calculation.

Table 5.6 gives resonance positions for the $^3\Sigma^+$, $^3\Pi$ and $^3\Sigma^-$ resonances as a function of bond length. As bond length increases we find that all resonances lower in position and narrow in their widths. At the smallest bond length we were unable to fit the width of the $^3\Pi$ resonance. This is due to the extreme broadness the resonance is likely to have, resulting in it crossing over threshold features which RESON is unable to make a fit of. Our calculations also detected a $^3\Delta$ state at 1.2718 and 1.3718 Å, at 1.2718 Å it lies very close to the $^3\Sigma^-$, thus we were unable to obtain a position fit for this resonance despite its clear appearance in the eigenphase sums. The value of 4.1 eV given in Table 5.6 is a result of a manual fit, whereby we have taken the second derivative of

Table 5.6: Resonance position (and widths) in eV as a function of bond length. *a* indicates a manual fit.

Bond length (Å)	0.9718	1.0718	1.1718 (equilibrium)	1.2718	1.3718
$^3\Sigma^+$	7.55 (2.01)	5.71 (1.35)	4.526 (1.186)	2.08 (0.25)	1.03 (0.08)
$^3\Pi$	9.72(*a*)	7.76 (3.14)	3.208 (1.084)	2.64 (0.84)	2.08 (0.52)
$^3\Sigma^-$	9.04 (2.89)	6.64 (1.73)	4.881 (1.084)	4.1*a*	2.40 (0.43)

the eigenphase sum to find the position of the point of inflection. The $^3\Delta$ resonance is observable in the eigenphase sums at all bond lengths, however due to its proximity to $^3\Sigma^-$ and the increased broadness of all resonances at lower bond lengths, we were not able to obtain RESON fits for this $^3\Delta$ resonance.

5.6 Conclusions

This chapter has presented excitation cross-sections to the first two excited states of CN which represent the 'CN red' and 'CN violet' spectral lines. Applying the Born correction to these cross-sections leads to an enhancement of the magnitude of both. It must also be considered that this enhancement is already pronounced at the maximum incident electron energy in our calculations. At 10 eV the size of the cross-section is approximately doubled by the correction. A typical plasma may contain electrons moving at much greater energies than 10 eV, thus if we were to extend our results up to and beyond ionisation of the molecule (into the high energy scattering regime), this enhancement will be even more pronounced. This is because at these energies the Born approximation becomes dominant. This increase in cross-section magnitude will lead to an increase in calculated excitation rates, likely leading to an enhancement of the spectra modelled from this data.

Thus far the role of electron-scattering cross-sections in the interstellar medium (ISM) has largely been ignored. Due to this there is no data with which to compare our excitation cross-sections to, and to our knowledge we believe our data to be the first low-energy electronic excitation cross-sections for this molecule. Comparisons with plasma models are also difficult, as these all assume non-local thermal equilibrium (LTE). Because of this the plasma spectra can be predicted from these models, however reaction rates cannot. Thus no direct comparisons with existing plasma data can be made.

The calculations also give data which suggest there are no scattering resonance features at low energy, below 3 eV. This makes it unlikely that the formation on CN^- in the ISM is caused by the trapping of an incoming electron into a resonance state of neutral molecule. The temperatures in the ISM are simply too low to produce electrons with enough energy to become trapped in one of these states.

As discussed in chapters 6 & 7, an alternative explanation of the observed molecular anion abundance may arise from the very weakly bound anionic states. These states will support nuclear excited states which lie in the continuum and therefore are resonances.

However, it appears that CN^- does not support any of these states either. It would therefore seem likely that the vast majority interstellar CN^- is formed by some other mechanism, such as by dissociative attachment of a CN containing species.

5.7 CN Spin-Coupled Rotational Cross-Sections

The theory used in this section is fully outlined in chapter 4 and these results have been published in Harrison et al. (2012).

5.7.1 Introduction

CN was one of the earliest molecules detected in the ISM and it has been observed in a variety of different astronomical environments (Bus et al., 1991; Ahearn et al., 1995; Fray et al., 2005; Giannetti et al., 2012). The CN rotational spectrum has been used to measure the temperature of the cosmic microwave background (CMB) along different lines of sight. However whether the collisional excitation by species including electrons contribute to an enhanced observed temperature for the rotational states of CN has proved controversial (Roth et al., 1993; Leach, 2012). Electron collisional excitation of CN was considered sometime ago by Crawford et al. (1969) and Allison and Dalgarno (1971), and recently by Harrison and Tennyson (2012).

Each rotational level of CN is split by spin-rotation coupling so that rotational level N has two sub-levels given by $j = N \pm 1/2$; conventionally each of these are labelled using N and the e or f label for the splitting (Brown et al., 1975). Levels with parity $+(-1)^{j-1/2}$ are e levels ($j = N + 1/2$), while levels with parity $-(-1)^{j-1/2}$ are f levels ($j = N - 1/2$). Radiative (dipolar) selection rules are:

$$\Delta j = 0, e \leftrightarrow f, \Delta j = \pm 1, e \leftrightarrow e, \text{and} f \leftrightarrow f, \tag{5.1}$$

5.7.2 Results

Figures 5.7 to 5.11 present both the pure rotational ("rotational") and spin-rotational cross-sections for the $0 \rightarrow N$ ($N = 0, 1, 2, 3, 4$), $1 \rightarrow 1$, $2 \rightarrow 2$, $1 \rightarrow 2$ and $1 \rightarrow 3$ transitions, for incident electron energies up to 4 eV. The e/f notation in the legends indicating the spin-resolved transition between states as discussed in the previous paragraph. It is important to note that above the A $^2\Pi$ excitation threshold at 1.515 eV, electronic excitations are also possible. However, what is clearly visible in the figures is

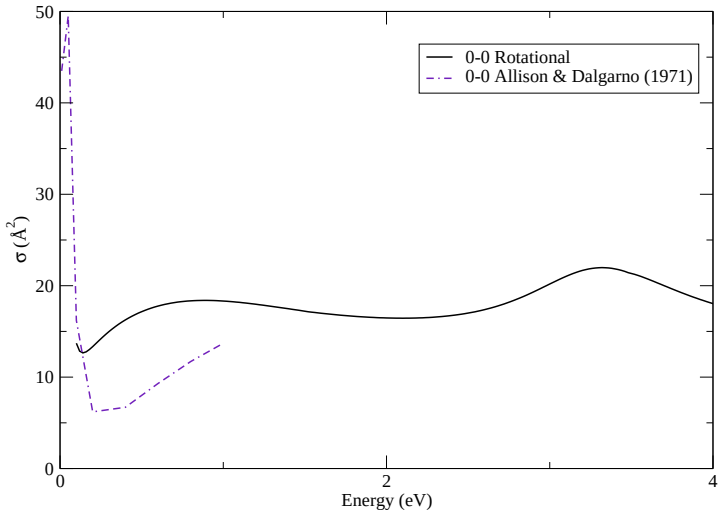

Figure 5.5: CN $N = 0 - 0$ elastic rotationally-resolved cross-section

the resonance feature associated with the ^2Pi resonance between 3-3.4 eV (depending on model). The resonance region is the energy range where transitions with $\Delta N > 2$ are significant but, conversely, it does not significantly affect the dipole-dominated $\Delta N = 1$ transitions. Also note the 0-0 elastic rotational cross-section is not changed by introducing spin-coupling, as both j and j' may only have the value 1/2. Cross-sections up to and included $\Delta N = 6$ were calculated and considered, however those beyond $\Delta N = 4$ are all very small, below 0.01 Å^2 and are not considered here.

In fig. 5.7, the present pure elastic $0 - 0$ cross section is compared to the old close-coupling calculations of Allison and Dalgarno (1971). Both calculations are found to agree at the lowest energy (0.1 eV) while at higher energy, our value is much larger, reflecting most probably the much better treatment of the short-range forces as well as the possible role of the above mentioned resonances.

Very similar elastic cross sections are obtained for levels $N = 1$ and 2, as plotted in fig. 5.8. We also observe for these "quasi-elastic" transitions ($\Delta N = 0$) that parity-changing transitions ($e \leftrightarrow f$) have much lower cross sections than parity-conserving transitions. This propensity rule is further discussed below.

In fig. 5.9, the $0 - 1$ and $0 - 2$ rotational cross sections are compared to the results of Allison and Dalgarno (1971). The large dipolar $0 - 1$ cross sections are found in excellent agreement, as expected since the dipole moment used is the same in both calculations. The present $0 - 2$ cross section is found to be significantly lower than that of Allison and Dalgarno (1971), as this transitions is dominated by short-range effects,

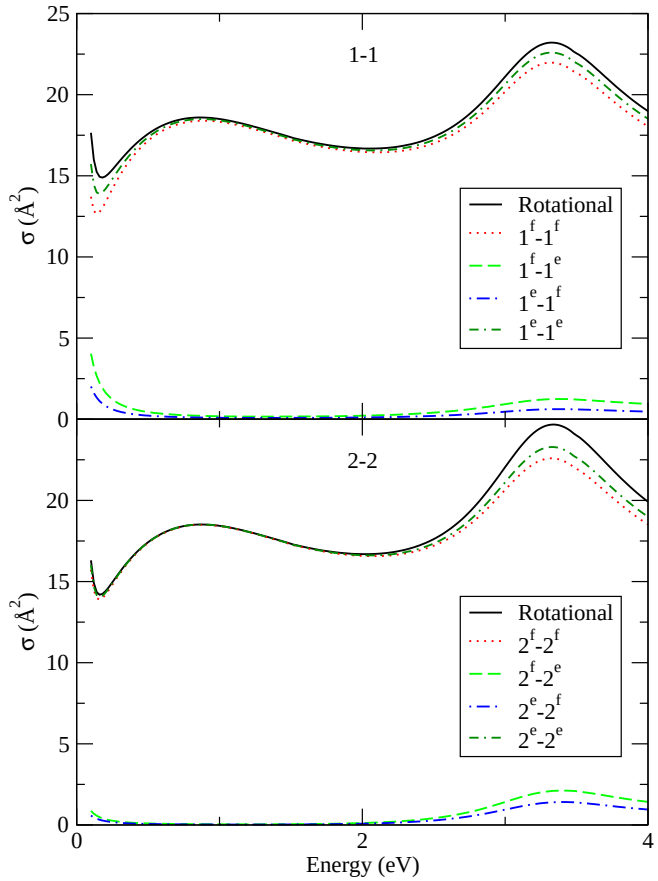

Figure 5.6: CN $N = 1 - 1$ and $N = 2 - 2$ spin-rotationally resolved elastic cross-sections

this again shows the importance of the R-matrix treatment. It is also about two orders of magnitude lower than the $0 - 1$ cross section. We also observe that the largest spin-rotational cross sections are those corresponding to parity-conserving transitions. This propensity rule, which can be written $\Delta j = \Delta N$, is a general feature of any molecule in $^{2S+1}\Sigma$ electronic state as described theoretically in Alexander et al. (1986). For $\Delta j = 1$ it thus follows the above radiative selection rule. At the IOS level, it can be explained simply from the $3j$ and $6j$ coefficients in eq. (4.14). We note that this propensity rule is also observed in the recent close-coupling calculations of Lique and Klos (2011) and Kalugina et al. (2012) on CN–He and CN–H_2, respectively.

Fig. 5.10 shows that $0 - 3$ and $0 - 4$ cross sections are much lower than the $0 - 2$ cross section, except in the region of the B $^2\Sigma^+$ resonance where the $0 - 4$ cross section, in particular, is significantly amplified and becomes larger than the $0 - 2$ cross section. This is expected to have important consequences on the spin-coupled cross sections, as discussed below. Again we observe that parity-conserving transitions ($\Delta j = \Delta N$) are

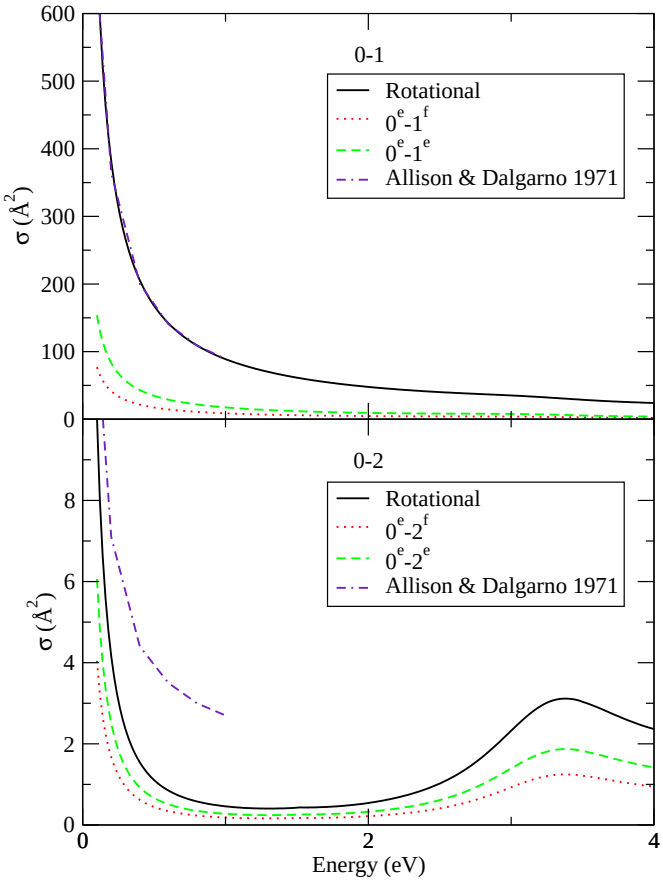

Figure 5.7: CN $N = 0 - 1$ and $N = 0 - 2$ spin-rotational excitation cross-sections

preferred.

Finally, fig. 5.11 gives cross sections for $\Delta N = 1, 2$ transitions out of the $N = 1$ parity doublet. The dipolar $1 - 2$ rotational cross section is found to be comparable to the $0 - 1$ cross section and the propensity rule $e \leftrightarrow e, f \leftrightarrow f$ is clearly in evidence for all transitions at collision energy below about 2 eV. However, at higher energy, the parity-changing transition $1^f - 3^e$ is surprisingly found to become dominant. This illustrates the strong impact of the resonance associated with the B $^2\Sigma^+$ excitation at 3.49 eV. Indeed, this resonance greatly enhances the $0 - 3$ and $0 - 4$ cross sections (see fig. 5.10) which, in turn, increase $\Delta j = 3$ cross sections through eq. (4.14).

5.7.3 Conclusions

Data has been presented for the $(0 \rightarrow N)$, $(N = 0 - 4)$, $1 \rightarrow 2$ & $1 \rightarrow 3$ rotational cross-sections for an electron-CN collision. These results are heavily influenced by both the A $^2\Pi$ and B $^2\Sigma^+$ excitation thresholds at 1.52 and 3.49 eV respectively. The latter

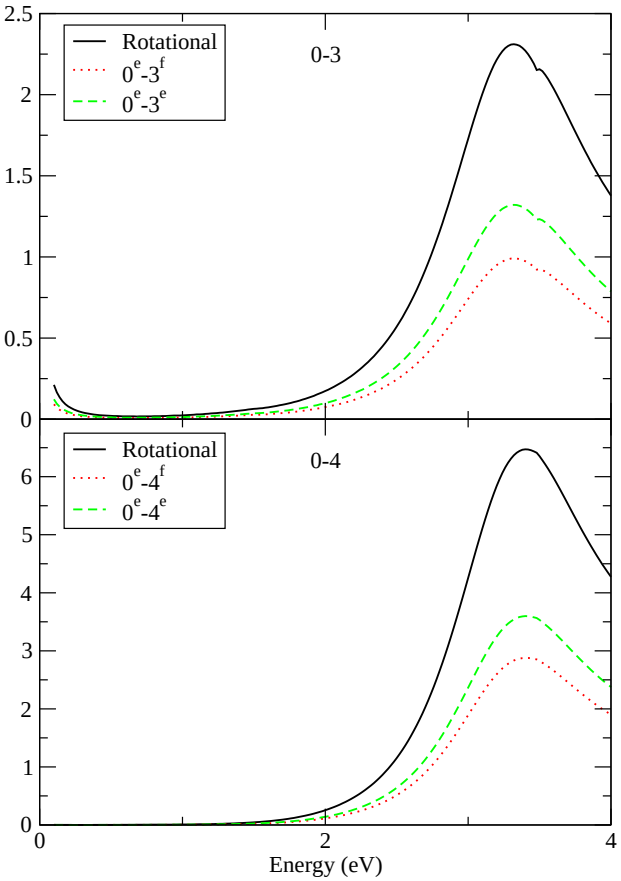

Figure 5.8: CN $N = 0 - 3$ and $N = 0 - 4$ spin-rotational excitation cross-sections

in particular leading to an enhancement of the cross-sections. At energy below these electronic thresholds, the usual propensity rule for parity-conserving transitions ($\Delta j = \Delta N$) was found to hold.

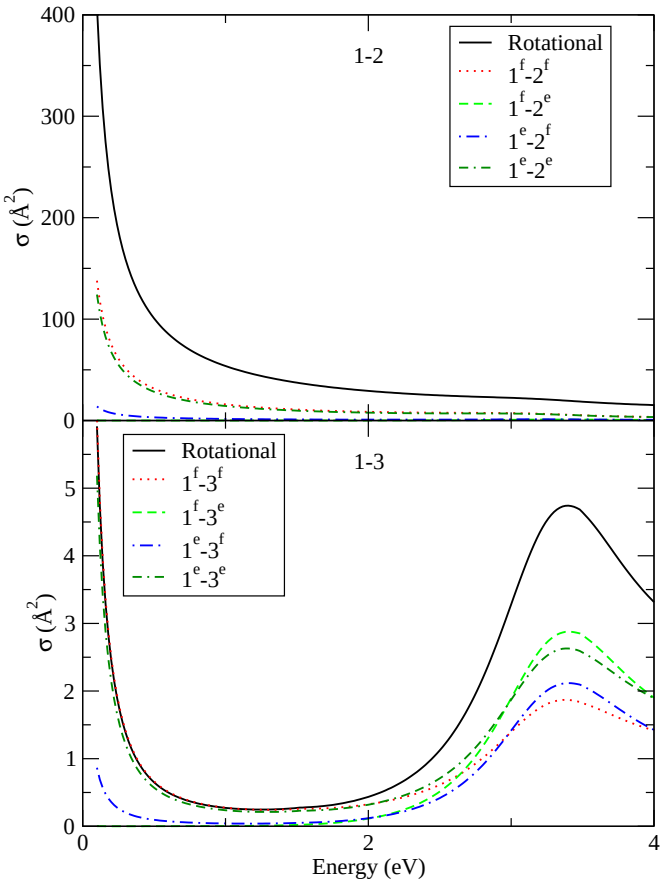

Figure 5.9: CN $N = 1 - 2$ and $N = 1 - 3$ Spin-Rotational Cross-sections

Chapter 6

C_3N

This chapter has been substantially published as Harrison and Tennyson (2011).

6.1 Introduction

The molecule C_3N (fig 6.1) has recently been discovered in the ISM (Thaddeus et al., 2008) alongside other members in the C_nN series (Cernicharo et al., 2008; Agundez et al., 2010). It has also been detected in the atmosphere of Titan (Vuitton et al., 2009).

No experimental data has ever been produced on the molecule, and whilst this is the first investigation into electron-scattering interactions with C_3N, many target calculations have already been published (McCarthy et al., 1995; Sadlej and Roos, 1991; Flores, 1992), along with work on the ground state of the C_3N^- anion (Botschwina and Oswald, 2008; Kolos et al., 2008; Zhan and Iwata, 1996).

6.2 Method

The scattering calculations reported here were performed using the UK molecular R-matrix codes (Morgan et al., 1998*b*), mostly starting from the Quantemol-N interface (section 3.6). Target electronic structure calculations were largely performed with MOLPRO (Werner et al., 2008), which was also used to provide many of the sets of target molecular orbitals. The scattering calculations were performed at two levels: static exchange (SE), which is useful for identifying shape resonances, and close coupling (CC). The presence of very low-lying excited target states meant that the widely used static exchange plus polarisation model was deemed inappropriate for this study, as this method

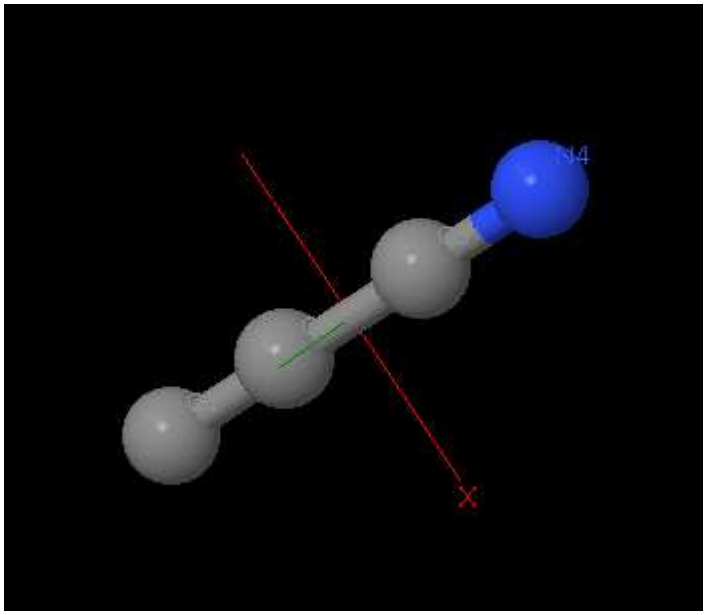

Figure 6.1: The molecule C_3N (taken from Quantemol-N)

Table 6.1: Equilibrium bond lengths for C_3N

Bond	Length (Å)
C1-C2	1.212
C2-C3	1.375
C3-N	1.161

is prone to giving pseudoresonances at energies above the first electronically excited target state.

As we are dealing with electron collisions with strongly dipolar systems, it is necessary to allow for the contribution of electron interactions with the long-range target dipole moment to any cross sections calculated. This was carried out using the program BORNCROS (Baluja et al., 2000), which directly calculates the dipole Born correction to the cross-sections.

All calculations were performed at the equilibrium geometry of the neutral target (table 6.1) and ignored effects due to nuclear motion. We note that although the molecule considered here is linear, neither the polyatomic R-matrix codes nor MOLPRO use $C_{\infty v}$ symmetry. All calculations were therefore performed using C_{2v} symmetry. In most cases identifying the results in $C_{\infty v}$ is straightforward and these symmetry labels are largely used below.

Table 6.2: Results of the cc-pVTZ R-matrix target tests run using various weighted NOs produced by Molpro, and their comparison to the pure Molpro calculation and other theoretical data.

Weighting ($^2\Sigma^+$:$^2\Pi$:$^2\Sigma^-$)	X $^2\Sigma^+$ (H)	μ (D)	A $^2\Pi$ (eV)
1:0:0	-168.009	2.93	1.20
5:2:1	-168.003	3.66	0.41
1:1:1	-167.999	3.89	0.30
Pure Molpro	-168.516	2.86	0.16
McCarthy et al. (1995)	-167.400	2.85	0.27

6.3 Target Calculations

Quantemol-N was used to carry out HF and CAS-CI calculations using DZP and cc-pVDZ basis sets. Tests were performed with several other basis sets, including the ANO basis recommended by Widmark et al. (1990) for the C_3N but for which we were unable to get satisfactory results.

Models 2 and 4, used a 10σ, 3π orbital space, with 8 electrons frozen in the 1 – 4σ orbitals and the remaining 17 electron distributed among the 5 – 10σ and all the π orbitals. This CAS-CI model was retained for use in model 5, which made use of MOLPRO MRCI orbitals; these NOs were obtained by the state-averaging the lowest $^2A_1$, $^2B_1$, $^2B_2$, and $^2A_2$ MRCI states in a 5:2:2:1 weighting, manually chosen in order to produce good target characteristics for the scattering run. Table 6.2 shows the full details of Molpro NO study.

Table 6.3 compares our target models with the results of previous electronic structure calculations. Despite a thorough search no experimental dipole moments could be found for the neutral molecule.

6.4 Scattering Calculations and Bound Anion States

Again a 48-state calculation was carried out (doublet and quartet states with 6 states per symmetry being included). The 40 target states below 10eV retained in the outer region. 46 in Quantemol-N jobs. As for C_2H^- (chapter 7) the bound state calculations retained only the X $^2\Sigma^+$ and A $^2\Pi$ target states, and were propagated to 30.1 a_0.

Table 6.4 presents the calculated electronic bound states for all models, as well as previous results from literature. All models find the deeply bound X $^1\Sigma^+$ state, with CC calculations finding the state between 1 and 1.5 eV deeper, furthermore use of the

Table 6.3: Selected calculated target properties of C_3N. All results are for the equilibrium geometry of C_3N. The calculated absolute energies of the X $^2\Sigma^+$ ground state is given in Hartree while the vertical excitation energy to the low-lying A $^2\Pi$ is given in eV. μ is the ground state dipole moment, given in Debye. See text for details of models.

Model	Basis	Orbitals	Method	X $^2\Sigma^+$	μ	A $^2\Pi$
This work/1	DZP	SCF	HF	-167.870	2.332	
2	DZP	SCF	CAS-CI	-167.933	1.288	1.038
3	cc-pVDZ	SCF	HF	-167.871	2.749	
4	cc-pVDZ	SCF	CAS-CI	-167.937	2.270	1.235
5	cc-pVTZ	NOs	CAS-CI	-168.003	3.655	0.406
Flores (1992)	6-31G*		UMP2	-168.345	3.270	
Sadlej and Roos (1991)	ANO	CAS-SCF	CAS-SCF		2.920	0.750
		CAS-SCF	MRCI		3.040	0.400
McCarthy et al. (1995)	cc-pVTZ		RCCSD(T)	-167.440		0.266
	cc-pVQZ		RHF	-168.071	3.254	
			RCCSD	-167.439	2.887	
			RCCSD(T)	-167.400	2.852	0.270

MRCI-CC calculation bring the bound state even deeper to about 4 eV, closer in line with data from previous results in the literature. This model also finds numerous other weakly bound states of C_3N^-, presented in table 6.5. It should be noted that model 3 (SCF-SE calculation using the cc-pVDZ basis set) also finds the $^{1,3}\Pi$ bound state at 0.0002 eV, although this was not found in any other models that use SCF orbitals. There appears to be no prediction of bound states other than the X $^1\Sigma^+$ states in the literature.

6.5 Resonances

Figure 6.2 presents the eigenphase sums for C_3N^- calculations. Table 6.6 summarizes the resonance data for C_3N^- calculations, with the same method being employed as previously described for the C_2H^- resonances. The SE models all find shape resonances of $^1\Pi$ and $^3\Pi$ symmetries. These appear in all CC calculations at about 0.1 eV lower in electron scattering energy, with the width remaining quite stable for the $^1\Pi$ resonance, and at about 0.2 – 0.4 eV lower scattering energy with a narrower width for the $^3\Pi$

Table 6.4: C_3N^- bound states with binding energies given in eV relative to the ground state. All results are for the equilibrium geometry of C_3N

Model	Basis	Orbitals	Method	X $^1\Sigma^+$
This work/1	DZP	SCF	SE	2.793
2	DZP	SCF	CC	3.896
3	cc-pVDZ	SCF	SE	2.248
4	cc-pVDZ	SCF	CC	3.788
5	cc-pVTZ	MRCI	CC	4.009
Botschwina and Oswald (2008)	VQZ+	RHF	RHF	3.651
	VQZ+	RHF	RCCSD	4.343
	VQZ+	RHF	RCCSD(T)	4.395
Kolos et al. (2008)	aug-cc-pCV5Z	RHF	RHF	3.650
	aug-cc-pCV5Z	RHF	RCCSD	4.363
	aug-cc-pCV5Z	RHF	RCCSD(T)	4.417
Zhan and Iwata (1996)	6-31G+(d)	HF	HF	2.519

Table 6.5: Binding energies, in eV, of the states of C_3N^- calculated for the MRCI-CC scheme (model 5).

	Singlet	Triplet
Σ^+		0.0012
	0.5490	0.5490
		0.6241
		0.6220
	4.0094	4.0094
Π	0.0003	0.0003

Table 6.6: C_3N^- low-lying resonance positions (and widths) in eV

Model	1	2	3	4	5
$^1\Pi$	2.905 (0.471)	2.716 (0.452)	2.989 (0.444)	2.822 (0.475)	2.749 (0.437)
$^1\Sigma^-$		2.29 a		2.191 (0.158)	2.094 (0.153)
$^1\Delta$		2.307 (0.161)		2.248 (0.176)	2.167 (0.184)
$^3\Sigma^+$		0.987 (0.016)		1.327 (0.023)	0.741 (0.034)
$^3\Pi$	1.342 (0.204)	1.167 (0.121)	1.632 (0.220)	1.25 a	1.426 (0.141)
$^3\Sigma^-$		1.795 (0.053)		2.163 (0.063)	1.666 (0.075)
$^3\Delta$		1.460 (0.038)		1.819 (0.047)	1.329 (0.060)

[a] Resonance present in eigenphases but not fitted by RESON.

resonance. In all CC calculations, Feshbach resonances appear in $^1\Sigma^-$, $^1\Delta$, $^3\Sigma^+$, $^3\Sigma^-$ and $^3\Delta$ symmetries. These resonances appear systematically at higher energies for the larger cc-pVTZ basis compared to cc-pVDZ when using SCF orbitals. However the use of MRCI NO's leads to lower resonance positions than either SCF-CC models for all symmetries. The Feshbach resonance widths remain stable across all CC models.

6.6 Cross-Sections

Figure 6.3 presents the total elastic cross-section of C_3N for electron scattering energies up to 10 eV, for three models, SCF-SE, SCF-CC and MRCI-CC. Born corrected results for the MRCI-CC model are also shown.

Figures 6.4 shows inelastic cross-sections representing the excitation from the $^2\Sigma^+$ ground state of the neutral to the first two excited states, both of which are $^2\Pi$; the Born correction is applied to both excitations. The comparison between the SCF-CC and the MRCI-CC models shows us that the use of MRCI orbitals increases the cross-sections at all energies, although both models share similar features (such as the threshold spike in B $^2\Pi$ excitation). Again the extra resonances shown by the MRCI-CC model should be treated with caution.

6.7 Conclusions

The presence of electronic resonance features above 1 eV for this molecule suggests that formation of temporary negative ions by electrons trapped in these resonance states is an unlikely mechanism for radiative electron attachment in the ISM. This is because 1 eV

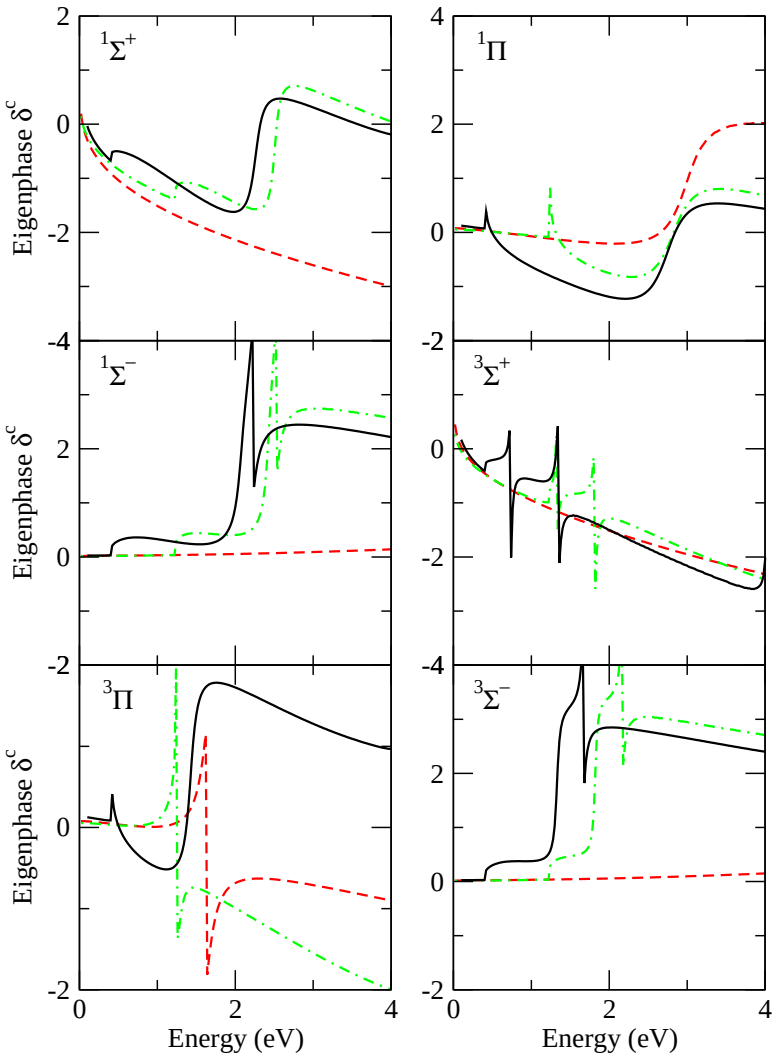

Figure 6.2: Electron – C_3N eigenphase sums: for SCF-SE(dash), SCF-CC(dash-dot) and MRCI-CC(solid) models.

converts to a much higher temperature than electrons are found at in the ISM, making it highly unlikely electrons will reach the energies required to become temporarily trapped in the resonance states.

The more likely possibility is that the molecular anions observed may arise from the very weakly bound anionic states, as found for C_3N^-. These states will support nuclear excited states which lie in the continuum and therefore are resonances. If this mechanism does explain the formation of such anions, C_3N^- would be observed in large quantities but C_2H^- would not as this molecule does not support such states (see chapter 7). This prediction appears to match current observations.

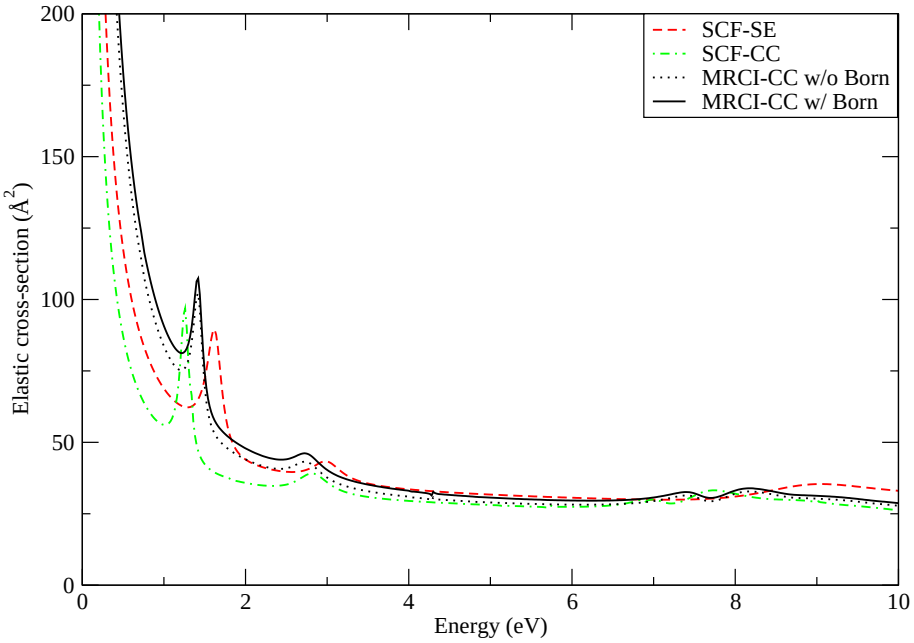

Figure 6.3: C_3N Elastic Cross-Section

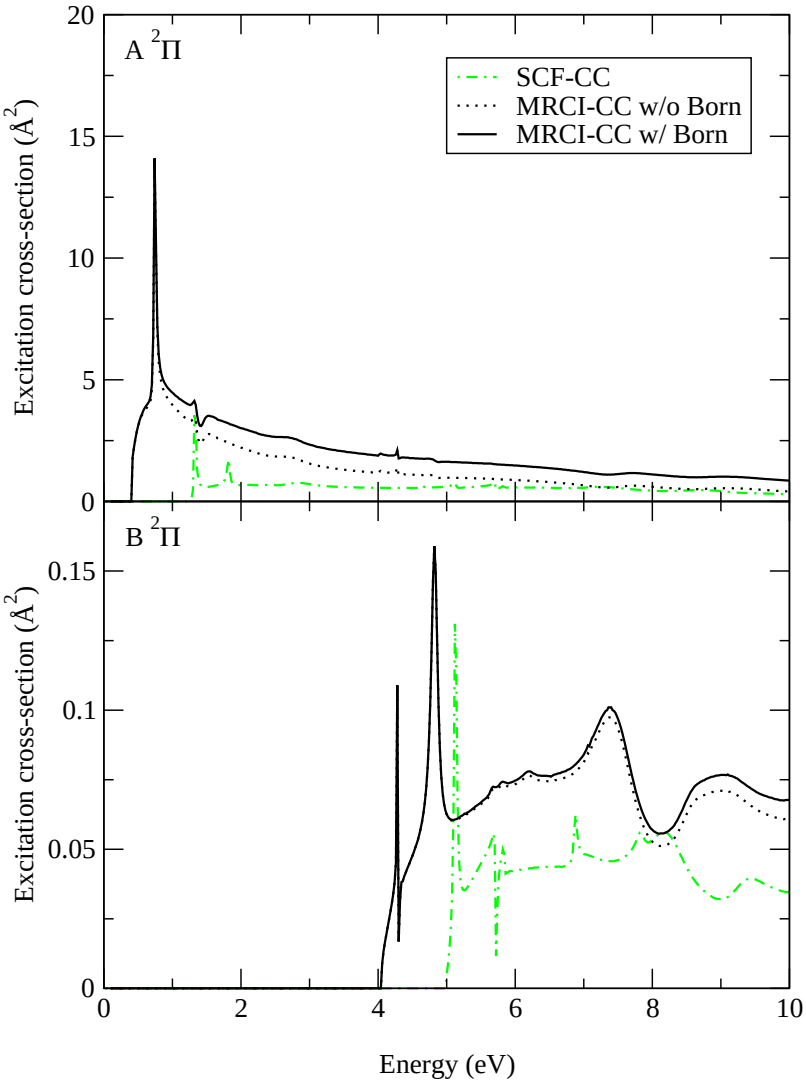

Figure 6.4: C_3N electron impact electronic excitation cross sections to A $^2\Pi$ and B $^2\Pi$.

Chapter 7

C_2H

This chapter has been substantially published as Harrison and Tennyson (2011).

7.1 Introduction

Whilst C_2H (figure 7.1) has not been directly observed in the ISM, a number of its larger counterparts have been (Gupta et al., 2007; McCarthy et al., 2006; Brunken et al., 2007; Vuitton et al., 2009). Initially our studies focussed on electron collisions with C_4H as the first member of the series for which the associated anion had been observed in the interstellar medium (Gupta et al., 2007). However we found it difficult to establish definitive properties for the ground state of C_4H, a problem that is well-documented (Fortenberry et al., 2010). Although we have performed a series of electron collision studies with C_4H, here we report electron collision calculations which focus on C_2H as we consider the results of these calculations to be more reliable.

Although no experimental work has ever been carried out on the neutral radical, a number of previous theoretical calculations (Woon, 1995; Cui and Morokuma, 1998), including DFT (Ziegler and Gutsev, 1992) have been published. There is also been some experimental data on the binding energy of the electron in C_2H^- (Janousek et al., 1979; Ervin and Lineberger, 1991; Taylor and Xu, 1998).

7.2 Method

The scattering calculations reported here were performed using the UK molecular R-matrix codes (Morgan et al., 1998*b*), mostly starting from the Quantemol-N interface (section 3.6). Target electronic structure calculations were largely performed with MOL-

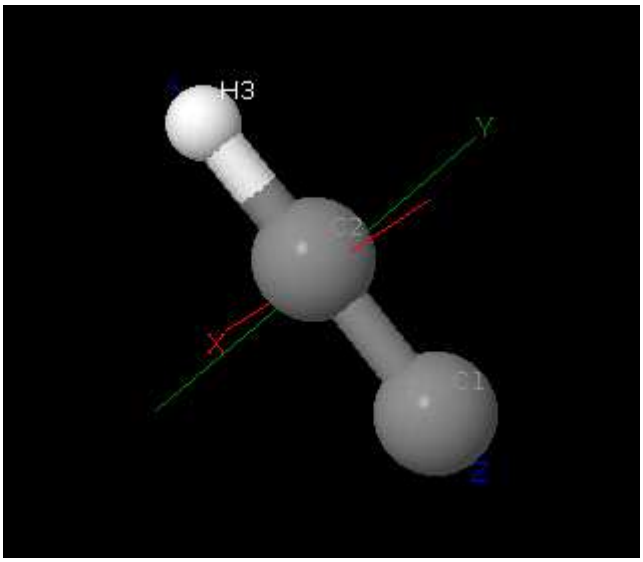

Figure 7.1: The molecule C_2H (taken from Quantemol-N)

PRO (Werner et al., 2008), which was also used to provide many of the sets of target molecular orbitals. The scattering calculations were performed at two levels: static exchange (SE), which is useful for identifying shape resonances, and close coupling (CC). The presence of very low-lying excited target states meant that the widely used static exchange plus polarisation model was deemed inappropriate for this study, as this method is prone to giving pseudoresonances at energies above the first electronically excited target state.

As we are dealing with electron collision with strongly dipolar systems, it is necessary to allow for the contribution of electron interactions with the long-range target dipole moment to any cross sections calculated. This was carried out using the program BORNCROS (Baluja et al., 2000), which directly calculates the dipole Born correction to the cross-sections.

All calculations were performed at the equilibrium geometry of the neutral target (table 7.1) and ignored effects due to nuclear motion. We note that although the molecule considered here are linear, neither the polyatomic R-matrix codes nor MOLPRO use $C_{\infty v}$ symmetry. All calculations were therefore performed using C_{2v} symmetry. In most cases identifying the results in $C_{\infty v}$ is straightforward and these symmetry labels are largely used below.

Table 7.1: Equilibrium bond lengths for C_2H

Bond	Length (Å)
C1-C2	1.235
C2-H	1.080

7.3 Target Calculations

A variety of models were tested when calculating results for the neutral C_2H target, a selection of these are shown in table 7.3. Models 1 – 6 were carried out using the R-Matrix software Quantemol-N. These comprised Hartree-Fock (HF) and Complete Active Space Configuration-Interaction (CAS-CI) calculations using each of the 3 basis sets, DZP, cc-pVDZ and cc-pVTZ. The CAS-CI calculations used an orbital space of 7,2,2 orbitals of symmetry a_1, b_1, b_2 respectively which maps to 7 σ and 2 π orbitals. Eight electrons were frozen in the 1 – 4σ orbitals with five active electrons distributed amongst the 5 – 7σ and 1 – 2π. Model 7 used this CAS-CI model but the molecular orbitals used in the calculation were produced by MOLPRO, in this case using a multireference CI (MRCI) calculation, and the R-Matrix calculation was carried out using the R-Matrix codes manually, to allow for use of MOLPRO orbitals. These natural orbitals (NOs) were state averaged from 3 states produced one each from $^2A_1$, $^2B_1$ and $^2B_2$, ($^2\Sigma^+$ and $^2\Pi$) MRCI calculations, using the MOLPRO 'MATROP' facility, with a 13:1:1 weighting. This weighting was chosen to create a target model with good characteristics for the scattering calculation i.e. a good reproduction of the excitation energies and dipole moment in comparison with the original MOLPRO calculations. Use of the pure $^2A_1$ MRCI orbitals was found to make the first vertical excitation energy too high in energy by a factor of 2, and the use of more equally weighted state-averaged orbitals was found to reduce the dipole to a value too small to be acceptable in the scattering calculation by up to a factor of 3. Hence model 7 was deemed acceptable in describing both these characteristics without sacrificing one in favour of the other. Whilst we were able to find some experimental data for the bound state energy of the anion, we could not find any data on the neutral, such as the dipole moment. Table 7.2 shows the full details of Molpro NO study.

There have been a number of previous *ab initio* studies on C_2H; Table 7.3 compares our models with the best of these. As we only use a very limited correlation space, the other studies give lower absolute energies even for calculations which use the same

Table 7.2: Results of the cc-pVTZ R-matrix target tests run using various weighted NOs produced by Molpro, and their comparison to the standalone Molpro quantum chemistry calculation and other theoretical data.

Weighting ($^2\Sigma^+$:$^2\Pi$:$^2\Sigma^-$)	X $^2\Sigma^+$ (H)	μ (D)	A $^2\Pi$ (eV)
16:1:0	-76.297	0.68	1.12
13:1:0	-76.296	0.64	1.09
8:1:1	-76.296	0.57	1.03
5:2:0	-76.293	0.28	0.87
1:1:1	-76.267	0.09	0.82
Molpro	-76.484	0.82	0.55
Woon (1995)	-76.468	0.77	0.40

Table 7.3: Selected calculated target properties of C_2H. All results are for the equilibrium geometry of C_2H. The calculated absolute energies of the X $^2\Sigma^+$ ground state is given in Hartree while the vertical excitation energy to the low-lying A $^2\Pi$ is given in eV. μ is the ground state dipole moment, given in Debye. See text for details of models.

Model	Basis	Orbitals	Method	X $^2\Sigma^+$	μ	A $^2\Pi$
This work/1	DZP	SCF	HF	-76.142	0.804	1.186
2	DZP	SCF	CAS-CI	-76.200	0.837	1.204
3	cc-pVDZ	SCF	HF	-76.138	0.789	
4	cc-pVDZ	SCF	CAS-CI	-76.207	0.801	1.304
5	cc-pVTZ	SCF	HF	-76.156	0.797	
6	cc-pVTZ	SCF	CAS-CI	-76.208	0.801	1.248
7	cc-pVTZ	NOs	CAS-CI	-76.296	0.640	1.089
Woon (1995)	cc-pVDZ		RCCSD(T)	-76.401	0.766	0.361
	cc-pVTZ		RCCSD(T)	-76.468	0.774	0.402
	CBS limit		RCCSD(T)	-76.499		0.423
Cui and Morokuma (1998)	cc-pVTZ		CASPT2	-76.458		0.790

target basis. Our dipole moments are in reasonable agreement with those predicted by Woon (1995). However our predictions for the vertical energy of excitation for the very low-lying A $^2\Pi$ state appear to be systematically too high.

7.4 Scattering Calculations and Bound Anion States

Our scattering calculations concentrated on finding bound states and resonances for C_2H^- but also provide low-energy electron – C_2H collision cross sections. Two classes

Table 7.4: C_2H^- bound states with binding energies given in eV relative to the ground state. All calculations are for the equilibrium geometry of C_2H

Model	Basis	Orbitals	Method	$^1\Sigma^+$ Binding energy (eV)
This work/1	DZP	SCF	SE	1.186
2	DZP	SCF	CC	2.713
3	cc-pVDZ	SCF	SE	1.114
4	cc-pVDZ	SCF	CC	2.637
5	cc-pVTZ	SCF	SE	1.156
6	cc-pVTZ	SCF	CC	2.617
7	cc-pVTZ	NOs	CC	2.282
Baker et al. (1986)	6-311^{++}G	UHF	UHF	1.56
	6-311^{++}G	UHF	UCISD	2.62
Janousek et al. (1979)			experiment	2.94±0.10
Ervin and Lineberger (1991)			experiment	2.969±0.006
Taylor and Xu (1998)			experiment	2.956±0.020

of models were tested: SE based on a single target state and CC models where 48 state calculations (doublet and quartet states, 6 states per symmetry) were performed in the inner region. As discussed below, different numbers of these states were retained in the outer region of the calculation.

Bound states were calculated using the outer region program BOUND (Sarpal et al., 1991). For these calculations only the low-lying X $^2\Sigma^+$ and A $^2\Pi$ were retained in the outer region of the CC calculations. These were propagated to a distance of 30.1 a_0. Table 7.4 summarizes the results of these studies. In contrast to C_3N^- discussed in chapter 6, all models found only a single bound state. The SE calculations give a vertical binding energy of about 1.2 eV whereas for the CC calculations this binding energy is increased to about 2.6 eV. These figures are in broad agreement with the electronic structure calculations of Baker et al. (1986). The CC binding energies are some 0.6 eV less than the measured ones; however the measured binding energies are adiabatic and will therefore be higher than our calculated vertical ones.

Table 7.5: C_2H^- low lying resonance positions (and widths) in eV

Model	1	2	3	4	5	6	7
$^1\Sigma^+$							2.957 (0.122)
$^1\Sigma^-$		3.876 (1.115)		4.231 (1.056)		3.908 (1.080)	5.130 (1.596)
$^3\Sigma^+$		2.589 (0.430)		2.768 (0.377)		2.679 (0.444)	2.923 (0.127)
							3.942 (0.125)
$^3\Pi$	3.522 (1.949)	3.49 a	3.634 (2.038)	3.380 (1.360)	3.562 (2.021)	3.53 a	3.682 (2.742)
$^3\Sigma^-$		3.374 (0.867)		3.625 (0.814)		3.416 (0.854)	4.495 (1.298)

[a] Resonance present in eigenphases but not fitted by RESON.

7.5 Resonances

Outer region calculations were performed retaining those target states which lie below 10 eV for the CC calculations, the Quantemol-N default setting. This means 25 states for models 2, 4 and 6 but only 16 for model 7. The results reported below are insensitive to increasing these numbers. Resonances were characterised using a Breit-Wigner fit to the eigenphases, which are shown in figure 7.2, as implemented in the automated detection and fitting program RESON (Tennyson and Noble, 1984*b*). As noted below, resonances which overlap excitation thresholds were not fitted by this procedure. Only low-lying resonances were considered since higher resonances are unlikely to be important in any radiative association process.

Table 7.5 summarizes the resonances detected for C_2H^-. The SE calculations all detect a single shape resonance of $^3\Pi$ symmetry at about 3.5 eV. At the SE level this is a very broad resonance with a width of about 2 eV. In the CC calculations this resonance position is lowered to about 3.4 eV and becomes considerably narrower with SCF orbitals and broader with MRCI NO's. The CC calculations based on the use of SCF orbitals introduce Feshbach resonances of $^1\Sigma^-$, $^3\Sigma^+$ and $^3\Sigma^-$ symmetry. Use of NOs introduce a further narrow $^3\Sigma^+$ resonance. We note that none of these resonances lie below the A $^2\Pi$ first excited state of C_2H.

7.6 Cross-Sections

Figure 7.3 presents the total elastic cross-section of C_2H for electron scattering energies up to 10 eV, for all 3 models, SCF-SE, SCF-CC and MRCI-CC. For the final MRCI-CC model, a Born correction was applied due to the dipolar nature of the molecule, which acts to increase the cross-section at all energies.

Electron impact electronic excitation cross sections are a feature of CC calculations.

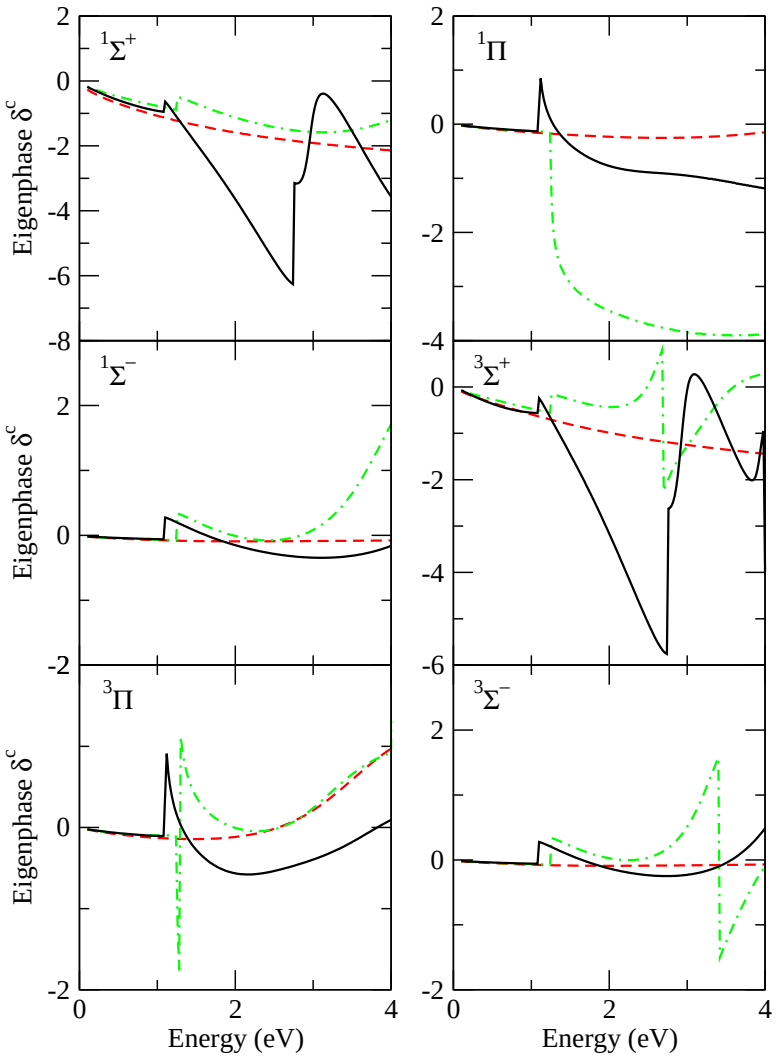

Figure 7.2: Electron – C_2H eigenphase sums for different symmetries for the SCF-SE(dash), SCF-CC(dash-dot) and MRCI-CC(solid) models.

Figure 7.4 shows the cross-sections representing the excitation from the $^2\Sigma^+$ ground state of the neutral to the first three excited states, A $^2\Pi$, a $^4\Sigma^+$ and b $^4\Delta$. Here the Born correction is only applied to the $^2\Pi$ excitation, as this is the only dipole-allowed transition. All three excitation cross sections show resonance features. These are particularly pronounced in the CC-MRCI calculations; we note that cross sections approximately average the SCF-CC ones which show fewer resonances. Although it is likely that these cross sections display resonance features, they can only be properly characterised by much larger calculations than the one presented here.

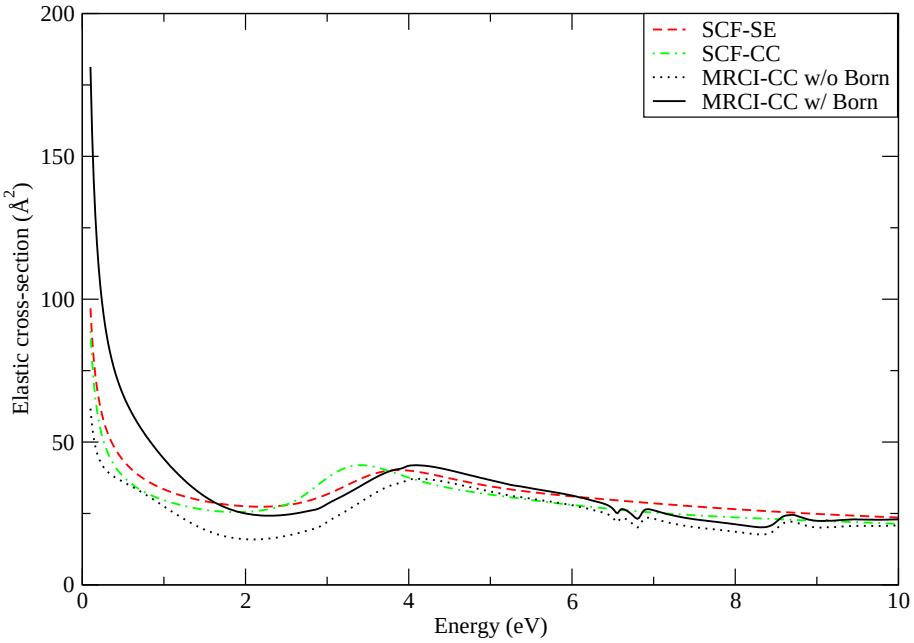

Figure 7.3: Elastic Cross-Section for electron C_2H collisions

7.7 Conclusions

The presence of electronic resonance features above 1 eV for this molecule suggests that formation of temporary negative ions by electrons trapped in these resonance states is an unlikely mechanism for radiative electron attachment in the ISM. This is because 1 eV converts to a much higher temperature than electrons are found at in the ISM, making it highly unlikely electrons will reach the energies required to become temporarily trapped in the resonance states.

The more likely possibility is that the molecular anions observed may be arise from the very weakly bound anionic states, as found for C_3N^-. These states will support nuclear excited states which lie in the continuum and therefore are resonances. We note that C_2H^- appears not to support such states. If this mechanism does explain the formation of such anions, C_3N^- would be observed in large quantities but C_2H^- would not. This prediction appears to match current observations.

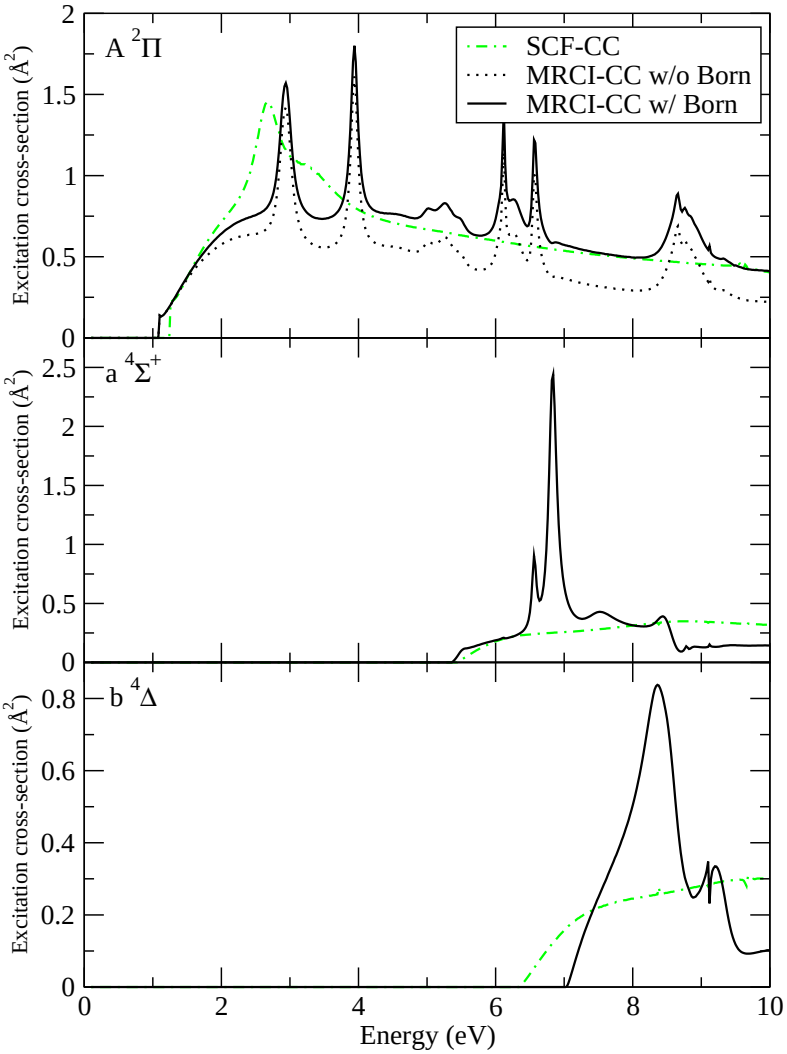

Figure 7.4: Electron impact electronic excitation cross sections for C_2H final state: A $^2\Pi$, a $^4\Sigma^+$ and b $^4\Delta$.

Chapter 8

Atomic Oxygen

8.1 Introduction

Atomic oxygen (figure 8.1) is one of the most abundant elements in the universe and can be found in a wide range of environments such as astrophysical and industrial plasmas (Goicoechea et al., 2009; Ershov and Borysow, 2007) and planetary atmospheres (Gerarda et al., 2008; Hall et al., 1995). This atom is extremely reactive and thus has a short lifespan unless it exists in an environment where its continually produced, such as Earth's low-orbit atmosphere (Hecht et al., 1995), where ultra-violet radiation continually splits its molecular parent. This leads to this environment being composed of 96% atomic oxygen, historically leading to problems with the erosion of spacecraft passing through (Packirisamy et al., 1995). The reactive nature of atomic oxygen has also led to it being used in cleaning processes for paintings and surgical instruments, where removal of organic hydrocarbons which may not be removed by other means is desired.

The abundance and variety of environments in which the element is found means it

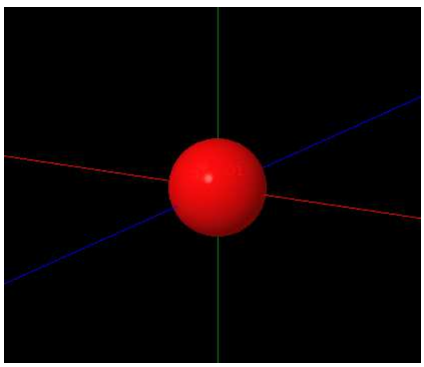

Figure 8.1: The Oxygen atom (taken from Quantemol-N)

is crucial to understand the processes which it can undergo. This is especially important in both astrophysical and industrial plasmas, which require a key understanding of environmental chemistry to model and understand what is happening.

The motivation behind this chapter is a direct influence from my work with Quantemol. Shortly after supplying Quantemol-N to Dublin City University (DCU), I was contacted by Dr. Bernard Keville in order for me to act as support in his use of it. After some successful initial work, Bernard asked if it was possible for Quantemol-N to carry out calculations on electron-atom collisions, in particular oxygen. In particular Bernard was interested in theoretically re-producing the excitation cross-section which leads to the ^{3}P-^{3}S^o emission line at 844 nm. This line is caused by an electron excitation between ground and excited ^{3}P states, before de-excitation to the ^{3}S^o state. The aim of this calculation would be to theoretically re-produce the 844 nm excitation cross-section found in Katsch et al. (2000). After initial investigations it was determined that Quantemol-N would be unable to carry out the electron-oxygen scattering calculation. This was because using D_{2h} molecular symmetry to reproduce spherical symmetry became problematic for excitations, where a breaking of the required degeneracies between D_{2h} symmetries occurred. Note that the UK molecular R-matrix codes cannot be run using spherical symmetries, but only use Abelian symmetries, thus D_{2h} symmetry is used as it contains the most symmetry, thus leading to the fastest calculation. The symmetry issue was further complicated by the ^{3}P ground state of oxygen, which proved difficult to reproduce in Quantemol-N. It was therefore decided that I would run R-matrix calculations in an attempt to produce the required data, as manual manipulation of the input files would allow for a fine-tuning of the results as opposed to the automated approach of Quantemol-N.

A significant amount of experimental work has been done concerning oxygen in plasmas (e.g. Ershov and Borysow (2007); Booth et al. (1991)), and a small number of previous atomic R-matrix calculations on electron-oxygen scattering do exist. Primarily the RMPS calculations of Thomas et al. (1997), and the modified B-spline R-matrix method with non-orthogonal orbitals of Zatsarinny and Tayal (2001). These calculations however do not include results for the required ^{3}P-^{3}P excitation cross-section. No other theoretical cross-sections for this excitation have been found, thus this chapter gives the first theoretical cross-section for the ^{3}P-^{3}P excitation by electron impact. The R-matrix method has also been used to calculate oscillator strengths for the allowed

transitions (Bell and Hibbert, 1990). An extensive summary of all atomic oxygen collision cross-sections, used as the benchmark in this work, has also been created (Itikawa and Ichimura, 1990).

This chapter represents the first serious use of the UK molecular R-matrix codes (Carr et al., 2012) to model an electron-atom interaction. Whilst in principle the codes are able to correctly model this, a number of minor difficulties were encountered. Thus the aim of this chapter is to not only present the data calculated, but also to explain the process of how to run an atom in the codes and the factors which must be known about.

8.2 Method

Whilst the work in this chapter primarily follows the standard procedure outlined in Chapter 3 and used in the other chapters, there are a few key points of note to consider when carrying out an electron-atom collision using the molecular codes.

- Establishing the correct electron configuration of the ground state in D_{2h} molecular symmetry when applied to an atom.
- Ensuring that excited atomic states are correctly described by the appropriate degenerate D_{2h} states. Here we note that the D_{2h} states only share degenerate energies as they are describing a species with a higher symmetry (in this case, atomic spherical symmetry).
- Making sure the input files for the running of the code have the appropriate changes to reflect the above.

It is important to note how each of these were dealt with in order to successfully run an atomic calculation with molecular codes.

1. *The oxygen ground state:* As previously mentioned, atomic oxygen has a ^{3}P ground state, this is quite an awkward state to create in the D_{2h} molecular representation. Table 8.1 shows the neccesary conversion between atomic and the molecular symmetries, clearly a P-state requires 3 degenerate molecular states. In order to create the correct ground state, the following electron configuration was used a_g^2, b_{1g}^2, b_{2g}^2 & b_{3g}^2. This reflects the electron configuration in spherical (atomic) notation of $1s^2$, $2s^2$, $2p^4$.

Table 8.1: Conversion relations between spherical atomic state symmetries and molecular states of D_{2h} symmetry

Atomic State	Corresponding Degenerate D_{2h} States
S	A_g
S^o	A_u
P	B_{1g}, B_{2g}, B_{3g}
P^o	B_{1u}, B_{2u}, B_{3u}
D	A_g, A_g, B_{1g}, B_{2g}, B_{3g}
D^o	A_u, A_u, B_{1u}, B_{2u}, B_{3u}

2. *Excited states:* A common practise in atomic R-matrix calculations is to manually shift the energies of excited states so that they match experimental values (e.g. Hudson et al. (2012)). It was crucial to do this in these calculations for two reasons. First, so that the excited ^3P state is at the same threshold as found in the experimental work of Katsch et al. (2000), and secondly to ensure that the excited states retain the necessary state degeneracies in order to correctly reproduce the atomic states in the D_{2h} molecular symmetry used in the calculation. There is further discussion of this below, with table 8.3 showing the energy shifts I had to impart on each of the molecular target states in order to retain the correct degeneracies, whilst also ensuring they were at the experimental excitation energies.

3. *Adapting the input files to correctly impart energy shifts:* This took the most time to correctly configure due to some experimentation. Whilst energy shifting is contained in the code documentation, there is no guide which explains the process from start to finish. Hence I have created a framework here with which future users can use when attempting similar atomic calculations. Table 8.2 provides this, and also contains the atom-specific changes which are required during the running of certain code modules.

8.3 Calculation Details

For this R-matrix calculation the aug-cc-pVQZ basis set was chosen (Dunning, 1989). Initial investigation with cc-pVnZ (n=D,T,Q) basis sets led to poor target results, further discussion led to the conclusion that an augmented basis set was required to take into

Table 8.2: Framework for running an atom (as opposed to a molecule) - electron collision calculation in the UK Molecular R-matrix codes

	Task	Additional Comments
1	Run the target calculation	Make sure the correct electron configuration in D_{2h} is established in order to correctly create the atomic ground state.
2	Observe state energies	These are found in the fort.24 file.
3	Determine which states should be degenerate to resolve atomic states	Comparison with experimental energies is useful here.
4	Calculate a 'shift energy' for each state to make appropriate D_{2h} states degenerate	Also a good idea to include a shift which makes the atomic state match the experimental value.
5	The N+1 inner region jobfiles need an addition	The 'ESHIFT' variable must be added to the N+1 SCATCI's, this is an array of energy shifts (in Hartree) in the same order as states in CONGEN.
6	Outer region addition	SWINTERF needs an 'ESHIFT' array included, this array of energies should be in fort.24 order of states.
7	Outer region change	The 'IDTARG' array in SWINTERF is created using the same process as normal (i.e. All instances of the first state, then all instances of the next state etc.). However, this process must be applied to the 'post-shift' energy ordering of states, NOT the fort.24 ordering.

consideration the 'Rydberg-like' nature of the oxygen atom, particularly in its excited states. Larger basis sets were not investigated due to time limitations. The diffuse nature of the basis set used also meant an increase of the R-matrix radius from the standard 10 a_0 to 12 a_0. This was to ensure that none of the target wavefunction leaks outside of the R-matrix sphere, as tests run at 10 a_0 suggested this was happening. In order to produce a set of 'base-example' job files, a Quantemol-N CI calculation was carried out using the correct basis set and electron configuration (see below). Whilst this calculation did not produce any usable results, it provided a complete suite of calculation jobfiles which were then edited (in order to, for example, add the energy shifts) in order to run the correct calculation manually.

The target CI calculation kept $(1a_g)^2$ frozen, with an active space of (2-4a_g, 1-2b_{1u}, 1-2b_{2u}, 1-2b_{3u}, 1b_{1g}, 1b_{2g}, 1b_{3g})^6. State energies were calculated for 48 states, 3 states for each of the 8 D_{2h} symmetries, for both singlet and triplet spins. However I then

limited the scattering calculation to keep only 26 states in the outer region. This was judged by analysis of the state energies, beyond the 26 states the D_{2h} state degeneracies became too mixed up between states and it proved too difficult to resolve the atomic states from these. Table 8.3 shows the 26 states which were retained and had energy shifts applied. Note that the energy shifts not only increase the degeneracy of states in order to re-create the atomic states, they also adjust the energy of the resultant degenerate states so they match the experimental data of Itikawa and Ichimura (1990). The excitation cross-section calculated was for the excitation from the ^{3}P ground state to the 10.99 eV ^{3}P excited state.

Scattering calculations were propagated to 30.1 a_0 and upon the request of DCU results were calculated up to an electron scattering energy of 100 eV. Standard R-matrix calculations normally provide stable results up to the first ionisation energy, and then a high-energy treatment is used to extend the range. The ionisation energy of atomic oxygen is around 13.6 eV, so extending the range up to the required 100 eV had the potential to provide spurious results for the majority of the energy range. This problem is amplified by the fact that the ^{3}P-^{3}P transition is dipole forbidden, therefore the standard high-energy BEf approximation (Kim, 2001, 2007) could not be applied to the cross-section.

One important point of note is the extraction of an excitation cross-section between the atomic states when using the D_{2h} molecular symmetry. To obtain the correct cross-section, one must extract the cross-section going from one of the degenerate initial states to one of the degenerate final states. Multiplication and division factors may then be applied depending on the degeneracies of the states involved. For example in this work (the ^{3}P-^{3}P transition) I first extracted the excitation cross-section going from the $^3B_{3g}$ to the excited $^3B_{3g}$ state with the 'post-shift' value of 10.99 eV. Degeneracy rules can then be applied in order to increase or decrease the cross-section. E.g. the oxygen ^{3}P ground initial state is made of 3 degenerate molecular states, so the cross-section is decreased by a factor of 3, however the final ^{3}P state is also triply-degenerate, so we increase the cross-section by a factor of 3. Hence the overall effect these rules have in this case is nullified. Thus

$$\sigma(^3P -^3 P) = \sigma(^3B_{3g} -^3 B_{3g}). \tag{8.1}$$

In general the degeneracy rules can be applied as follows (where n and m represent the degeneracies of the initial (x) and final (y) molecular states of the excitation respectively,

Table 8.3: Energy shifts required to make atomic states from molecular states (note the states are presented in the order of the 'pre-shift' original target calculation). Shifts are applied to make state energy match the experimental values of Itikawa and Ichimura (1990).

Target E_h	D_{2h} State	Vert. Exc. En. (eV)	Shift (eV)	Atomic State	Exp. En. (eV)
-74.539	$^3B_{3g}$	0.000	0.000		
-74.539	$^3B_{1g}$	0.004	-0.004	^3P	0.00
-74.538	$^3B_{2g}$	0.007	-0.007		
-74.471	^1A_g	1.849	0.121		
-74.469	^1A_g	1.900	0.020		
-74.463	$^1B_{2g}$	2.070	-0.320	^1D	1.97
-74.459	$^1B_{1g}$	2.161	-0.504		
-74.458	$^1B_{3g}$	2.186	-0.553		
-74.406	^1A_g	3.617	0.573	^1S	4.19
-74.035	^3A_u	13.715	-4.195	$^3S^o$	9.52
-74.011	$^3B_{3u}$	14.362	-0.242		
-74.011	$^3B_{1u}$	14.366	-0.251	$^3P^o$	14.12
-74.010	$^3B_{2u}$	14.398	-0.315		
-74.004	^3A_u	14.558	-2.468		
-74.001	$^3B_{2u}$	14.624	-2.600		
-74.000	$^3B_{1u}$	14.655	-2.662	$^3D^o$	12.09
-74.000	$^3B_{3u}$	14.663	-2.677		
-73.999	^3A_u	14.684	-2.721		
-73.969	$^3B_{3g}$	15.495	-4.505		
-73.969	$^3B_{1g}$	15.504	-4.522	^3P	10.99
-73.968	$^3B_{2g}$	15.529	-4.573		
-73.954	$^1B_{3u}$	15.920	-3.190		
-73.953	$^1B_{1u}$	15.932	-3.214		
-73.951	$^1B_{2u}$	15.987	-3.324	$^1D^o$	12.73
-73.945	^1A_u	16.149	-3.648		
-73.942	^1A_u	16.237	-3.825		

and the true atomic states are given by i (initial) and j (final):

$$\sigma_{ij} = \frac{m}{n}\sigma_{xy} \tag{8.2}$$

The ^{3}P-^{3}P cross-section could have also been extracted by finding the cross-section between any of the degenerate molecular states in the ^{3}P ground state, to any of the degenerate molecular states that make up the final ^{3}P state. After checking the data this was confirmed.

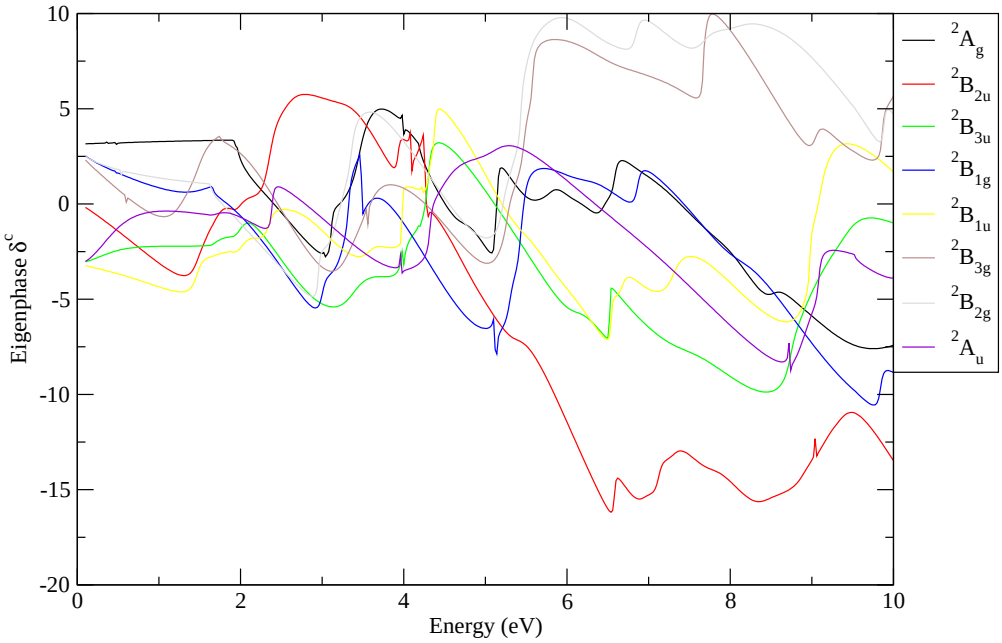

Figure 8.2: Eigenphase sums of the doublet O^- states

8.4 Scattering Results

8.4.1 Eigenphase Sums

Eigenphase sums were calculated up to 100 eV, however beyond the ionisation energy these can become unstable and erratic. Thus here we present the scattering eigenphase sums up to a 10 eV (figures 8.5 and 8.6). Beyond this energy scattering observables can become unstable, an example of this is the dramatic increase of the eigenphase sums above 10 eV (not shown). One prominent point of note from the eigenphase sums is that the D_{2h} scattering states which should be degenerate for atomic symmetry (e.g. $^2B_{1g}$, $^2B_{2g}$, $^2B_{3g}$ to describe ^2P) are not, this is a consequence of applying the energy shifts to the target states. This became evident when comparing to the results of the Quantemol-N calculation, in which no energy shifts were applied. In this calculation the eigenphase sums of the degenerate scattering states were indeed identical. However as previously mentioned the ^3P-^3P cross-section from the Quantemol-N calculation did not agree at all with the cross-section of Katsch et al. (2000). Another important point of note is the role of pseudo-resonances, which are excited target states lying above the ionisation threshold.

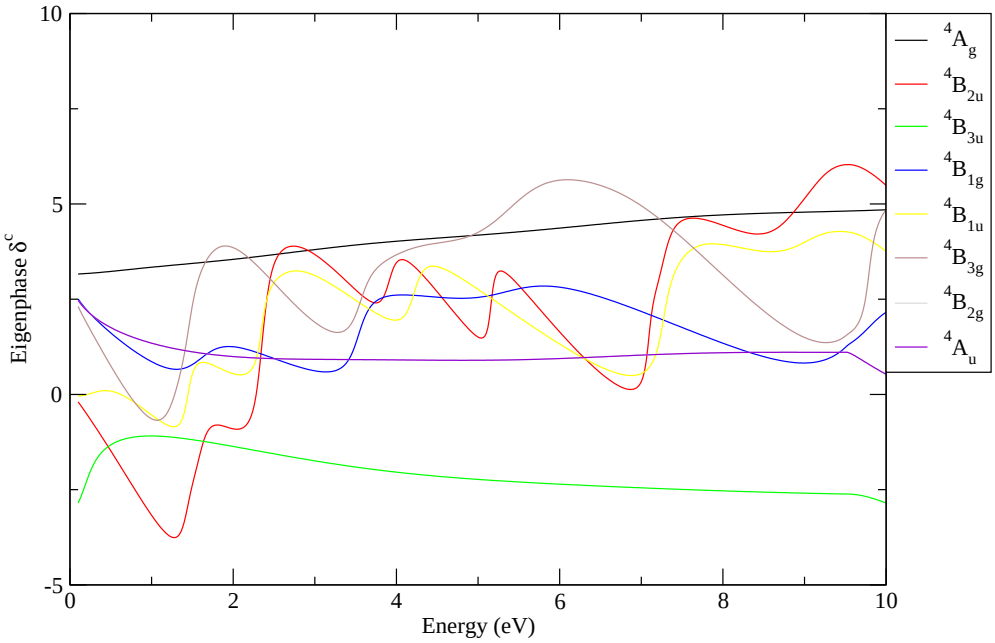

Figure 8.3: Eigenphase sums of the quartet O^- states

8.4.2 ^{3}P-^{3}P Cross-Section

Figure 8.7 presents the final calculated electron impact cross-section for the ^{3}P-^{3}P excitation, up to an energy of 100 eV, this was done purely using the R-matrix method without application of any high-energy approximations. Here we have applied Gaussian smoothing to our data to reduce the noise caused by pseudo-resonances (Gorfinkiel and Tennyson, 2005), carried out via a Fortran subroutine (*J. Gorfinkiel, private communication*). By comparison of this work to the Katsch data we can see there is a good match, particularly in the threshold region. The magnitude and shape of the overall cross-section matches excellently, including the early peak around 30 eV and also the tail of the cross-section which levels off at around 0.02 Å^2. Clearly the theoretical data shows many more features compared to the smooth nature of the experimental result, this can be attributed to a large number of pseudo-resonances which present themselves in the theoretical calculation, and also the slight numerical instability of the R-Matrix method above ionisation.

8.5 Conclusions

Here I have presented the first known attempt at running an electron-atom scattering calculation using the UK molecular R-matrix codes. There are a number of key points

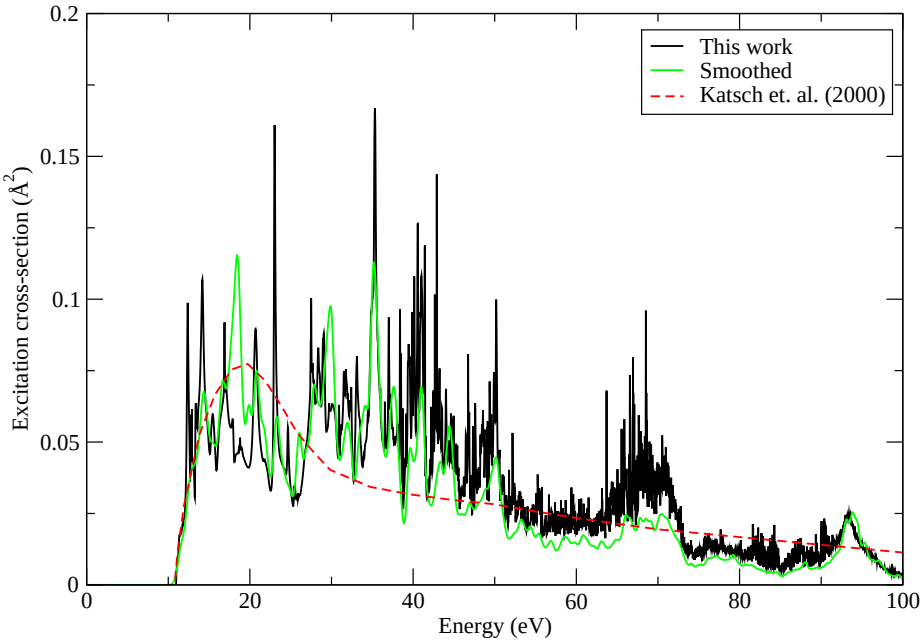

Figure 8.4: Atomic Oxygen ^{3}P-^{3}P excitation cross-section, leading the emission of the 844 nm spectral line

which require attention when carrying out such an exercise, and in the example of atomic oxygen this was not helped by the non-standard nature of the ground state. However I feel the attempt was successful and the theoretical cross-section matches the experimental result excellently despite the issues, including the fact that the R-matrix method is not designed to go to such high energies above ionisation. When presenting the data to Bernard Keville at DCU he was extremely happy with the results, and thus I feel as a proof of concept exercise for running atoms using the molecular code, it has been successful.

Chapter 9

NaI

9.1 Introduction

NaI (figure 9.1) is an alkali halide with 64 electrons, and is commonly used as a food supplement to treat and prevent iodine deficiency. It can also be activated with thalium and used in scintillation detectors. This is because activated NaI emits photons when exposed to ionizing radiation, this is traditionally the most widely used of the current scintillation materials as it gives the highest light yield. NaI also has a radioactive isotope, $Na^{131}I$, which is used in the treatment of cancer and hyperthyroidism.

The motivation behind investigating electron scattering with the NaI molecule came directly from my work with Quantemol. Mark Kushner, director of the computational plasma science and engineering group at the university of Michigan, requested we carry out electron scattering calculations on a number of molecules used in plasmas, with NaI being one of the molecules in question. The data requested included elastic and inelastic cross-sections up to 100 eV.

A literature search reveals there is no previous electron scattering data for this molecule, either experimental or theoretical. The majority of existing work concerns potential curves (e.g. Sandrone and Dixon (1998), Kim et al. (2001)), photo-dissociation data (e.g. Ziesel et al. (2001), Hosseini et al. (2005)) and molecular dynamics (e.g. Martinez and Levine (1996), Nakagami et al. (2002)). I was also unable to find energies for the ground and excited states for comparison with the results presented here.

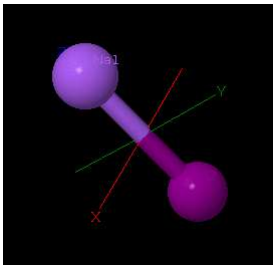

Figure 9.1: The molecule NaI (taken from Quantemol-N)

9.2 Calculation Details

The electron-molecule collision calculations were carried out solely using Quantemol-N (section 3.6). Whilst the NaI molecule has the irreducible symmetry of $C_{\infty v}$, this is not possible in Quantemol-N. Instead C_{2v} symmetry was used, with conversion back to the true $C_{\infty v}$ states being relatively trivial. The target calculation was a full configuration interaction with 8 states in total (the 4 state symmetries in both singlet and triplet spin multiplicities, 1 state per symmetry). A bond length of 2.71 Å was taken from the experimental data of Herzberg and Huber (1979), and the 3-21G basis set has been used for the calculation (Dobbs and Hehre, 1987). The R-matrix radius has been set to 13 a_0, and the scattering propagated out to 100 a_0. The electronic configuration of the ground state was chosen as $(1\text{-}16a^1, 1\text{-}7b^1, 1\text{-}7b^2, 1\text{-}2a^2)^{64}$, and for the configuration interaction the $(1\text{-}12a^1, 1\text{-}5b^1, 1\text{-}5b^2, 1a^2)^{46}$ orbitals were frozen, with an active space of $(13\text{-}16a^1, 6\text{-}7b^1, 6\text{-}7b^2, 2a^2)^{18}$. Scattering variables were calculated up to 100 eV.

9.3 Target Results

The energy of the X $^1\Sigma^+$ ground state is calculated to be -7048.24 Hartree, with some low-lying excited states also found (table 9.1). Note that as the target calculation only ran for 1 state per symmetry, it is possible that a low-lying excited state of the same spin-symmetry as the ground state could exist, however it would not be detected in this particular piece of work. A very large ground state dipole moment of 10.05 Debye (in the direction of the Na atom) is calculated, which compares well to the literature (table 9.2).

Table 9.1: Vertical excitation energies from the X $^1\Sigma^+$ state.

Excited state	Vertical exc. en. (eV)
a $^3\Pi$	4.163
A $^1\Pi$	4.218
b $^3\Sigma^+$	4.544

Table 9.2: NaI groud state dipole moment literature comparison

Source	Method	μ (D)
This work	CI	10.05
Sakai et al. (1992)	MRSDCI	9.41
Hebert et al. (1968)	Experimental	9.21

9.4 Scattering Results

Figure 9.2 shows the eigenphase sums for the Doublet NaI^- scattering states up to 10 eV. The corresponding resonance data is given in table 9.3.

Figure 9.3 gives the elastic cross-section up to 100 eV, here it is clear that the Born correction dramatically changes the cross-section at low energies. For example at 10 eV the Born corrected cross-section is almost 2000 Å larger than the non-Born value. At higher energies this also results in the Born corrected cross-section levelling at around 100 $Å^2$, a much larger value than the non-corrected value. Figure 9.4 contains the BEB ionisation cross-section up to 5000 eV, this is calculated as part of Quantemol-N. Here a peak of around 3.2 $Å^2$ occurs at about 200 eV, with values at higher energies tailing off to about 0.55 $Å^2$ at 5000 eV.

Figure 9.5 contains the electron-impact excitation cross-sections for the excitations of the ground state to the first three excited target states (given in table 9.1). For both the $^2\Pi$ excitations we can see a pronounced enhancement of the cross-section at 4.2 eV, this is due to the $^2\Pi$ scattering resonance found at 3.74 eV. Also note that the peak is much larger (1 $Å^2$ c.f 0.2 $Å^2$) and the higher energy plateau is about twice as large (0.1 $Å^2$ c.f. 0.05 $Å^2$) for the ΔS=1 Π transition compared to the Δ S=0 Π transition. The

Table 9.3: NaI^- doublet resonance positions (and widths) in eV, below 10 eV

Π	0.662 (0.214)
	3.740 (0.003)
Σ^-	4.950 (0.298)
Δ	7.133 (0.601)

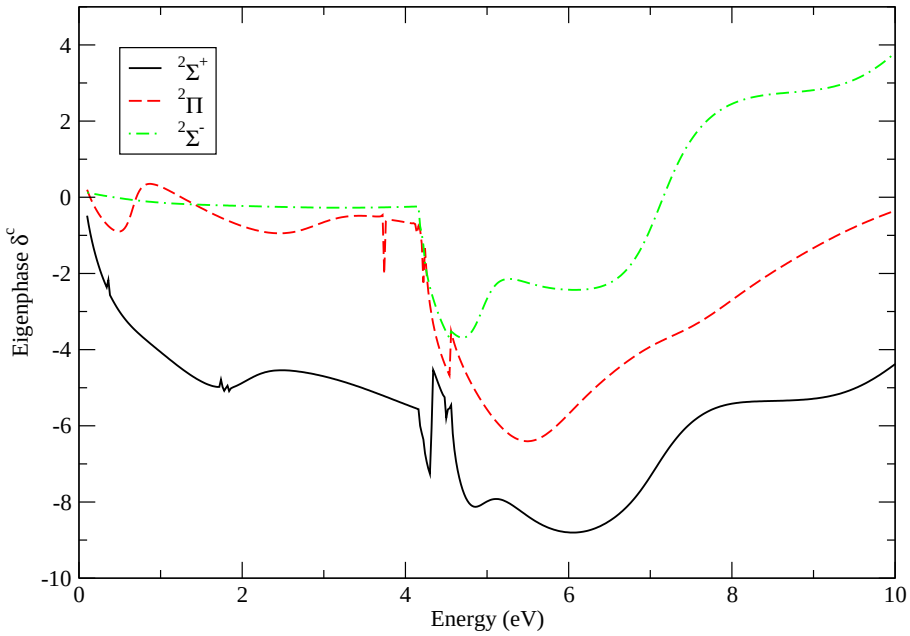

Figure 9.2: NaI eigenphase sums

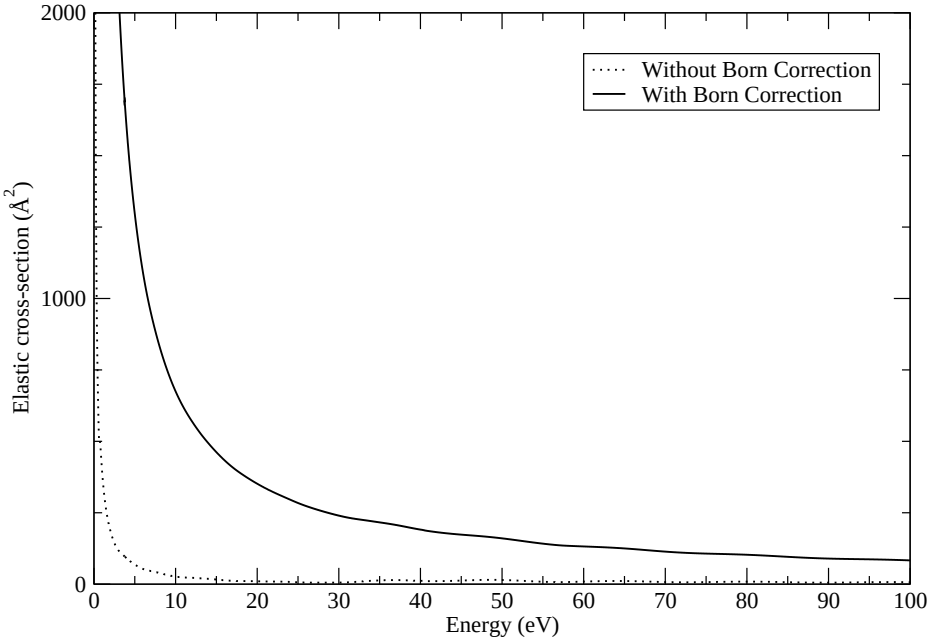

Figure 9.3: NaI elastic cross-section

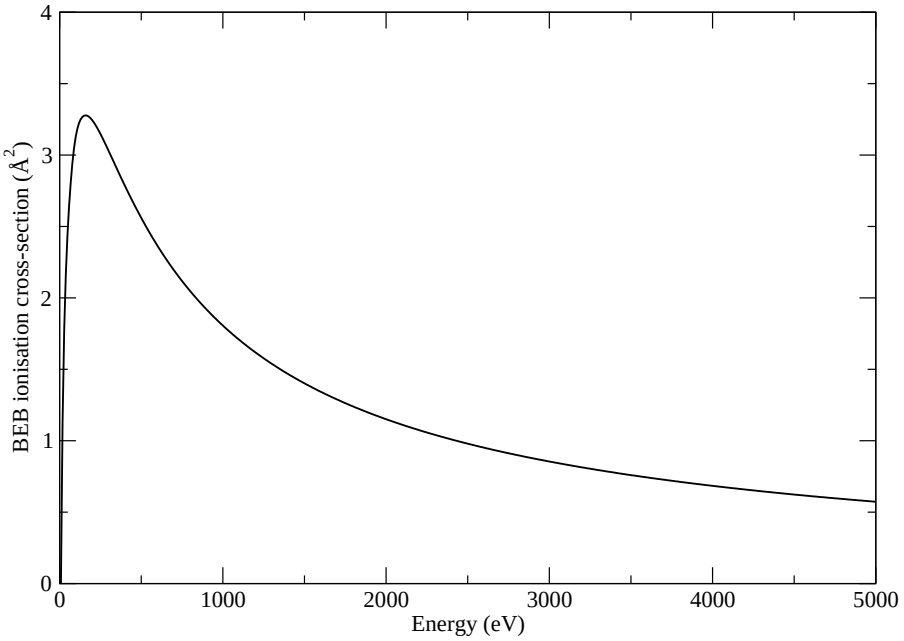

Figure 9.4: NaI BEB ionisation cross-section

X $^1\Sigma^+$-b $^1\Sigma^+$ excitation cross-section has a pronounced peak of 1.5 Å^2 just above 6 eV. I believe this could be due to the $^2\Delta$ resonance at 7.133 eV, which has a width large enough to bring the peak into its range. Beyond this peak the cross-section remains fairly stable at 0.1 Å^2 between 7.5 - 10 eV.

Figure 9.6 presents the high energy approximation of the excitation cross-section using the BEf method (Kim, 2001, 2007). Here we note this method is only applicable to dipole allowed transitions and thus only the cross-section for the X $^1\Sigma^+$ - A $^1\Pi$ transition has been calculated. The calculated dipole transition moment used in this method for this transition is 9.58 Debye, taken from the target calculation fort.24 output. In this figure we see an early peak of 0.51 Å^2 at about 10 eV, before steadily levelling off to 0.04 Å^2 at 1000 eV.

Finally figure 9.7 gives the reaction rate co-efficients for the scattering calculation. This is a standard Quantemol-N result calculated by applying a Boltzmann-type distribution to the elastic cross-section. The rate coefficient is maximised at around 2500 K, with a value of 4.5×10^{-5} cm^3/s, before steadily decreasing down to 3.5×10^{-5} cm^3/s at 10,000 K.

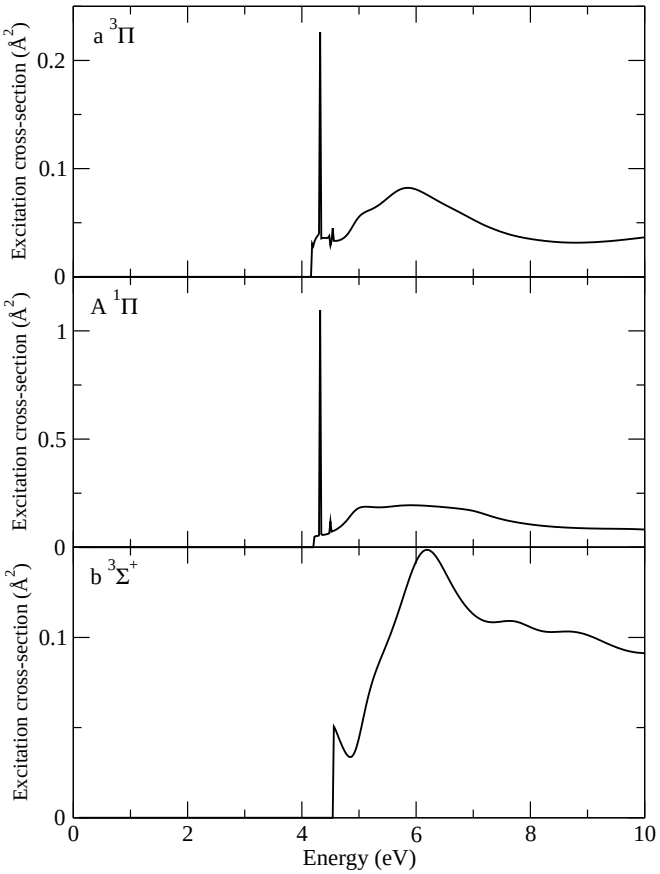

Figure 9.5: NaI excitation cross-sections from the X $^1\Sigma^+$ state to the a $^3\Pi$, A $^1\Pi$, and b $^3\Sigma^+$ states.

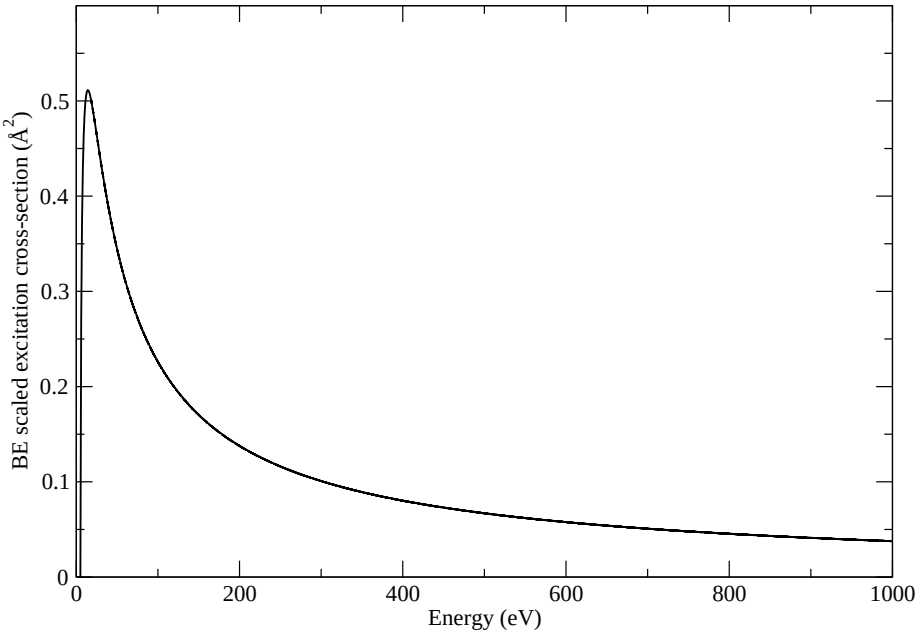

Figure 9.6: NaI scaled BEf excitation cross-section for the dipole allowed X $^1\Sigma^+$ - A $^1\Pi$ transition.

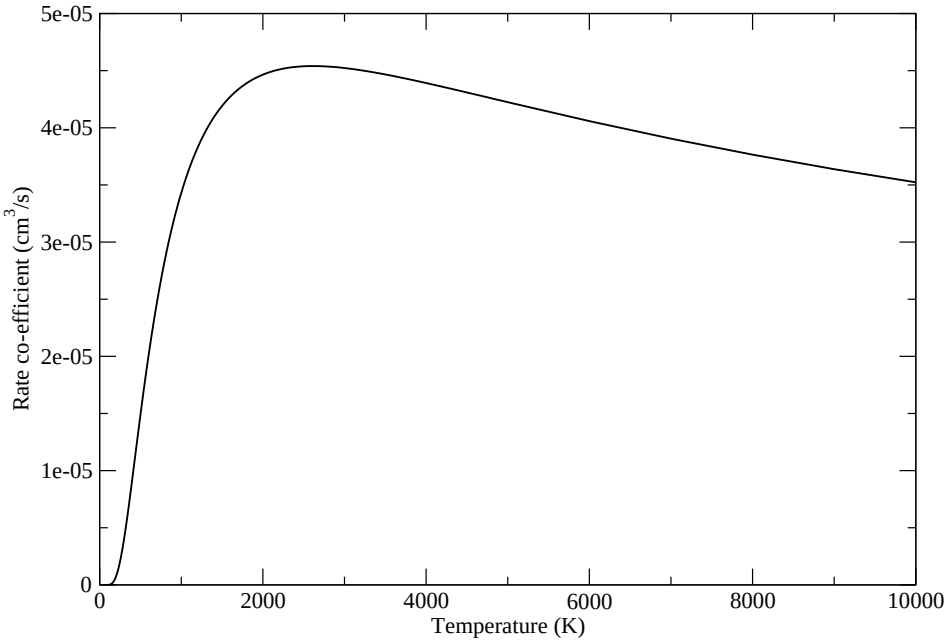

Figure 9.7: NaI reaction rate coefficients for elastic electron scattering as a function of Temperature.

9.5 Conclusions

In this chapter I have carried out electron scattering on the NaI molecule. An 8-state CI model was used and a ground state energy of -7048.24 Hartree has been found, of $^1\Sigma^+$ symmetry. Furthermore three relatively low lying excited states have been found between 4.0 and 4.6 eV, of $^3\Pi$, $^1\Pi$ and $^3\Sigma^+$ symmetries. Although here it should be noted that the target calculation only included one state-symmetry combination, therefore there may exist a second $^1\Sigma^+$ state lower than 4 eV in energy. The calculated X $^1\Sigma^+$ ground state dipole moment was found to be 10.05 Debye, which matches well with experimental values between 9.2 - 9.4 Debye. A CC scattering model has been used to calculate scattering observables up to 100 eV, although eigenphase sums and resonance parameters have only been considered up to 10 eV due to the presence of pseudo-resonances above ionisation threshold. Resonances were found of $^2\Pi$, $^2\Sigma^-$ and $^2\Delta$ symmetries and these acted to enhance the excitation cross-sections. The Born correction has been applied to the calculated total elastic cross-section and this leads to a dramatic increase in the cross-sections magnitude between 0-100 eV, but particularly at the lower energies. This is due to the large dipole moment of the ground state making the Born correction bigger, as this increases with the square of the dipole moment value. Finally, the BEB ionisation cross-section (up to 5000 eV), the X $^1\Sigma^+$ - A $^1\Pi$ BEf excitation cross-section (up to 1000

eV), and reaction rate co-efficients (up to 10000K) have been presented.

In terms of applying this data to the modelling of industrial plasmas, there is more emphasis placed upon the high-energy results (those above the ionisation threshold of the molecule). This is simply because industrial plasmas carry free electrons with a much larger energy than are found interstellar environments (such as found in the previous chapters). Therefore it is likely the key data which can be used from this chapter will be the cross-sections which go up to high energies, such as the BEB ionisation, BEf excitation, and elastic total cross-sections. Low-lying resonances are less likely to be as important compared to the large-scale trend and magnitude of these cross-sections.

Chapter 10

SiBr & $SiBr_2$

10.1 Introduction

Both SiBr and $SiBr_2$ are metal halides which can occur in industrial plasmas when silicon is etched by products such as hydrogen bromide. As these species can then exist in the plasma itself it is necessary to understand how they interact with the free electrons that are available. The calculations in this chapter were carried out as part of some work Quantemol carried out with an industrial partner. The electron-impact cross-sections calculated here were subsequently used to increase the level of sophistication of plasma models, which have historically not included complete sets of reactions possible within the plasma.

No previous electron scattering investigations have been carried out for these molecules, with SiBr investigations mainly concentrating on spectroscopic properties and analysis (Jevons and Bashford, 1937; Rao and Haranath, 1969; Ishiguro et al., 1995), its Rydberg states (Bossier et al., 1984), and has also been used in analysis of the fine-structure constant (Beloy et al., 2010). A literature check for $SiBr_2$ suggests that most work has concentrated on the structure and vibrational energetics of the molecule (Hargittai et al., 1983; Coffin et al., 1989; Gershikov et al., 1990).

10.2 SiBr

10.2.1 Calculation Details

Two calculations were carried out for SiBr, one using a Hartree-Fock target and static-exchange scattering model, the other using a configuration interaction target (allowing

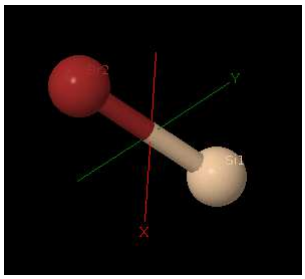

Figure 10.1: The molecule SiBr (taken from Quantemol-N)

Table 10.1: SiBr target calculation data.

Method	Ground State	Energy (H)	μ (D)
HF	$^2\Sigma^+$	-2861.12	3.51
CI	$^2\Pi$	-2861.24	4.14

excitations from the ground state) followed by the close coupling scattering method. Both of these calculations were carried out using Quantemol-N (section 3.6). For these calculations the equilibrium bond length of 2.64 Å was used, found by carrying out a relaxation in MOLPRO (Werner et al., 2008), and making use of the c_{2v} symmetry. The ground state electron configuration for both HF and CI models being (1-14a_1 1-5b_1 1-5b_2 1a_2)^{49}, with the single electron in the 14a_1 orbital. For the CI calculation 28 electrons were frozen in the (1-8a_1 1-3b_1 1-3b_2) orbitals, with the remaining 21 electrons in an active space of (9-14a_1 4-6b_1 4-6b_2 1a_2). An R-matrix radius of 10 a_0 was chosen to fully encompass the target wavefunction created using the 6-311G basis set.

10.2.2 Target Data

The HF target calculation produces a $^2\Sigma^+$ ground state, which becomes $^2\Pi$ in the CI calculation, with the $^2\Sigma^+$ state becoming the first excitation. Both models have a large dipole moment in the direction of the bromine atom, with the CI model having the larger value by 0.6 D. Table 10.1 summarises these results and table 10.2 gives the first three excited states from the CI model. No information for comparison could be found in the literature for any of these values.

10.2.3 Scattering Results

For the scattering results we note that Koopman's theorem indicates an ionisation energy of 4.53 eV for SiBr, due to this we will only consider resonances up to 5 eV, as any above

Table 10.2: SiBr vertical excitation energies from the X $^2\Pi$ state.

Excited state	Vertical exc. en. (eV)
A $^2\Sigma^+$	2.10
a $^4\Sigma^-$	2.67
b $^4\Pi$	3.32

Table 10.3: SiBr resonance positions (and widths) in eV for the CI-CC model, ^{a} Resonance present in eigenphases but not fitted by RESON.

State	Position (Width)
$^1\Sigma^+$	4.997 (0.035)
$^1\Pi$	3.919 (0.129)
$^1\Sigma^-$	4.6a
$^1\Delta$	4.875 (0.031)
$^3\Sigma^+$	4.061 (0.330)
$^3\Pi$	2.719 (0.159)
	4.863 (0.218)
$^3\Sigma^-$	4.620 (0.217)
$^3\Delta$	4.061 (0.330)
	4.620 (0.217)

this will be pseudo-resonances. Figures 10.2 and 10.3 give the scattering eigenphase sums for the electron-SiBr collision for static-exchange and close-coupling models (although no shape resonances were detected in the static-exchange model). The associated resonance data (up to 5 eV) can be found in table 10.3. Feshbach resonances are detected in the $^1\Sigma^+$, $^1\Pi$, $^1\Sigma^-$, $^1\Delta$, $^3\Pi$, and $^3\Delta$ symmetries, there is also a $^1\Delta$ resonance which appears at 4.87 eV (with a width of 0.03 eV) in both the $^1\Sigma^+$ and $^1\Sigma^-$ symmetries. We note that the two $^3\Delta$ resonances were fitted using the RESON data from the $^3\Sigma^+$ and $^3\Sigma^-$ respectively. This was because RESON did not detect the 4.06 eV resonance in $^3\Sigma^-$ or the 4.62 eV resonance in $^3\Sigma^+$, despite them both being present in the eigenphase diagram.

Figure 10.4 gives the elastic cross-section for the static-exchange and close-coupling scattering models, with a Born correction also applied to the CC model in order to correct and enhance the low-energy magnitude of the cross-section. Both the SE and uncorrected CC cross-sections are very similar however once the Born correction is applied there is a large enhancement at the lower energies. All three variations level off at higher energies to about 50 Å^2. Figure 10.5 is the BEB ionisation cross-section up to 5000 eV for both

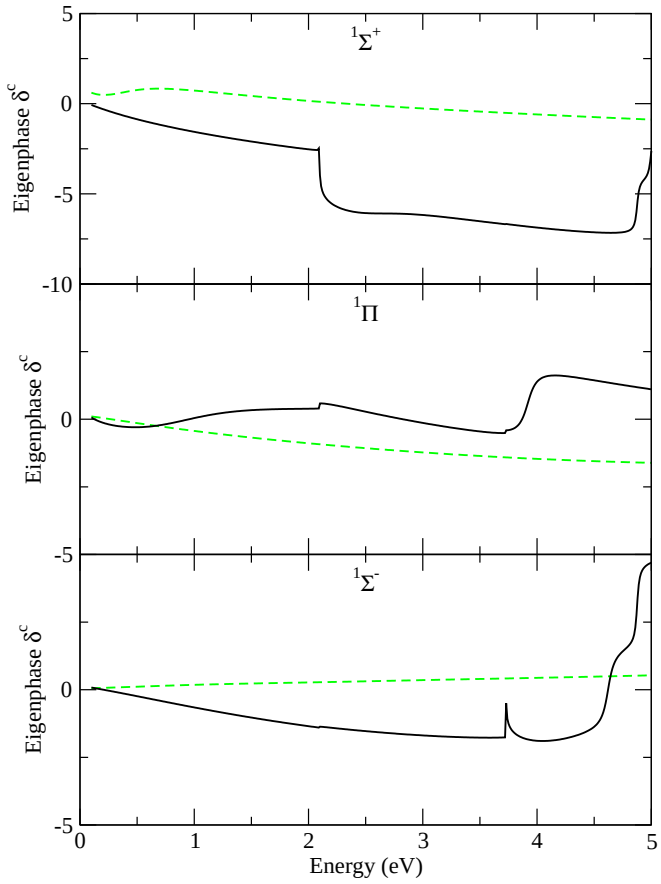

Figure 10.2: $SiBr^-$ singlet scattering eigenphases for the SE (dashed) and CC (solid) models.

the SE and CC models, created using the BEB approximation from the orbital energies. These both have an early peak at about 100 eV, with the SE peaking at just over 7 $Å^2$ and the CC at 9 $Å^2$. Both models then decrease down to 0.75 $Å^2$ by 5000 eV.

Excitation cross-sections for the first three excitations out of the X $^2\Pi$ ground state are given in figure 10.6. The first excitation is the dipole allowed transition to the A $^2\Sigma^+$ state and has the largest magnitude of all 3 excitations shown, about twice as large as the X $^2\Pi$ - a $^4\Sigma^-$ excitation, which peak at about 2.5 and 1.5 $Å^2$. All 3 cross-sections approximately take the same form, an early peak just after their threshold followed by a steady decrease to level off at approximately 0.05 $Å^2$ by 20 eV. We also note that due to the relatively low ionisation energy of SiBr (about 4.5 eV), many of the enhancements shown in these cross-sections beyond that energy may be due to the appearance of pseudo-resonances in the calculation.

Figure 10.7 gives the reaction rate co-efficients for the SE and CC scattering models. The SE model gives values approximately 33% larger than the CC model, with a maximum of 6×10^{-6} cm^3/s compared to 4×10^{-6} cm^3/s at 2500 Kelvin. Beyond this peak

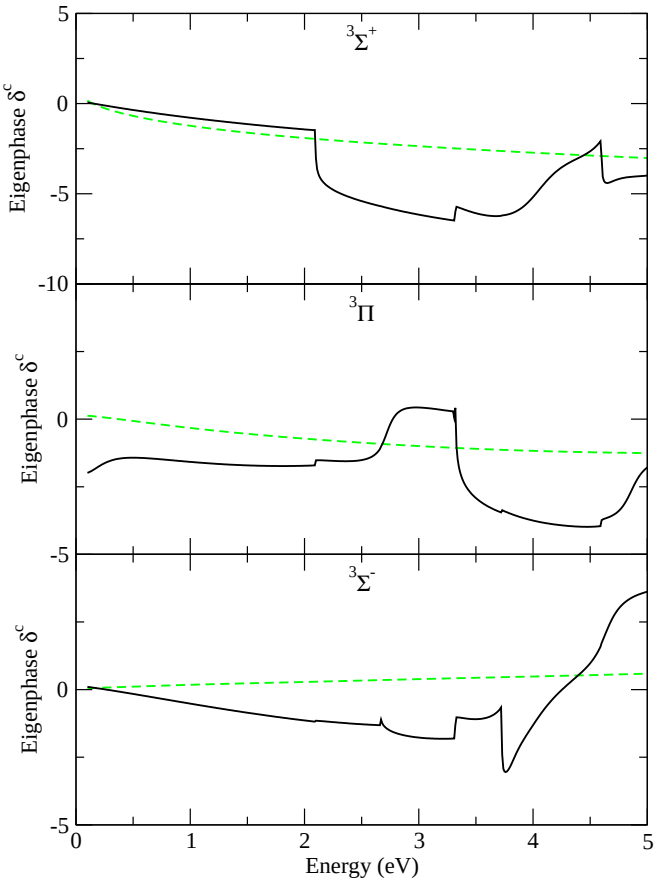

Figure 10.3: $SiBr^-$ triplet scattering eigenphases for the SE (dashed) and CC (solid) models.

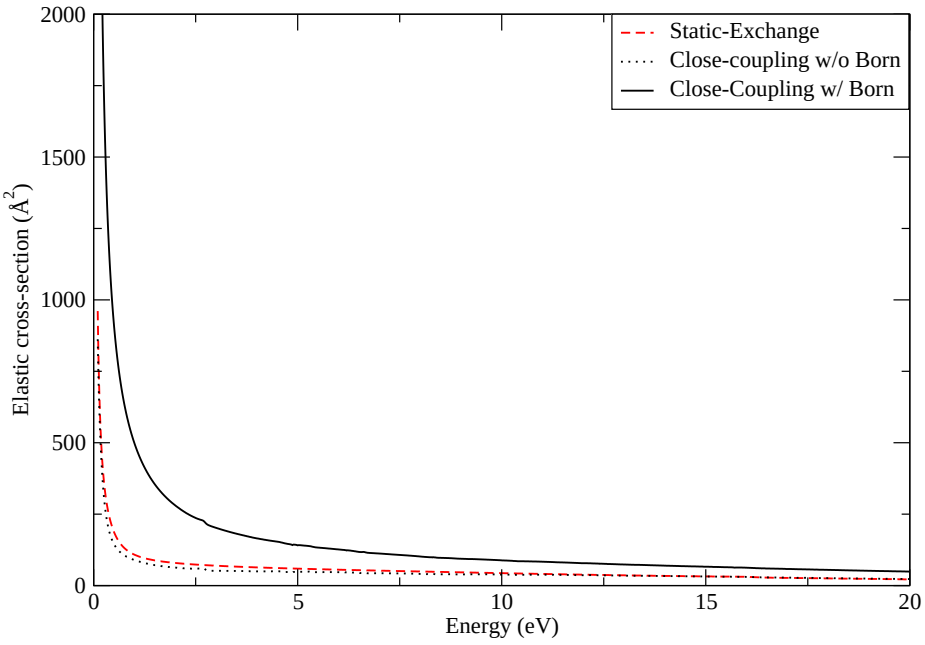

Figure 10.4: SiBr elastic cross-section

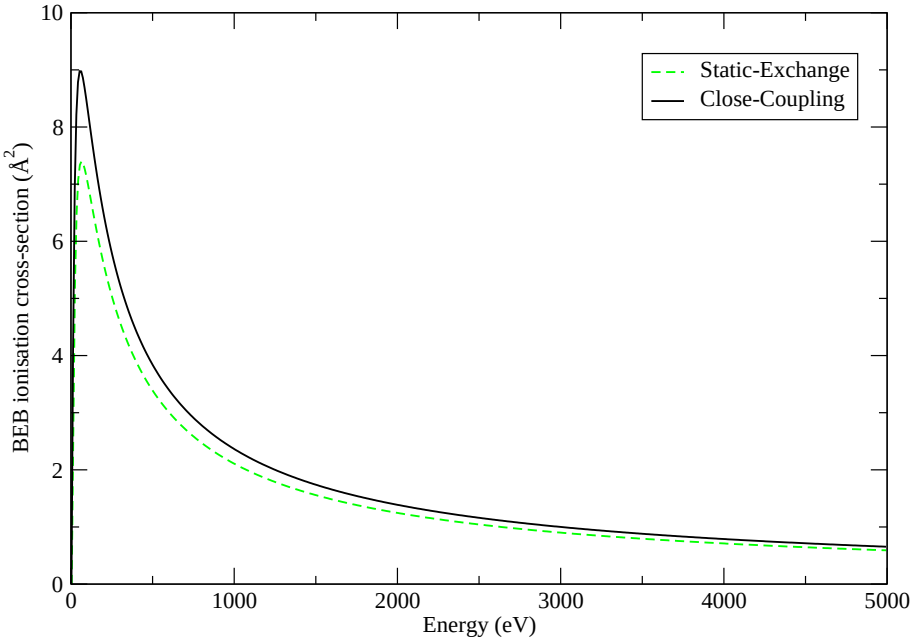

Figure 10.5: SiBr BEB ionisation cross-section

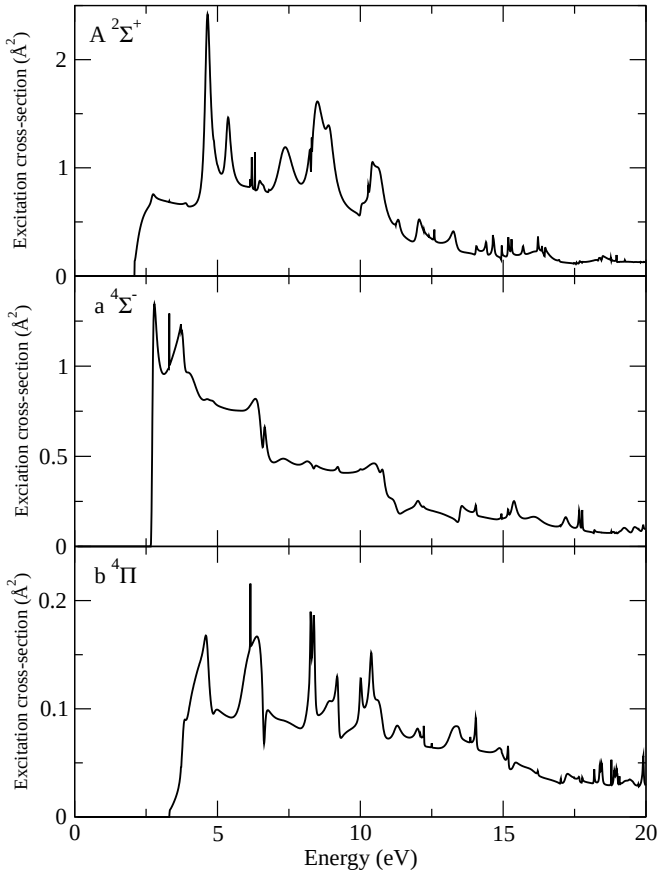

Figure 10.6: SiBr excitation cross-sections from the X $^2\Pi$ state to the A $^2\Sigma^+$, a $^4\Sigma^-$ and b $^4\Pi$ states.

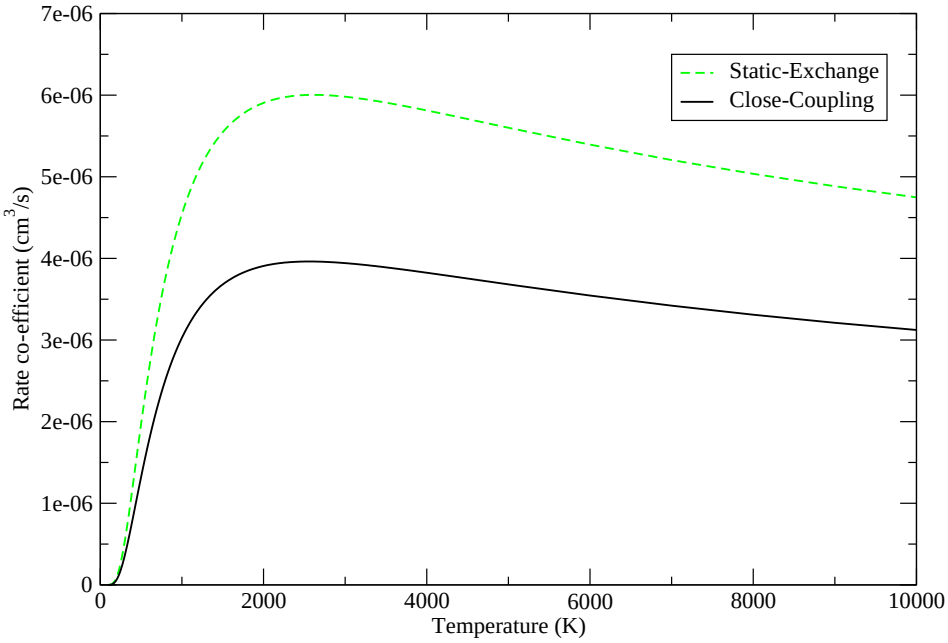

Figure 10.7: SiBr reaction rate co-efficients as a function of temperature.

temperature both models remain relatively stable to further increases, with the SE and CC models levelling off at 5×10^{-6} cm^3/s and 3×10^{-6} cm^3/s respectively by the end of the x-axis (10,000 Kelvin).

10.3 $SiBr_2$

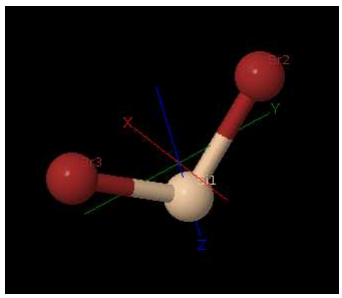

Figure 10.8: The molecule $SiBr_2$ (taken from Quantemol-N)

10.3.1 Calculation Details

Two calculations were carried out for $SiBr_2$, one using a Hartree-Fock target and static-exchange scattering model, the other using a configuration interaction target (allowing excitations from the ground state) followed by the close coupling scattering method.

Table 10.4: Geometry for $SiBr_2$

Atom	x	y	z
Si	0.0	0.0	1.204
Br	0.0	1.84	-0.212
Br	0.0	-1.84	-0.212

Table 10.5: $SiBr_2$ target calculation data.

Method	X $^1A_1$ (H)	μ (D)	a $^3B_1$ (eV)
HF	-5433.61	-2.28	
CI	-5433.62	-2.09	1.96
Coffin et al. (1989)	-5412.36		1.45

Both of these calculations were carried out using Quantemol-N (section 3.6). For these calculations the equilibrium geometry found in table 10.4 was used based upon the literature values, both experimental (Hargittai et al., 1983; Gershikov et al., 1990) and theoretical (Coffin et al., 1989), making use of the c_{2v} symmetry (however we note as this molecule is non-linear the B_1 and B_2 states are not degenerate). The ground state electron configuration for both HF and CI models being (1-17a_1 1-6b_1 1-14b_2 1-5a_2)[84]. For the CI calculation 62 electrons were frozen in the (1-12a_1 1-5b_1 1-10b_2 1-4a_2) orbitals, with the remaining 22 electrons in an active space of (13-18a_1 6-7b_1 11-14b_2 5a_2). An R-matrix radius of 13 a_0 was chosen to fully encompass the target wavefunction created using the 6-311G basis set.

10.3.2 Target Data

Both HF and CI models found a $^1A_1$ ground state, with the CI calculation 0.02 Hartree lower in energy, both of these calculations are better than the target energy found by Coffin et al. (1989). Both models used here also found similar ground states dipole moments of between 2.1-2.3 Debye in the direction of the bromine atoms. Table 10.5 summarises these results along with the comparison to the work of Coffin et al. (1989), table 10.6 gives the first three excited states from the CI model.

10.3.3 Scattering Results

For the scattering results we note that Koopman's theorem indicates an ionisation energy of 10.12 eV for $SiBr_2$, due to this we will only consider resonances up to 10 eV, as any above this will be pseudo-resonances. Figure 10.9 gives the scattering eigenphase sums

Table 10.6: $SiBr_2$ vertical excitation energies from the X $^1A_1$ state.

Excited state	Vertical exc. en. (eV)
a $^3B_1$	1.96
A $^1B_1$	3.40
b $^3A_2$	7.74

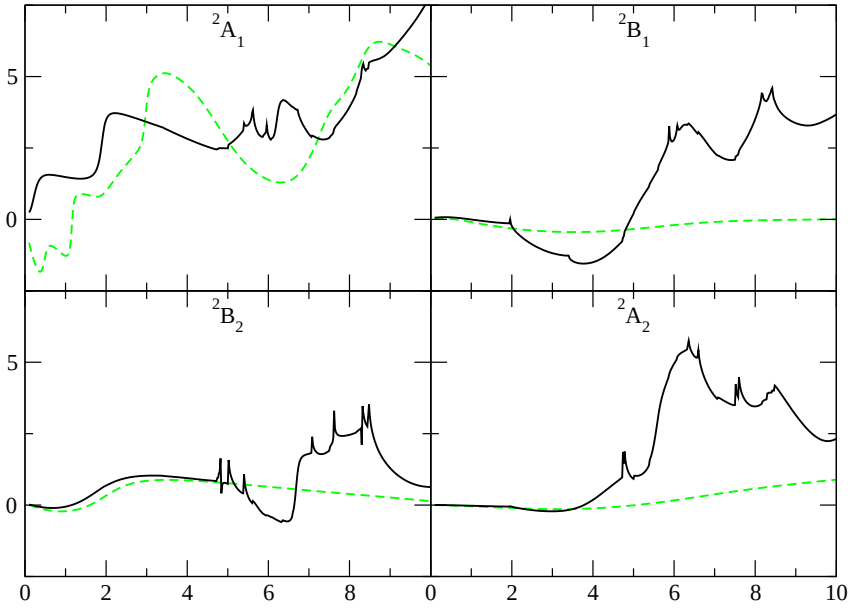

Figure 10.9: $SiBr_2^-$ doublet scattering eigenphases for the SE (dashed) and CC (solid) models.

for the electron-$SiBr_2$ collision for both the static-exchange and close-coupling models. The associated resonance data (up to 10 eV) can be found in table 10.7. Four $^2A_1$ shape resonances have been detected, appearing in both SE and CC models, with the SE resonances being slightly higher in energy and wider than the CC counterparts. We also find a narrow Feshbach $^2A_1$ resonance at 9.6 eV. In the $^2B_2$ symmetry a shape resonance has been detected in both SE and CC models at around 2 eV. Although in the CC model this was not automatically detected by RESON it is clearly present in the eigenphase sums, this model has also detected two narrow Feshbach resonances at 4.8 and 6.7 eV. For the $^2A_2$ symmetry a shape resonance has been detected in both models, again the SE model detecting it at higher energy and greater width than the CC model. The CC model has also detected a single Feshbach resonance at 4.3 eV of 1.5 eV width.

Figure 10.10 gives the elastic cross-section for the static-exchange and close-coupling scattering models, with a Born correction also applied to the CC model in order to correct and enhance the low-energy magnitude of the cross-section. This leads to the corrected cross-section being about twice as large as the uncorrected at an electron

Table 10.7: $SiBr_2$ resonance positions (and widths) in eV. [a] Resonance present in eigenphases but not fitted by RESON.

State	HF	CI
$^2A_1$	1.154 (0.082)	0.243 (0.221)
	2.973 (0.143)	1.897 (0.185)
	7.245 (0.675)	6.209 (0.151)
	8.165 (0.592)	6.9a
		9.612 (0.001)
$^2B_2$	2.045 (1.524)	1.8a
		4.828 (0.013)
		6.684 (0.117)
$^2A_2$		4.384 (1.526)
	7.606 (6.202)	5.569 (0.232)

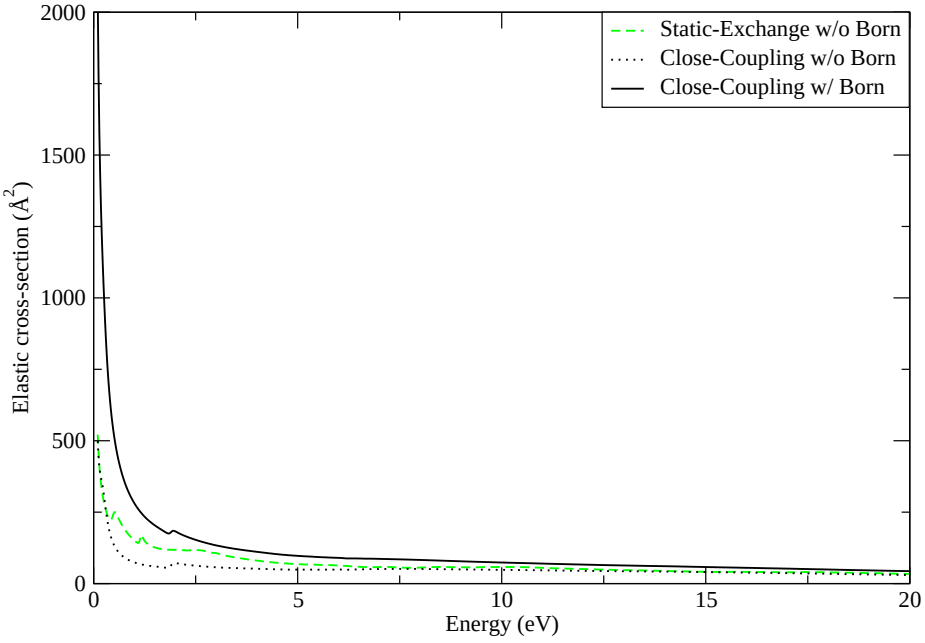

Figure 10.10: $SiBr_2$ elastic cross-section

energy of around 2.5 eV. All three variations level off at higher energies to about 50 Å^2. Figure 10.11 is the BEB ionisation cross-section up to 5000 eV, created using the BEB approximation from the orbital energies. This has an early peak of 3.5 Å^2 at 250 eV, before decreasing down to 0.75 Å^2 by 5000 eV.

Figure 10.12 presents the first three excitation cross-section from the X $^1A_1$ state. With a peak of 2.4 Å^2, the first excitation to the a $^3B_1$ state is twice as large as the next excitation (A $^1B_1$) and an order of magnitude greater than the third (b $^3A_2$). Both the a $^3B_1$ and A $^1B_1$ excitations have maximum peaks at around 4.5 eV and level off

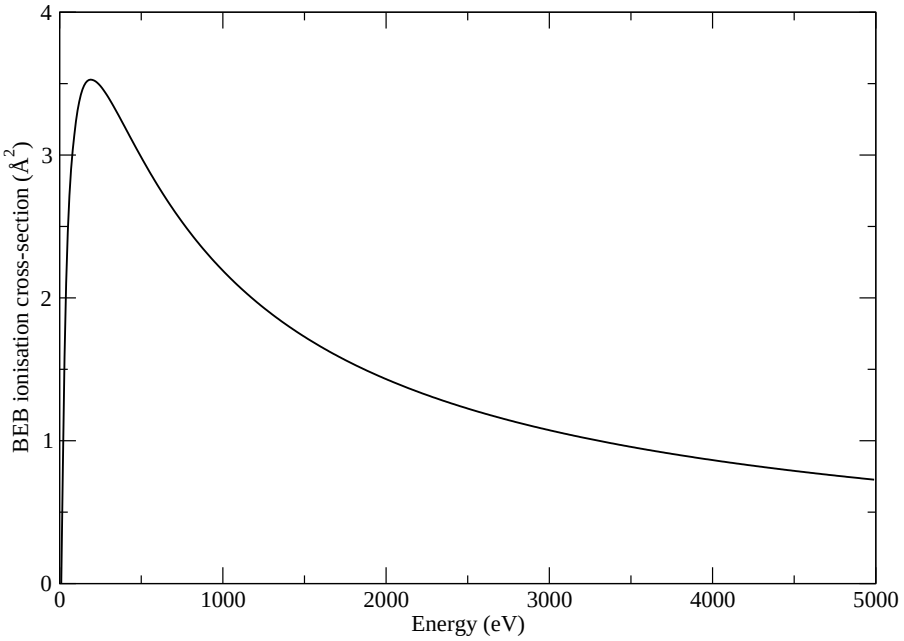

Figure 10.11: $SiBr_2$ BEB ionisation cross-section

to around 0.25 Å^2 at 20 eV. The b $^3A_2$ excitation is very sharply peaked at around 6 eV and levels off to 0.02 Å^2 by 20 eV. Figure 10.13 gives the high energy approximation of the excitation cross-section using the BEf method (Kim, 2001, 2007). This has only been calculated for the X $^1A_1$ - A $^1B_1$ excitation as this is the only dipole allowed of the three excitations considered, making use of the X $^1A_1$ - A $^1B_1$ dipole transition moment of -0.15 Debye, given by the target CI calculation. Compared to the same excitation cross-section as calculated by the R-matrix method, the BEf approximation peaks at 0.35 Å^2, about a quarter of the R-matrix cross-sections peak. However this approximation method is best used for high energies, and it is clear that as the energy approaches 1000 eV it levels off at around 2.5 Å^2, which is the same value obtained by the R-matrix excitation cross-section.

Figure 10.14 gives the reaction rate co-efficients for the SE and CC scattering models. The SE model gives values approximately 25% larger than the CC model, with a maximum of 2.75×10^{-6} cm^3/s compared to 2.2×10^{-6} cm^3/s at 2500 Kelvin. Beyond this peak temperature both models remain relatively stable to further increases, with the SE and CC models levelling off at 2.5×10^{-6} cm^3/s and 1.8×10^{-6} cm^3/s respectively.

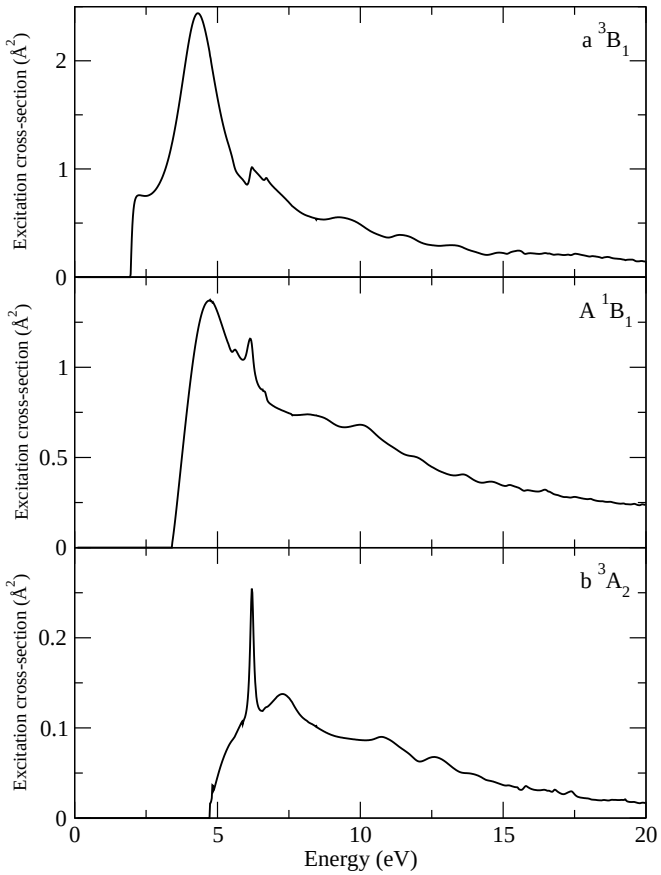

Figure 10.12: $SiBr_2$ excitation cross-sections from the X $^1A_1$ state to the a $^3B_1$, A $^1B_1$ and b $^3A_2$ states.

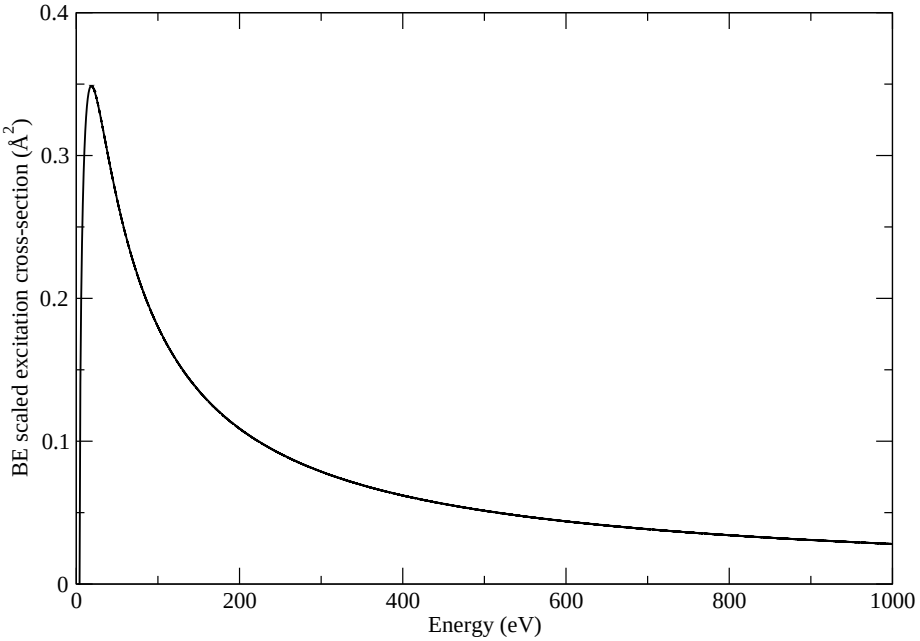

Figure 10.13: $SiBr_2$ scaled BEf excitation cross-section for the dipole allowed X $^1A_1$ - A $^1B_1$ transition.

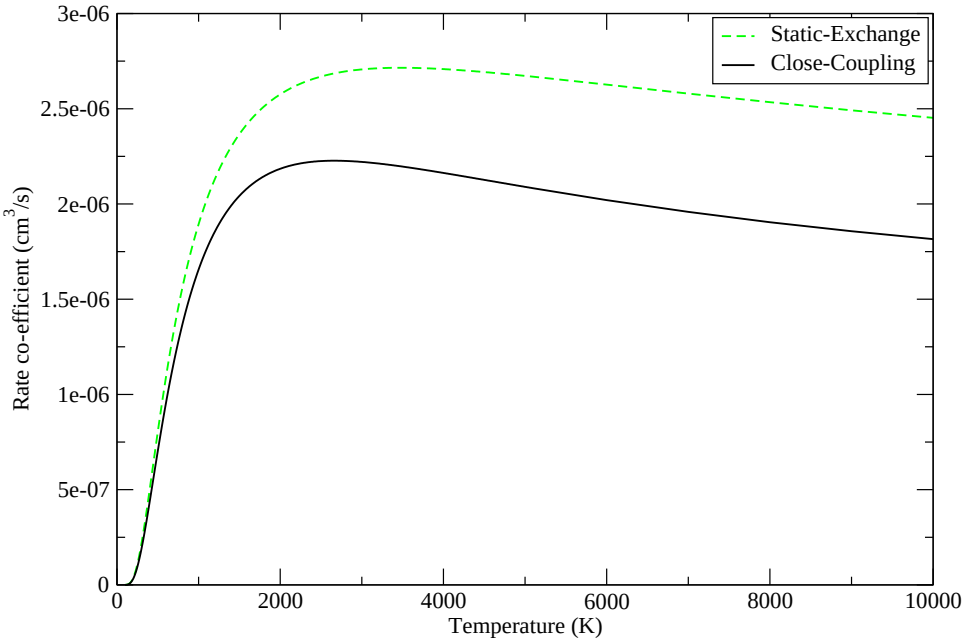

Figure 10.14: $SiBr_2$ reaction rate co-efficients for elastic electron scattering as a function of temperature.

10.4 Conclusions

The calculations in this chapter have been carried out due to the increasing need for electron-scattering data on species found within industrial plasmas. Since these calculations have taken place the data presented here has been used and applied to theoretical industrial plasma simulations, with successful results. As no previous electron scattering work had been carried out on these species these results are the first.

For SiBr two different models were applied, one using a Hartree-Fock target and static-exchange scattering model, and another using a configuration interaction target and close-coupling scattering model. Both models found there to be a ground state with an energy of around -2861 Hartree, although the HF target found a $^2\Sigma^+$ ground state whilst the CI model found one of $^2\Pi$. Similarly there was an increase in dipole moment from 3.51 to 4.14 Debye when going from the HF to CI models. No previous target data could be found for comparison. The CI model also found three low-lying excited states between 2.10 - 3.32 eV, of $^2\Sigma^+$, $^4\Sigma^-$ and $^4\Pi$ symmetries. The use of two different models also enabled us to check for Feshbach resonances, which will be present only in the CC scattering model. It was found there were 10 Feshbach resonances present under 10 eV, of various symmetries, no shape resonances were detected. These results can be clearly seen by comparison of the SE and CC model's eigenphase sums. The influence

of these resonances can be seen in the excitation cross-sections for SiBr, which show evidence of enhancement in the energy range of the resonance positions. Also presented are the total elastic and BEB ionisation cross-sections, and the reaction rate co-efficients as a function of temperature, for both the SE and CC scattering models. Whilst these models give similar results for the cross-sections in question, the addition of the Born correction to the total elastic cross-section increases the magnitude of it by around 100% at all energies (up to 20 eV).

For $SiBr_2$, again the two distinct models were used, both found there to be a $^1A_1$ ground state of -5433.6 Hartree, with a dipole moment of between 2.1 - 2.3 Debye. The ground state energy compared well to the other theoretical data found (-5412.36 Hartree). The CI model also found the first excited state to be of $^3B_1$ symmetry at 1.96 eV, again comparing well to the previous theoretical value of 1.45 eV. Furthermore the CI model also found two more low-lying excited states, at 3.40 ($^1B_1$) and 7.74 ($^3A_2$) eV respectively. After carrying out the scattering calculations, six shape and four Feshbach resonances were found in total, across various symmetries. Their influence can be seen in the excitation cross-sections as small increases in magnitude in the energy range associated with the resonance. Interestingly, from observation of the total elastic cross-section, we note that the SE model has a greater magnitude than the CC model at low energies. However, as previously, the application of the Born correction enhances this by approximately 100% at lower energies, the result of this being that both the SiBr and $SiBr_2$ total elastic cross-sections are very similar once the Born correction has been applied. The same is not true of the BEB ionisation cross-section, which is around 50% smaller for $SiBr_2$ than for SiBr, whilst sharing a similar shape. Also included in this set of data is the BEf cross-section for the dipole allowed X $^1A_1$ - A $^1B_1$ excitation, at low energies the maximum value of this cross-section is around 33% of the same excitation cross-section calculated using the R-matrix method. However, BEf is an approximation method designed to extend excitation cross-sections to much higher energies, so both are useful as data for distinct energy ranges.

Chapter 11

Conclusion

Within this thesis a number of electron-scattering interactions have been analysed, these range from astrophysical hydrocarbons (CN, C_3N, C_2H), to molecules of plasma interest (NaI, SiBr, $SiBr_2$), and atoms (O). The majority of these calculations were restricted to low-energy (i.e. below ionisation energy) electron-scattering, particularly for the astrophysical molecules as these low energy electrons reflect the environmental temperature of the interstellar medium. However use of approximation methods allow some scattering observables to be extended to much higher energies than the R-matrix calculations are capable of (e.g. BEB ionisation and BEf excitation cross-sections). For each of these calculations the K-,T- and R-matrices, the eigenphase sums, resonance parameters, elastic, inelastic, BEB and BEf cross-sections were all calculated.

This thesis also includes the development of a theory used for calculating spin-coupled rotational cross-sections. This has been developed from the work of Corey and McCourt (1983) and describes how the spin-coupled cross-sections may be obtained from the manipulation of the non-coupled ones (which themselves can be computed from T-matrices). This has led to the development of a new FORTRAN program for carrying this out, ROTLIN_S. Example data has been included as a validation of the code and to provide the first spin-coupled rotational cross-sections for the molecule CN, intended for further use in astrophysical modelling.

Finally within the thesis is detailed the first known complete calculation using the UK Molecular R-Matrix codes to carry out electron-atom scattering (in this case, oxygen). A number of problems were encountered that were particular to carrying out an electron-atom calculation, such as dealing with the spherical symmetry of an atom in the D_{2h} symmetry of the molecular codes. These have been detailed, along with solutions to each,

in the oxygen section (chapter 8). I feel as a proof of concept for running electron-atom scattering using these codes, this work was successful.

None of the electron-scattering calculations carried out in this thesis had previously been undertaken, either theoretically or experimentally, so all data presented here can be considered new. In the case of CN, C_2H, C_3N, $SiBr_2$ and O, some previous quantum chemistry data was found outlining the energetics of the various target states (also dipole moments and bound states in the case of CN, C_2H, and C_3N). Here the calculations were found to be in good agreement with the existing data. For the CN spin-coupled rotational cross-sections (sec 5.7), the data presented has been compared to the findings of Allison and Dalgarno (1971). In certain energy ranges the results differ significantly, showing the importance of the more complete R-matrix treatment we have carried out, more complete analysis is available in chapter 5.

Whilst a through analysis of results are presented in each chapter, here is now presented a brief outline of the results found for each study.

Chapter 5 details e-CN scattering for a number of combinations of orbital type and scattering methods. Particular attention was taken to the first 2 excitations as these are the cause of the well-known 'CN red' and 'CN violet' spectral bands, it was found the Born correction greatly enhances these cross-sections. A number of resonances were found in the triplet eigenphase sums, notably a $^3\Pi$ shape resonance at 3 eV which manifested itself across all 5 models, both static exchange and close-coupling. There are also Feshbach resonances detected for the $^3\Sigma^+$ and $^3\Sigma^-$ symmetries at approximately 4.5 and 5 eV respectively (depending on model). The fact no singlet resonances detected lead us to believe that the excited states of CN^- detected by Musial (2005) (which are all singlet) are false artefacts. As a further development an analysis of target and scattering properties as a function of bond length was undertaken, it was found that the resonances become lower in position and narrower in width as the bond length increases. The spin-rotational cross-sections were also calculated for various transitions, as discussed above some of these can be compared to the results of Allison and Dalgarno (1971). As a further extension to this, the cross-sections could now be utilised to produce reaction rates for the various electronically excited spin-rotation transitions. These would be extremely useful to the astrophysical community. In order to do this the outer region of the original CN R-matrix calculation would likely need to be re-done with a finer energy grid to fully resolve the data at the smallest electron energies (thus reflecting the low

temperatures of the ISM).

Chapters 6 and 7 present the calculations for e-C_3N and e-C_2H, these may be considered together as one investigation into how molecular anions may form in the interstellar medium. General consensus is that they form by radiative attachment of an electron to the neutral molecule with the same chemical formula (Millar et al., 2007). These chapters investigate whether this is possible. It is found that C_3N has a number of very weakly bound states (< 1 eV), whilst C_2H does not. There is a mechanism possible whereby very weakly bound states will support nuclear excited states which lie in the continuum and therefore are resonances. If this mechanism does explain the formation of such anions in the ISM, then the likelihood is C_3N^- would be much more abundant than C_2H^-, which currently matches the observations.

Chapter 8 outlines the method and problems of running an e-atom calculation using the UK molecular R-matrix codes. This was carried out in order to theoretically replicate the ^{3}P-^{3}P experimental cross-section of Katsch et al. (2000), requested by a Quantemol customer. This method was proven successful as the resulting theoretical cross-section matched the experimental data well. Whilst other data was calculated in this investigation, this excitation was the main focus and as such the quality of the calculation as a whole is based solely on this result. If we were to be critical of this calculation, I feel further attention could be made into investigating the effect manually changing the energy levels has as the calculation progresses to the outer region. In this work it is found that the eigenphase sums of the scattering states which should be degenerate are no longer after shifts are applied.

Chapter 9 shows the results of the first known e-NaI scattering calculation. Whilst only one model was considered and there is very little data on NaI with which to compare, a ground state dipole moment of 10.05 Debye was found, which matches nicely with the work of Sakai et al. (1992) and Hebert et al. (1968). Furthermore it was found that the first three excited states all lie very closely to each other, between 4.1 - 4.5 eV. The associated excitation cross-sections found present very similar forms, however the dipole allowed transition to the second excited state, A $^1\Pi$, was found to be approximately twice as large as the dipole forbidden transitions to the first (a $^3\Pi$) and third (b $^3\Sigma^+$) excited states. It is also worth noting that due to the very large dipole moment of the target molecule, the elastic cross-section was greatly enhanced by the Born correction, with there being up to two orders of magnitude difference at 10 eV (approx 10 c.f. 1000

Å^2) and at least an order of magnitude difference even at 100 eV (approx 5 c.f. 100 Å^2).

Finally Chapter 10 contains the results of investigations into both e-SiBr and e-$SiBr_2$ systems. Static-exchange and close-coupling scattering methods were employed for both molecules to search for shape and Feshbach resonances. SiBr was found to have no shape resonances at all below the ionisation threshold of 4.5 eV, however there are a number of Feshbach resonances of $^1\Sigma^+$, $^1\Pi$, $^1\Sigma^-$, $^1\Delta$, $^3\Pi$ and $^3\Delta$ symmetries. There is no data at all to compare the SiBr results to, however some target data for $SiBr_2$ was found (Coffin et al., 1989). Here it was found that both the HF and CI target calculations from this work produced better ground state energies by 21 Hartree, however the calculated X $^1A_1$ - a $^3B_1$ excitation energy was 0.5 eV higher. This potentially could be due to the method employed in this work improving the ground state energy but not the excited state energy, hence the vertical excitation energy is greater. The ionisation threshold for $SiBr_2$ is 10.1 eV, below which a number of shape resonances were found (four $^2A_1$, one $^2B_2$ and one $^2A_2$). Also Feshbach resonances were detected in the $^2A_1$, $^2B_2$ (two) and $^2A_2$ symmetries.

The R-matrix software Quantemol-N (Tennyson et al., 2007) was used at some stage in every calculation carried out in this work. Either to provide models for comparison with the final results (CN, C_3N, C_2H), job files for adaptation in the manual running of the R-matrix codes (O), or to provide the final sets of data (NaI, SiBr, $SiBr_2$). For over 5 years this program has been used as a tool for enabling non-experts to carry out R-matrix calculations, and over the course of this work has developed in ability and flexibility. Some of the newest features to be added to the software include the ability to calculate cross-sections for molecules of a particular fixed orientation, calculation of differential and momentum transfer cross-sections, and calculation of rotational excitation cross-sections.

The R-matrix codes themselves have also undergone a recent improvement (section 3.4) and are being continually developed. The majority of this work now lies in the outer region, where new functionality can be added in modularised form or small, standalone programs separate from the R-matrix codes themselves but which utilise the T-matrices produced. An example of this is the new code presented in chapter 4, the ROTLIN_S code enables spin-coupled rotational cross-sections to be computed from input T-matrices from the R-matrix codes. Note that in order to do this they have been converted into the correct irreducible symmetry using the KMATAD module, an example of these

transformations can be found in table 3.1.

The very fact that no previous electron-scattering data could be found for any of the species in this work is a stark reminder of how much is still unknown about the behaviour of both interstellar and industrial plasmas. The findings and conclusions drawn from both the work on C_2H and C_3N suggest that the current theories on carbon chain formation in the ISM (Millar et al., 2007) are heading in the right direction, as this work provides a potential explanation to match observations (Gupta et al., 2007; Thaddeus et al., 2008; Agundez et al., 2010). However more work is required on other relevant species e.g. C_4H, C_6H etc (it should be noted that there are inherent difficulties in working with C_4H theoretically (Fortenberry et al., 2010)). What we can conclude however is that electron-molecule interactions play a crucial role in interstellar plasmas. In order to fully understand the chemistry of these environments there is a need to complete the catalogue of mechanisms and interactions which are possible, this must be done in conjunction with observation as only then will the true nature of these plasmas will become apparent. This becomes even more important now that these species are starting to be observed in planetary atmospheres (Vuitton et al., 2009).

There is also an increasing demand within the industrial plasma community to understand the true mechanics that occur within a reactor. Traditionally the onus has been placed on machine output (i.e. silicon chip yield), with the physics of the plasma itself being of secondary importance. However as manufacturers strive for efficiency and effectiveness in their machines there comes a need to go beyond the varying of simple inputs such as power or gas flow. A true understanding of the electron-molecule chemistry is needed to produce the best output yield in the most cost-effective way. Quantemol have worked in partnership with global industrial plasma manufacturers on such investigations and it has been found that previously unconsidered interactions have had a profound effect on the plasma, where internal processes such as etching can produce a great number of ions and radicals (e.g. Kimura et al. (2001)). The work presented here on NaI, SiBr and $SiBr_2$ has shown these electron-heavy species have many resonances which result from electron-scattering interactions. These resonances all aid and enhance the electron-collision cross-sections, thus meaning that these species can have a substantial effect on the electrons that exist within the plasma.

Appendix A

Non-Hermiticity of the Hamiltonian: A Potential Scattering Example

This appendix has been taken and used with full permission courtesy of Hemal N. Varambhia.

Let the wavefunction of an enclosed system $\psi_i = f_i(r)Y_{l_i}^{m_i}(\theta,\phi)$. Evaluating the Hamiltonian matrix element $\langle\psi_j|\hat{H}\psi_i\rangle - \langle\hat{H}\psi_j|\psi_i\rangle$ over the interval containing the internal region yields:

$$M = -\frac{1}{2}[\langle\psi_j|\nabla^2\psi_i\rangle - \langle\nabla^2\psi_j|\psi_i\rangle] \tag{A.1}$$

(the potential matrix elements are assumed to be Hermitian and vanish). Thus the braket simplifies to a radial integral below

$$M = -\frac{1}{2}\left\{\int_0^a r^2 dr f_j^* \frac{1}{r^2}\frac{d}{dr}\left(r^2\frac{df_i}{dr}\right) - \int_0^a r^2 dr\left[\frac{1}{r^2}\frac{d}{dr}\left(r^2\frac{df_j}{dr}\right)\right]^* f_i\right\} \tag{A.2}$$

$$\tag{A.3}$$

Simplifying notation:

$$M = -\frac{1}{2}(I_1 - I_2) \tag{A.4}$$

$$I_1 = \int_0^a f_j^*\frac{d}{dr}\left(r^2\frac{df_i}{dr}\right)dr \tag{A.5}$$

$$I_2 = \int_0^a \frac{d}{dr}\left(r^2\frac{df_j^*}{dr}\right)f_i dr \tag{A.6}$$

We shall evaluate the integrals I_1 and I_2 using integration by parts where for I_1:

$$v = f_j^* \tag{A.7}$$
$$\frac{du}{dr} = \frac{d}{dr}\left(r^2 \frac{df_i}{dr}\right) \tag{A.8}$$

and for I_2

$$v = f_i \tag{A.9}$$
$$\frac{du}{dr} = \frac{d}{dr}\left(r^2 \frac{df_j^*}{dr}\right) \tag{A.10}$$

Upon evaluation of these integrals, one obtains non-zero surface terms resulting in the Hamiltonian not being Hermitian.

$$M = -\frac{a^2}{2}(f_j(a)^* f_i'(a) - f_j'(a)^* f_i(a)) \neq 0 \tag{A.11}$$

Define the Bloch operator and the modified Hamiltonian:

$$\hat{L} = \frac{1}{2a}\delta(r-a)\frac{d}{dr}r \tag{A.12}$$
$$\hat{\mathcal{H}} = \hat{H} + \hat{L} \tag{A.13}$$

Computing the modified Hamiltonian matrix elements over the same interval

$$-\frac{1}{2}\langle\psi_j|\nabla^2\psi_i\rangle + \langle\psi_j|\hat{L}\psi_i\rangle - \frac{1}{2}\langle\nabla^2\psi_j|\psi_i\rangle - \langle\hat{L}\psi_j|\psi_i\rangle \tag{A.14}$$

it may be shown that evaluating those matrix elements involving the Bloch operator simplify to

$$\frac{1}{2a}\left\{a^2\left[f_j(a)^*\frac{d}{dr}[rf_i(r)]_a - \frac{d}{dr}[rf_j(r)^*]_a f_i(a)\right]\right\} \tag{A.15}$$

Finally appealing to the product rule equation (A.15) may be shown to cancel the kinetic energy surface term (A.11), and Hermicity is regained. Discussion on the above problem may be found in Lane and Robson (1966).

Appendix B

The Outer Region Coupled Differential Equations

This appendix has been taken and used with full permission courtesy of Hemal N. Varambhia.

B.1 Derivation

Considering

$$\hat{H}_{N+1}|\Psi^{\Delta}\rangle = E|\Psi^{\Delta}\rangle \tag{B.1}$$

one may decompose this Schrödinger equation to

$$-\frac{1}{2}\nabla^2_{N+1}\Psi^{\Delta} + \left\{-\sum_A \frac{Z_A}{|\mathbf{r}_{N+1}-\mathbf{r}_A|} + \sum_i \frac{1}{|\mathbf{r}_{N+1}-\mathbf{r}_i|}\right\}\Psi^{\Delta} + \hat{H}_N\Psi^{\Delta} = E\Psi^{\Delta} \tag{B.2}$$

Let

$$\hat{V}_1 = -\sum_A \frac{Z_A}{|\mathbf{r}_{N+1}-\mathbf{r}_A|} \tag{B.3}$$

$$\hat{V}_2 = \sum_i \frac{1}{|\mathbf{r}_{N+1}-\mathbf{r}_i|} \tag{B.4}$$

In the outer region one may employ the single centre expansion:

$$\Psi^{\Delta} = \sum_{\lambda} \frac{F^{\Delta}_{\lambda}}{r_{N+1}} \psi^N_{\lambda} Y^{m_\lambda}_{l_\lambda} \tag{B.5}$$

In evaluating the kinetic energy term of equation (B.2)

$$\nabla^2\Psi^{\Delta} = \sum_{\lambda}\left[F_{\lambda}^{\Delta\prime\prime} - \frac{l_\lambda(l_\lambda+1)}{r_{N+1}^2}F_{\lambda}^{\Delta}\right]\frac{\psi_\lambda^N Y_{l_\lambda}^{m_\lambda}}{r_{N+1}} \tag{B.6}$$

Further manipulation of equation (B.2) and substituting equation (B.6) the coupled differential equations become:

$$\sum_{\lambda}\left\{F_{\lambda}^{\Delta\prime\prime} - \frac{l_\lambda(l_\lambda+1)F_{\lambda}^{\Delta}}{r_{N+1}^2} + 2(E-E_\lambda)F_{\lambda}^{\Delta}\right\}\psi_\lambda^N Y_{l_\lambda}^{m_\lambda} = 2\sum_{\lambda}\hat{V}F_{\lambda}^{\Delta}\psi_\lambda^N Y_{l_\lambda}^{m_\lambda} \tag{B.7}$$

where

$$\hat{V} = \hat{V}_1 + \hat{V}_2 \tag{B.8}$$

$$\hat{V} = -\sum_{A}\frac{Z_A}{|\mathbf{r}_{N+1}-\mathbf{r}_A|} + \sum_{i}\frac{1}{|\mathbf{r}_{N+1}-\mathbf{r}_i|} \tag{B.9}$$

and projecting on to $\psi_{\lambda'}^N Y_{l_{\lambda'}}^{m_{\lambda'}}$

$$F_{\lambda'}^{\Delta\prime\prime} - \frac{l_{\lambda'}(l_{\lambda'}+1)F_{\lambda'}^{\Delta}}{r_{N+1}^2} + 2(E-E_{\lambda'})F_{\lambda'}^{\Delta} = 2\sum_{\lambda}V_{\lambda'\lambda}F_{\lambda}^{\Delta} \tag{B.10}$$

where

$$V_{\lambda'\lambda} = \langle\psi_{\lambda'}^N Y_{l_{\lambda'}}^{m_{\lambda'}}|\hat{V}|\psi_\lambda^N Y_{l_\lambda}^{m_\lambda}\rangle \tag{B.11}$$

B.2 The Channel Coupling Potential

In the outer region the position vector of the scattering electron is greater than those of the target electrons and the constituent nuclei. Therefore one may appeal to the Legendre generating function and the spherical harmonic addition theorem to show that:

$$\sum_{i}\frac{1}{|\mathbf{r}_{N+1}-\mathbf{r}_i|} = \sum_{l}\sum_{m=-l}^{l}\frac{1}{r_{N+1}^{l+1}}\sum_{i}R_l^m(\mathbf{r}_i)Y_l^m(\theta_{N+1},\phi_{N+1}) \tag{B.12}$$

where

$$R_l^m(\mathbf{r}_i) = \frac{4\pi}{2l+1}{r_i}^l Y_l^m(\theta_i,\phi_i) \tag{B.13}$$

Furthermore, define

$$V^1_{\lambda'\lambda} = \langle \psi^N_{\lambda'} Y^{m_{\lambda'}}_{l_{\lambda'}} | \hat{V}_1 | \psi^N_{\lambda} Y^{m_{\lambda}}_{l_{\lambda}} \rangle \tag{B.14}$$

$$V^2_{\lambda'\lambda} = \langle \psi^N_{\lambda'} Y^{m_{\lambda'}}_{l_{\lambda'}} | \hat{V}_2 | \psi^N_{\lambda} Y^{m_{\lambda}}_{l_{\lambda}} \rangle \tag{B.15}$$

Computing $\langle \psi^N_{\lambda'} Y^{m_{\lambda'}}_{l_{\lambda'}} | \hat{V}_2 | \psi^N_{\lambda} Y^{m_{\lambda}}_{l_{\lambda}} \rangle$ to begin with, we then obtain

$$V^2_{\lambda'\lambda} = \sum_l \sum_{m=-l}^{l} \frac{(-1)^{m_{\lambda'}}}{r^{l+1}_{N+1}} M^m_l(\lambda' \to \lambda) C(l_{\lambda'}, l, l_{\lambda}) \begin{pmatrix} l_{\lambda'} & l & l_{\lambda} \\ -m_{\lambda'} & m & m_{\lambda} \end{pmatrix} \begin{pmatrix} l_{\lambda'} & l & l_{\lambda} \\ 0 & 0 & 0 \end{pmatrix} \tag{B.16}$$

where

$$M^m_l(\lambda' \to \lambda) = \langle \psi^N_{\lambda'} Y^{m_{\lambda'}}_{l_{\lambda'}} | \sum_i R^m_l(\mathbf{r}_i) | \psi^N_{\lambda} Y^{m_{\lambda}}_{l_{\lambda}} \rangle \tag{B.17}$$

Let us define

$$b_{l,\lambda'\lambda} = \sum_{m=-l}^{l} (-1)^{m_{\lambda'}+1} \left[-M^m_l(\lambda' \to \lambda) \right] C(l_{\lambda'}, l, l_{\lambda}) \begin{pmatrix} l_{\lambda'} & l & l_{\lambda} \\ -m_{\lambda'} & m & m_{\lambda} \end{pmatrix} \begin{pmatrix} l_{\lambda'} & l & l_{\lambda} \\ 0 & 0 & 0 \end{pmatrix} \tag{B.18}$$

In a similar fashion to the above, we can show that:

$$V^1_{\lambda'\lambda} = \sum_l \sum_{m=-l}^{l} \sum_A \frac{Z_A R^m_l(\mathbf{R}_A)(-1)^{m_{\lambda'}+1}}{r^{l+1}_{N+1}} \delta_{\lambda\lambda'} C(l_{\lambda'}, l, l_{\lambda}) \begin{pmatrix} l_{\lambda'} & l & l_{\lambda} \\ -m_{\lambda'} & m & m_{\lambda} \end{pmatrix} \begin{pmatrix} l_{\lambda'} & l & l_{\lambda} \\ 0 & 0 & 0 \end{pmatrix} \tag{B.19}$$

Again we let

$$c_{l,\lambda'\lambda} = \sum_{m=-l}^{l} \sum_A Z_A R^m_l(\mathbf{R}_A)(-1)^{m_{\lambda'}+1} \delta_{\lambda\lambda'} C(l_{\lambda'}, l, l_{\lambda}) \begin{pmatrix} l_{\lambda'} & l & l_{\lambda} \\ -m_{\lambda'} & m & m_{\lambda} \end{pmatrix} \begin{pmatrix} l_{\lambda'} & l & l_{\lambda} \\ 0 & 0 & 0 \end{pmatrix} \tag{B.20}$$

Hence if we let $a_{l,\lambda'\lambda} = b_{l,\lambda'\lambda} + c_{l,\lambda'\lambda}$ then

$$\langle \psi^N_{\lambda'} Y^{m_{\lambda'}}_{l_{\lambda'}} | \hat{V} | \psi^N_{\lambda} Y^{m_{\lambda}}_{l_{\lambda}} \rangle = \sum_l \frac{a_{l,\lambda'\lambda}}{r^{l+1}_{N+1}} \tag{B.21}$$

where

$$C(l_{\lambda'}, l, l_{\lambda}) = \sqrt{\frac{(2l_{\lambda'}+1)(2l+1)(2l_{\lambda}+1)}{4\pi}} \tag{B.22}$$

$$a_{l,\lambda'\lambda} = \sum_{m=-l}^{l} \mu_l^m(\lambda' \to \lambda)(-1)^{m_{\lambda'}+1} C(l_{\lambda'}, l, l_\lambda) \begin{pmatrix} l_{\lambda'} & l & l_\lambda \\ -m_{\lambda'} & m & m_\lambda \end{pmatrix} \begin{pmatrix} l_{\lambda'} & l & l_\lambda \\ 0 & 0 & 0 \end{pmatrix} \tag{B.23}$$

and the molecular multipole moments

$$\mu_l^m(\lambda' \to \lambda) = -M_l^m(\lambda' \to \lambda) + \sum_A Z_A R_l^m(\mathbf{R}_A)\delta_{\lambda\lambda'} \tag{B.24}$$

Appendix C

Publications

Bound and continuum states of molecular anions C_2H^- and C_3N^-

S. Harrison and J. Tennyson

J. Phys. B: At. Mol. Opt. Phys., **44**, 045206 (7 pages) (2011)

Electron collisions with the CN radical: bound states and resonances

S. Harrison and J. Tennyson

J. Phys. B: At. Mol. Opt. Phys., **45**, 035204 (7 pages) (2012)

A dissociative electron attachment cross-section estimator

J.J. Munro, S. Harrison, J. Tennyson and M.M. Fujimoto

J. Phys. Conf. Series, (in press)

Calculated electron impact spin-coupled rotational cross sections for $^{2S+1}\Sigma^+$ linear molecules: CN as an example

S. Harrison, J. Tennyson and A. Faure

J. Phys. B: At. Mol. Opt. Phys., **45**, 175202 (9 pages) (2012)

Bibliography

Agundez M, Cernicharo J, Guelin M, Kahane C, Roueff E, Klos J, Aoiz F J, Lique F, Marcelino N, Goicoechea J R, Garcia M G, Gottlieb C A, McCarthy M C and Thaddeus P 2010 *Astron. Astrophys. Lett.* **517**, L2.

Ahearn M F, Millis R L, Schleicher D G, Osip D J and Birch P V 1995 *Icarus* **118**, 223–270.

Ajitha D and Hirao K 2001 *Chem. Phys. Letters* **347**, 121–126.

Alexander M H, Smedley J E and Corey G C 1986 *J. Chem. Phys.* **84**, 3049–3058.

Allison A C and Dalgarno A 1971 *Astron. Astrophys.* **13**, 331–332.

Almlof J and Taylor P R 1984 'Advanced Theories and Computational Approaches to the Electronic Structure of Molecules'.

Baker J, Nobes R H and Radom L 1986 *J. Comp. Chem.* **7**, 349–358.

Baluja K L, Burke P G and Morgan L A 1982 *Computer Phys. Communs.* **27**, 299–307.

Baluja K L, Mason N J, Morgan L A and Tennyson J 2000 *J. Phys. B: At. Mol. Opt. Phys.* **33**, L677–L684.

Baluja K L, Mason N J, Morgan L A and Tennyson J 2001 *J. Phys. B: At. Mol. Opt. Phys.* **34**, 2807–2821.

Bell K L and Hibbert A 1990 *J. Phys. B: At. Mol. Opt. Phys.* **23**, 2673–2685.

Beloy K, Borschevsky A, Schwerdtfeger P and Flambaum V V 2010 *Phys. Rev. A* **82**, 022106–1–022106–7.

Berente I, Szalay P G and Gauss J 2002 *J. Chem. Phys.* **117**, 7872–7881.

Berkowitz J, Chupka W A and Walter T A 1969 *J. Chem. Phys.* **50**, 1497–1500.

Booth J P, Joubert O and Pelletier J 1991 *J. Appl. Phys.* **69**, 618–626.

Bossier G, Bredohl H and Dubois I 1984 *J. Mol. Spec.* **106**, 72–76.

Botschwina P and Oswald R 2008 *J. Chem. Phys.* **129**, 044305.

Bouchiha D, Caron L G, Gorfinkiel J D and Sanche L 2008 *J. Phys. B: At. Mol. Opt. Phys.* **41**, 045204.

Boys S F 1950 *Proc. Roy. Soc. A* **200**, 542–544.

Bradforth S E, Kim E H, Arnold D W and Neumark D M 1993 *J. Chem. Phys.* **15**, 800–810.

Breit G and Wigner E 1936 *Phys. Rev.* **49**, 519–531.

Broadfoot A L, Belton M J S, Takacs P Z, Sandel B R, Shemansky D E, Holberg J B, Ajello J M, Atreya S K, Donahue T M, Moos H W, Bertaux J L, Blamont J E, Strobel D F, McConnell J C, Dalgarno A, Goody R and McElroy M B 1979 *Science* **204**, 979–982.

Broadfoot A L, Sandel B R, Shemansky D E, Holberg J B, Smith G R, Strobel D F, McConnell J C, Kumar S, unten D M, Atreya S K, Donahue T M, Moos H W, Bertaux J L, Blamont J E, Pomphrey R B and Linick S 1981 *Science* **212**, 206–211.

Brown J M, Hougen J T, Huber K P, Johns J W C, Kopp I, Lefebvre-Brion H, Merer A J, Ramsay D A, Rostas J and Zare R N 1975 *J. Molec. Spectrosc.* **55**, 500 – 503.

Brunger M J and Buckman S J 2002 *Physics Reports* **357**, 215–458.

Brunken S, Gupta H, Gottlieb C A, McCarthy M C and Thaddeus P 2007 *Astrophys. J.* **664**, L43–L46.

Burke P G 1973 *Computer Phys. Communs.* **6**, 288–302.

Burke P G, Hibbert A and Robb W D 1971 *J. Phys. B: At. Mol. Opt. Phys.* **4**, 153–161.

Burke P G, Mackey I and Shimamura I 1977 *J. Phys. B: At. Mol. Opt. Phys.* **10**, 2497–2512.

Burke P G, Noble C J and Burke V M 2007 *Adv. Atom. Mol. Opt. Phys.* **54**, 237–318.

Burke P G, Noble C J and Scott P 1987 *Proc. R. Soc. Lond.* **410**, 289–310.

Burke P G and Seaton M J 1971 *Methods Comput. Phys.* **10**, 1–80.

Bus S J, Ahearn M F, Schleicher D G and Bowell E 1991 *Science* **251**, 774–777.

Caprasecca S, Gorfinkiel J D, Bouchiha D and Caron L G 2009 *J. Phys. B: At. Mol. Opt. Phys.* **42**, 095205.

Carr J M, Galiatsatos P G, Gorfinkiel J D, Harvey A G, Lysaght M A, Madden D, Masin Z, Plummer M and Tennyson J 2012 *Euro. J. Phys. D* **66**, 58.

Cernicharo J, Guelin M, Agundez M, McCarthy M C and Thaddeus P 2008 *Astrophys. J.* **688**, L83–L86.

Chakrabati K and Tennyson J 2012 *Eur. Phys. J. D* **66**, 31.

Chang E S and Fano U 1972 *Phys. Rev. A* **6**, 173–185.

Chang E S and Temkin A 1969 *Phys. Rev. Letts.* **23**(8), 399.

Chistophorou L G and Olthoff J K 2004 *Fundamental Electron Interactions with Plasma Processing Gases* Kluwer Academic/Plenum Publishers.

Chu S I and Dalgarno A 1974*a* *Phys. Rev. A* **10**, 788–792.

Chu S I and Dalgarno A 1974*b* *Phys. Rev. A* **10**, 788–92.

Coffin J M, Hamliton T P, Pulay P and Hargittai I 1989 *Inorg. Chem.* **28**, 4092–4094.

Corey G C and McCourt F R 1983 *J. Phys. Chem.* **87**, 2723–2730.

Crawford O H, Allison A C and Dalgarno A 1969 *Astron. Astrophys.* **2**, 451.

Cui Q and Morokuma K 1998 *J. Chem. Phys.* **108**, 626–636.

Curik R, Ziesel J P, Jones N C, Field T and Field D 2006 *Phys. Rev. Lett.* **12**, 123202–123206.

Dobbs K D and Hehre W J 1987 *J. Comp. Chem* **8**, 880–893.

Domcke W 1991 *Phys. Rep.* **208**, 97–188.

Dora A, Bryjko L, van Mourik T and Tennyson J 2012 *J. Chem. Phys.* **136**, 024324.

Dubernet M L, ca C B, Daniel F, Dayou F, Doronin M, Faure A, Feautrier N, Flower D R, Lique F, Grosjean A, Halvick P, Marinakis S, Moreau N, Roueff E, Spielfiedel A, Stoecklin T, Tennyson J, Vasserot A M and Wiesenfeld L n.d. *Astron. Astrophys.* .

Dunning T H 1970 *J. Chem. Phys* **53**, 2823.

Dunning T H 1989 *J. Chem. Phys.* **90**, 1007.

Ershov A and Borysow J 2007 *Plasma Source Sci. Technol.* **16**, 798–802.

Ervin K M and Lineberger W C 1991 *J. Chem. Phys* **95**, 1167.

Fano U 1970 *Phys. Rev. A* **2**, 353–365.

Faure A, Gorfinkiel J D, Morgan L A and Tennyson J 2002*a* *Computer Phys. Communs.* **144**, 224–241.

Faure A, Gorfinkiel J D, Morgan L A and Tennyson J 2002*b* *Computer Phys. Comms.* **144**, 224–241.

Faure A, Gorfinkiel J D and Tennyson J 2004 *J. Phys. B: At. Mol. Opt. Phys.* **37**, 801–807.

Faure A, Kokoouline V, Greene C H and Tennyson J 2006 *J. Phys. B: At. Mol. Opt. Phys.* **39**, 4261–4273.

Faure A and Tennyson J 2001 *Mon. Not. R. astr. Soc.* **325**, 443–448.

Faure A and Tennyson J 2002*a* *J. Phys. B: At. Mol. Opt. Phys.* **35**, 3945–3956.

Faure A and Tennyson J 2002*b* *J. Phys. B: At. Mol. Opt. Phys.* **35**, 1865–1873.

Faure A, Varambhia H N, Stoecklin T and Tennyson J 2007 *Mon. Not. R. astr. Soc.* **382**, 840–848.

Feshbach H 1958 *Ann. Phys.* **5**, 357–390.

Feshbach H 1962 *Ann. Phys.* **19**, 287–313.

Flores J R 1992 *J. Phys. Chem.* **96**, 4414–4420.

Florescu-Mitchell A I and Mitchell J B A 2006 *Phys. Rep.* **430**, 277–374.

Fortenberry R C, King R A, Stanton J F and Crawford T D 2010 *J. Chem. Phys.* **132**.

Fray N, Benilan Y, Cottin H, Gazeau M C and Crovisier J 2005 *Planet. Sp. Sci.* **53**, 1243–1262.

Gerarda J C, Huberta B, Shematovichb V, Bisikalob D and Gladstone G 2008 *Planetary and Space Sci.* **56**, 542–552.

Gershikov A G, Subbotina N Y and Hargittai M 1990 *J. Mol. Spec.* **143**, 293–303.

Giannetti A, Brand J, Massi F, Tieftrunk A and Beltran M T 2012 *Astron. Astrophys.* **538**.

Goicoechea J R, Compigne M and Habart E 2009 *ApJ* **699**, L165.

Gorfinkiel J D and Tennyson J 2005 *J. Phys. B: At. Mol. Opt. Phys.* **38**, 1607–1622.

Gottlieb C A, Brunken S, McCarthy M C and Thaddeus P 2007 *J. Chem. Phys.* **126**, 191101.

Guillon G and Stoecklin T 2007 *Phys. Rev. A* **75**, 052722–052728.

Gupta H, Brunken S, Tamassia F, Gottlieb C A, McCarthy M C and Thaddeus P 2007 *Astrophys. J.* **655**, L58–L60.

Hall D T, Strobel D F, Feldman P D, McGrath M A and Weaver H A 1995 *Nature Let.* **373**, L677–679.

Halmová G, Gorfinkiel J D and Tennyson J 2008 *J. Phys. B: At. Mol. Opt. Phys.* **41**, 155201.

Halpern J B, Huang Y and Titarchuk T 1996 *Astrophysics and Space Science* **236**, 11–17.

Harada N and Herbst E 2008 *Astrophys. J.* **685**, 272–280.

Hargittai I, Schultz G, Tremmel J, Kagramanov N D, Maltsev A K and Nefedov M 1983 *J . Am. Chem. Soc. Lett.* **105**, 2896–2897.

Harrison S and Tennyson J 2011 *J. Phys. B: At. Mol. Opt. Phys.* **44**, 045206.

Harrison S and Tennyson J 2012 *J. Phys. B: At. Mol. Opt. Phys.* **45**, 035204.

Harrison S, Tennyson J and Faure A 2012 *J. Phys. B: At. Mol. Opt. Phys.* **45**, 175202.

Hebert A J, Lovas F J, Melendres C A, Hollowell C D, Jr. T L S and Jr. K S 1968 *J. Chem. Phys.* **48**, 2824–2825.

Hecht J H, Christensen A B, Gutierrez D J, Kayser D, Sharp W E, Sharber J R, Winningham J D, Frahm R A, Strickland D J and McEwen D J 1995 *J. Geo. Res.* **100**, 17285–17298.

Herbst E and Osamura Y 2008 *Astrophys. J.* **679**, 1670–1679.

Herzberg G and Huber K P 1979 *Molecular Spectra and Molecular Structure* Vol. 4 Van Nostrand Reinhold.

Hosseini B H, Sadeghpour H R and Balakrishnan N 2005 *Phys. Rev. A* **71**, 023402–023409.

Huber K P and Herzberg G 1997 *NIST Chemistry WebBook, NIST Standard Reference Database Number 69. Eds. P.J Linstrom and W. G. Mallard. National Institute of Standards and Technology. Gaithersburg M.D. 20899, http://webbook.nist.gov* .

Hudson C E, Ramsbottom C A and Scott M P 2012 *ApJ* **750**, 65.

Ishiguro M, Okabayashi T and Tanimoto M 1995 *J. Mol. Struc.* **352/353**, 317–323.

Itikawa Y and Ichimura A 1990 *J. Phys. Chem. Ref. Data* **19**, 637–651.

Itikawa Y and Mason N 2005 *J. Phys. Chem. Ref. Data* **34**, 1–22.

Janousek B K, Brauman J I and Simons J 1979 *J. Chem. Phys.* **71**, 2057.

Jevons W and Bashford L A 1937 *Proc. Phys. Soc.* **49**, 554–567.

Jimenez-Serra I, Martin-Pintado J, Viti S, Martin S, Rodriguez-Franco A, Faure A and Tennyson J 2006 *Astrophys. J.* **650**, L135–L138.

Joshipura K N and Patel P M 1994 *Z. Phys. D* **29**, 269–273.

Kaiser M E and Wright E L 1990 *ApJ* **356**, L1–L4.

Kalcher J 2002 *Phys. Chem. Chem. Phys.,* **4**, 3311–3317.

Kalugina Y, Lique F and Kos J 2012 *Mon. Not. R. astr. Soc.* **422**, 812–818.

Katsch H M, Tewes A, Quandt E, Goehlich A, Kawetzki T and Dobele H F 2000 *J. Appl. Phys.* **88**, 6232–6238.

Kim W, Qin W, McCoy D and Torop L 2001 *Chem. Phys.* **264**, 401–411.

Kim Y K 2001 *Phys. Rev. A* **64**, 032713–1–032713–10.

Kim Y K 2007 *J. Chem. Phys.* **126**, 064305–1–064305–8.

Kimura M, Itikawa Y and Bederson B 2001 *Adv. At. Mol. Opt. Phys.* **44**, 33–57.

Klein R, McGinnis R P and Leone S R 1983 *Chem. Phys. Letters* **100**, 475–478.

Kolos R, Gronowski M and Botschwina P 2008 *J. Chem. Phys.* **128**, 154305.

Krelowski J, Galazutdinov G and Beletsky Y 2011 *Astron. Astrophys.* **531**, A68.

Lane A M and Robson D 1966 *Phys. Rev.* **151**, 774–787.

Lane N F 1980*a* *Rev. Mod. Phys.* **52**, 29–119.

Lane N F 1980*b* *Rev. Mod. Phys.* **52**, 29–119.

Larsson M and Orel A E 2008 *Dissociative Recombination of Molecular Ions* Cambridge University Press.

Leach S 2012 *Mon Not R astr Soc* **421**, 1325.

Lim A J, Rabadán I and Tennyson J 1999 *Mon. Not. R. astr. Soc.* **306**, 473–478.

Lique F and Klos J 2011 *Mon Not R astr Soc* **413**, L20–L23.

Liu Y, Duan C, Lie H, Guo H, Guo Y, Liu X and Lin J 2001 *Journal of Molecular Spectroscopy* **205**, 16–19.

Lopez-Duran D, Bodo E and Gianturco F 2008 *Comp. Phys. Comm.* **179**, 821–838.

Lovell A J, Kallivayalil N, Schloerb F B, R. C M, C. H K and Gombosi T I 2004 *Astrophys. J.* **613**, 615–621.

Löwdin P O 1955 *Phys. Rev.* **97**, 1474–1489.

Martinez T and Levine R 1996 *J. Chem. Phys.* **105**, 6334–6341.

McCarthy M C, Gottlieb C A, Gupta H and Thaddeus P 2006 *Astrophys. J.* **652**, L141–L144.

McCarthy M C, Gottlieb C A, Thaddeus P, Horn M and Botschwina P 1995 *J. Chem. Phys.* **103**, 7821–7827.

Meier R R 1991 *Space Sci. Reviews* **58**, 1–185.

Midda S and Das A K 2004 *International Journal of Quantum Chemistry* **98**, 447–455.

Millar T J, Walsh C, Cordiner M A, Chumin R N and Herbst E 2007 *Astrophys. J.* **662**, L87–L90.

Morgan L A 1984 *Computer Phys. Communs.* **31**, 419–422.

Morgan L A, Burke P G and Gillan C J 1990 *J. Phys. B: At. Mol. Opt. Phys.* **23**, 99–113.

Morgan L A, Gillan C J, Tennyson J and Chen X 1997 *J. Phys. B: At. Mol. Opt. Phys.* **30**, 4087–4096.

Morgan L A, Tennyson J and Gillan C J 1998*a* *Computer Phys. Communs.* **114**, 120–128.

Morgan L A, Tennyson J and Gillan C J 1998*b* *Computer Phys. Comms.* **114**, 120–128.

Munjal H and Baluja K L 2007 *J. Phys. B: At. Mol. Opt. Phys.* **40**, 1713.

Musial M 2005 *Molecular Physics* **103**, 2055–2060.

Nakagami K, Ohtsuki Y and Fujimura Y 2002 *J. Chem. Phys.* **117**, 6429–6438.

Natterer J and Koch W 1995 *Molecular Physics* **84**, 691–706.

Noble C J and Nesbet R K 1984 *Computer Phys. Communs.* **33**, 399–411.

Norcross D W and Padial N T 1982 *Phys. Rev. A* **25**, 226–238.

Ortiz J V 1998 *Chem. Phys. Letters* **296**, 494–498.

Packirisamy S, Schwam D and Litt M H 1995 *Journal of Materials Science* **30**, 308–320.

Petrie S and Herbst E 1997 *Astrophys. J.* **491**, 210–215.

Pfingst K, Thummel H T and Peyerimhoff S D 1992 *J. Phys. B: At. Mol. Opt. Phys.* **25**, 2107–2119.

Polak R and Fiser J 2002 *Journal of Molecular Structure* **584**, 69–77.

Porfireva G A 1975 *Astronomicheskii Zhurnal* **52**, 593–598.

Rabadán I, Sarpal B K and Tennyson J 1998*a* *Mon. Not. R. astr. Soc.* **299**, 171–175.

Rabadán I, Sarpal B K and Tennyson J 1998*b* *J. Phys. B: At. Mol. Opt. Phys.* **31**, 2077–2090.

Rabadán I and Tennyson J 1996 *J. Phys. B: At. Mol. Opt. Phys.* **29**, 3747–3761.

Rabadán I and Tennyson J 1997 *J. Phys. B: At. Mol. Opt. Phys.* **30**, 1975–1988. erratum 31, 4485-4487 (1998).

Rábadan I and Tennyson J 1998*a* *Computer Phys. Communs.* **114**, 129–141.

Rabadán I and Tennyson J 1998*b* *Computer Phys. Comms.* **114**, 129–141.

Radford H E and Broida H P 1962 *Phys. Rev.* **128**, 231–242.

Rao K B and Haranath P V 1969 *J. Phys. B. At. Mol. Phys.* **2**, 1382–1386.

Riascos H, Zambrano G and Prieto P 2004 *Braz. J. Phys.* **34**, 1583–1586.

Robb W D 1972 *Computer Phys. Communs.* **4**, 16–19.

Roberts J F, Jimenez-Serra I, andS. Viti J M P, Rodriguez-Franco A, Faure A and Tennyson J 2010 *Astron. Astrophys* **513**, A46.

Roothan C C J 1951 *Rev. Mod. Phys.* **23**, 69–89.

Roth K C, Meyer D M and Hawkins I 1993 *ApJ* **413**, L67–L71.

Sadlej J and Roos B O 1991 *Chem. Phys. Let.* **180**, 81–87.

Sakai Y, Miyoshi E and Anno T 1992 *Can. J. Chem.* **70**, 309–313.

Sandrone G and Dixon D 1998 *J. Phys. Chem. A* **102**, 10310–10317.

Sanna N and Gianturco F A 1998 *Computer Phys. Communs.* **114**, 142–167.

Sarpal B K, Branchett S E, Tennyson J and Morgan L A 1991 *J. Phys. B: At. Mol. Opt. Phys.* **24**, 3685–3699.

Schneider B 1975 *Chem. Phys. Lett.* **31**, 237–241.

Schneider B I and Hay P J 1976 *Phys. Rev. A* **13**, 2049–2056.

Scholz T T 1991 *J. Phys. B: At. Mol. Opt. Phys.* **24**, 2127–2146.

Schuchardt K L, Didier B T, Elsethagen T, Sun L, Gurumoorthi V, Chase J, Li J and Windus T L 2007 *J. Chem. Inf. Model.* **47**, 1045–1052.
URL: *https://bse.pnl.gov/bse/portal*

Shafir D, Novotny S, Buhr H, Altevogt S, Faure A, Grieser M, Harvey A G, Heber O, Hoffmann J, Kreckel H, Lammich L, Nevo I, Pedersen H, Rubinstein H, Schneider I F, Schwalm D, Tennyson J, Wolf A and Zajfman D 2009 *Phys. Rev. Lett.* **102**, 223202.

Shi D, Li W, Sun J and Zhu Z 2011 *Journal of Quantitative Spectroscopy & Radiative Transfer* **112**, 2335–2346.

Slater J C 1960 *Quantum Theory of Atomic Structure* McGraw-Hill.

Sordo J A 2001 *J. Chem. Phys.* **114**, 1974–1980.

Stibbe D T and Tennyson J 1999 *Chem. Phys. Letts.* **308**, 532–536.

Szabo A and Ostlund N S 1996 *Modern Quantum Chemistry: Introduction to Advanced Electronic Structure Theory* Dover Publications.

Taylor T R and Xu C S 1998 *J. Chem. Phys.* **108**, 10018–10026.

Tennyson J 1996 *J. Phys. B: At. Mol. Opt. Phys.* **29**, 1817–1828.

Tennyson J 1997 *Computer Phys. Communs.* **100**, 26–30.

Tennyson J 2010 *Phys. Rep.* **491**, 29–76.

Tennyson J, Brown D B, Munro J J, Rozum I, Varambhia H N and Vinci N 2007 *J. Phys. Conf. Series* **86**, 012001.

Tennyson J and Noble C J 1984*a* *Computer Phys. Communs.* **33**, 421–424.

Tennyson J and Noble C J 1984*b* *Computer Phys. Comms.* **33**, 421–424.

Terzieva R and Herbst E 2000 *International Journal of Mass Spectroscopy* **201**, 135–142.

Thaddeus P 1972 *Annu. Rev. Astro. Astrophysics.* **10**, 305–334.

Thaddeus P, Gottlieb C A, Gupta H, Brunken S, McCarthy M C, Agundez M, Guelin M and Cernicharo J 2008 *Astrophys. J.* **677**, 1132–1139.

Thogersen L and Olsen J 2004 *Chem. Phys. Letters* **393**, 36–43.

Thomas M R J, Bell K L and Berrington K A 1997 *J. Phys. B: At. Mol. Opt. Phys.* **30**, 4599–4607.

Thompson R and Dalby F W 1968 *Canadian Journal of Physics* **46**, 2815–2819.

Thummel H T, Nesbet R K and Peyerimhoff S D 1992 *J. Phys. B: At. Mol. Opt. Phys.* **25**, 4553–4579.

Thummel H T, Nesbet R K and Peyerimhoff S D 1993 *J. Phys. B: At. Mol. Opt. Phys.* **25**, 1233–1251.

Varambhia H N, Faure A, Graupner K, Field T A and Tennyson J 2010 *Mon. Not. R. astr. Soc.* **403**, 1409–1412.

Varambhia H N, Gupta M, Faure A, Baluja K L and Tennyson J 2009 *J. Phys. B: At. Mol. Opt. Phys.* **42**, 095204.

Varambhia. H N and Tennyson J 2007 *J. Phys. B: At. Mol. Opt. Phys.* **40**, 1211–1233.

Vuitton V, Lavvas P, Yelle R V, Galand M, Wellbrock A, Lewis G R, Coates A J and Wahlund J E 2009 *Planet. Space Sci.* **57**.

Werner H J, Knowles P J, Lindh R, Manby F R, Schütz M, Celani P, Korona T, Mitrushenkov A, Rauhut G, Adler T B, Amos R D, Bernhardsson A, Berning A, Cooper D L, Deegan M J O, Dobbyn A J, Eckert F, Goll E, Hampel C, Hetzer G, Hrenar T, Knizia G, Köppl C, Liu Y, Lloyd A W, Mata R A, May A J, McNicholas S J, Meyer W, Mura M E, Nicklass A, Palmieri P, Pflüger K, Pitzer R, Reiher M, Schumann U, Stoll H, Stone A J, Tarroni R, Thorsteinsson T, Wang M and Wolf A 2008 'MOLPRO, version 2008.3, a package of ab initio programs'.
URL: *http://www.molpro.net*

Widmark P O, Malmqvist P A and Roos B O 1990 *Theor Chim Acta* **77**, 291–306.

Wigner E 1946 *Phys. Rev.* **70**, 606–618.

Wigner E P and Eisenbud L 1947 *Phys. Rev.* **72**, 29–41.

Woon D E 1995 *Chem. Phys. Let.* **244**, 45 – 52.

Zatsarinny O and Tayal S S 2001 *J. Phys. B: At. Mol. Opt. Phys* **34**, 1299–1319.

Zhan C G and Iwata S 1996 *J. Chem. Phys.* **104**, 9058–9064.

Zhang R, Faure A and Tennyson J 2009 *Physica Scripta* **80**, 015301.

Zhang R, Galiatsatos P G and Tennyson J 2011 *J. Phys. B: At. Mol. Opt. Phys.* **44**, 195203.

Ziegler T and Gutsev G L 1992 *J. Comp. Chem.* **13**, 70–75.

Ziesel J P, Azria R and Teillet-Billy D 2001 *Int. J. Mass Spectrom.* **205**, 137–148.